DEVELOPMENT OF AN ELECTROMAGNETIC SENSING SYSTEM FOR FIELD RECONSTRUCTION AND GEOMETRICAL FEATURE MEASUREMENT

A Dissertation
Presented to
The Academic Faculty

by

Min Li

In Partial Fulfillment
of the Requirements for the Degree
Doctor of Philosophy in the
School of Mechanical Engineering

Georgia Institute of Technology
December 2017

DEVELOPMENT OF AN ELECTROMAGNETIC SENSING SYSTEM FOR FIELD RECONSTRUCTION AND GEOMETRICAL FEATURE MEASUREMENT

Approved by:

Dr. Kok-meng Lee, Advisor
School of Mechanical Engineering
Georgia Institute of Technology

Dr. Yan Wang
School of Mechanical Engineering
Georgia Institute of Technology

Dr. Shreyes N. Melkote
School of Mechanical Engineering
Georgia Institute of Technology

Dr. Yang Wang
School of Civil and Environmental Engineering
Georgia Institute of Technology

Dr. Boris Prilutsky
School of Biological Sciences
Georgia Institute of Technology

Date Approved: November 03, 2017

ACKNOWLEDGEMENTS

I would like to sincerely thank my advisor, Dr. Kok-Meng Lee. His wide knowledge, creative thinking and insightful guidance have provided me the basis and direction for this work. I am always inspired and encouraged by his endless passion and enthusiasm. Without his supervision, this work would not be realized. I would also like to thank my thesis committee members Dr. Shreyes N. Melkote, Dr. Boris Prilutsky, Dr. Yan Wang and Dr. Yang Wang for their time and valuable suggestions on this thesis.

I also want to express my gratitude to the staffs at Electronics Lab in The George W. Woodruff School of Mechanical Engineering especially Anh Nguyen, for their help with electrical circuit design and printed circuit board fabrication. For this research, I have received lots of grateful suggestions and helps from the former and current colleagues in AIMRL group: Dr. Jiajie Guo, Dr. Kun Bai, Dr. Wei Wang, Dr. Xiao Liang, Dr. Yin Chen, Dr. Jingjing Ji, Dr. Donghai Wang, Xiemin Chen, Yang Xie, Chun-Yeon Lin, Yang Huang, Lei Li, Bingjie Hao, Man Yu. Their assistances on this research are greatly appreciated.

I appreciate the summer intern program provided by The State Key Laboratory of Digital Manufacturing Equipment and Technology of Huazhong University of Science and Technology, Wuhan, China. Without this opportunity, my work cannot be extended to manufacturing applications.

The financial support from National Science Foundation (NSF) EFRI-M3C 1137172, NSF grant number CMMI-1662700 and National Basic Research Program of China (973 Program, Grant No. 2013CB035803) is gratefully acknowledged.

This thesis is dedicated to my parents, Guilin Li and Ailan Ding, who provide me with endless love, support, understanding and encouragement throughout my life. I cannot imagine what I have achieved without their supports.

TABLE OF CONTENTS

LIST OF TABLES

LIST OF FIGURES

LIST OF SYMBOLS AND ABBREVIATIONS

Capital Symbols

$\mathbf{A}$	Magnetic vector potential
$\mathbf{A}_S$	External magnetic vector potential
$\mathbf{B}$	Magnetic flux density
$\mathbf{B}_C$	Magnetic flux density generated by electromagnet
$\mathbf{B}_E$	Magnetic flux density generated by eddy current
$\mathbf{B}_G$	Geomagnetic field
$\mathbf{B}_U$	Un-modeled magnetic field
$\mathbf{C}$	Cost matrix of Dynamic time warping method
$\mathbf{D}$	Accumulated matrix of Dynamic time warping method
$\mathbf{G}$	Magnetic tensor
$\mathbf{H}$	Constraint matrix
I_o	Excitation current
$\mathbf{J}_i$	Eddy-current density in the i^{th} element
L_o	System characteristic length
$\mathbf{M}$	Magnetic moment
N	Number of turn
N_c	Element number of conductor
N_m	Measurement number
Q_M	Maximum iteration of element refinement
$\mathbf{R}$	Position vector
$\mathbf{T}$	Total magnetic flux density
$\mathbf{V}$	Vector representing the existence probability of cavities

Lower Case Symbols

a_i	Internal radius of electromagnet
a_o	External radius of electromagnet
e_α	Error of regularization method
$\overline{d}$	Spacing interval of the magnetic sensor
f	Excitation frequency
g	Gradient threshold for refinement
k	Factor of absolute current density for refinement
$\mathbf{n}$	Unit normal vector of position vector
$\mathbf{j}_i$	Current source in the i^{th} element
$\mathbf{m}$	Unit vector of magnetic moment
q	Required resolution of magnetic sensor
$\mathbf{r}$	Unit vector of position vector
$\mathbf{v}$	Eigenvector
w	Sensor space of magnetic tensor sensor
$\mathbf{w}_B$	Weight factor of magnetic field
$\mathbf{w}_G$	Weight factor of magnetic tensor

Greek

μ_0	Free-space permeability
μ	Magnetic permeability

α	Regularization parameter
$[\boldsymbol{\alpha}]$	System matrix of state-space representation
$[\boldsymbol{\beta}]$	Input matrix of state-space representation
$[\boldsymbol{\gamma}]$	Output matrix of state-space representation
v_i	Volume of i^{th} element
$\boldsymbol{\sigma}_i$	Conductivity of i^{th} element
δ	Error level
δ_d	Skin depth of eddy current
$\boldsymbol{\eta}$	Regularization data error
ε	Permittivity
ω	Angular velocity
λ	Eigenvalue

Abbreviations

(1, 2, 3) D	One, two, three Dimension
AD	Analog-to-Digital
DMP	Distributed Multipole
DMC	Distributed Multi-level Current
DTW	Dynamic time warping
ECD	Eddy-current Density
EM	Electromagnet
FEM	Finite Element Method
FM	Frequency Modulation
GMR	Giant Magnetoresistance

GPS	Global Positioning System
HT	Hough-transform
MFD	Magnetic Flux Density
MQS	Magneto Quasi-static
MTS	Magnetic Tensor Sensor
PCB	Printed Circuit Board
PDA	Personal Digital Assistance
PEC	Pulsed Eddy Current
PM	Permanent Magnet
RFID	Radio Frequency Identification
SNR	Signal-to-noise Ratio
SQUID	Superconducting Quantum Interference Device
SVD	Singular Value Decomposition
VIP	Visually Impaired Person
Wi-Fi	Wireless Fidelity

SUMMARY

This dissertation has been motivated by two practical applications: The first responds to a need to develop a geomagnetic field-based sensing system to help visually impaired patients locate objects and guide way-finding. The second is a method for intelligent manufacturing application, where an eddy current is electromagnetically induced in a conductive workpiece for real-time measurements of geometrical features. This thesis addresses a common problem in these applications, which involves reconstruction of a physical field from limited measurements for characterizing geometrical features. Inspired by the simplicity of electromagnetic source-based models, this thesis has formulated the forward and inverse electromagnetic problems and derived computationally efficient closed-form solutions to provide a basis for developing a multi-function electromagnetic sensing system and reconstructing a physical field of interest. The source-based models have been employed in the design, analysis and optimization of the sensing system for the above-mentioned applications, upon which two prototype sensing systems have been developed for reconstruction of far and near physical field. An experimental investigation has been carried out to validate the concept feasibility of field reconstruction, verify the source-based models and evaluate the sensor performance. Apart from the development of a multi-function electromagnetic sensing system for geometrical feature measurements, the findings of this thesis have offered a basis of a general field-reconstruction method that has a spectrum of engineering applications.

CHAPTER 1. INTRODUCTION

1.1 Background and Motivation

This dissertation is motivated by two practical applications: The first responds to a need to develop a sensing system that helps visually impaired persons (VIPs) locate objects for picking them up (arm-reaching) and guide navigation (way-finding). The second is a method that can perform real-time estimation of geometry and material properties of electrically conductive workpieces in manufacturing.

The arm-reaching and way-finding are two easy daily tasks; they are, however, often daunting tasks for VIPs who do not have the optical ability to interpret their surroundings. Traditionally, VIPs without residual vision rely on their hands, through white canes for close-range navigation or guide dogs for exploring the surroundings. White canes are most widely used because they are inexpensive, lightweight and small, and can reliably detect sufficiently large obstacles (such as steps and uneven surface) near ground/floor level, but the users must continuously scan the small area ahead of them. Fully trained guide dogs are effective aids, but very expensive and useful only for five years and must be taken care of by VIPs. As a result, it was estimated [1] that only 1% of the two million VIPs have guide dogs. Recent advances in personal mobile devices capable of computing, communication and control (3C), digital imaging, and global positioning, which are widely available at affordable cost, offer potentials to enhance the global perception of the user's surrounds. These are useful technologies for the VIPs; however, they are ineffective for arm reaching and close-range navigation. For instance, although very high-resolution images are now widely available at low cost, optically obtained images must be processed

digitally and converted into some other forms (such as voice and tactile) before they can be effectively appreciated by the visually impaired. Among the key challenges is a need for physical-based information to exchange the existing vision algorithms (that are often designed for machine applications) to facilitate the VIPs' arm reaching and way finding.

The field of metallic additive manufacturing and thin-walled components machining have attracted more and more attention in airspace industries for the past two decades. For the metallic additive manufacturing, due to its machining principle, most critical problems focus on process reliability of the finished-part geometries and material properties, which require layer-by-layer defect detection as well as post-processing precision machining. For such applications with defect detection between layers, the real-time estimation of geometry and material properties are needed to be performed within large areas or volumes. Obviously, most traditional methods which estimate or detect the target parameters within small areas or volumes limit the scopes of applications and manufacturing efficiency.

Machining thin-walled components (such as compressor disks and casings in aircraft engines) with high quality and superior service capability has been challenging due to workpiece deformation and vibration under uncertain cutting forces and thermal effects. The effectiveness of parameter sensing and process monitoring in real time dictates the success of thin-walled component machining. Thereby, there are huge demands for a new sensing technique for intelligent manufacturing, which has potentials to integrate a number multi-functions in a compact sensor and estimate the defects or desired parameters within a large area or volume using one-time measurement.

Inspired by the ability of some biological organisms to detect geomagnetic (earth-magnetic) fields as an orientation cue during migration or homing and the fact the many man-made objects, electronic devices or even the building structures can distort the relatively constant geomagnetic field, the geomagnetic field (magnetostatic field) effects have the potential to help VIPs overcome some problems encountered in daily arm-reaching and way-finding.

Electromagnetic fields have the tremendous characters (such as great penetration, fast response, well-defined theory and oil or other media insensitivity) that are very suitable for the nondestructive sensing and testing in manufacturing. Thereby, this research explores the use of electromagnetic fields (including the magnetostatic field and quasi-static field) and extends the capability for the two applications.

1.2 Prior and Related Works

The following review of the prior and related work is organized in three parts, ferrous object localization/identification, indoor and outdoor navigation for VIPs, and eddy-current testing.

1.2.1 Ferrous Object Localization/Identification

Localization and identification of ferrous/magnetic targets are practical problems in many applications. A creative and efficient way is to sense magnetostatic field of practical interests including armored vehicles (~10μT), geological ore inclusions and archaeological artifacts (~1nT to 1μT), hidden ordnance (~10 nT to 1μT), submarines (~1 to 10nT) and parts of the human body (≤ 10pT). Magnetic field-sensing satisfies many

harsh requirements (contactless, compactness, insensitive to the environments, passive methods) which cannot easily be fulfilled by other methods [2][3][4] and has been successfully used to detect and locate objects given their magnetic properties[5][6]. Inheriting many advantages of magnetic fields (such as great penetration, fast response, and well defined theory), the magnetic field-sensing continues to play an increasingly important role ranging from engineering applications, such as vehicle/ship/aircraft detection and tracking [7][8] to unexploded ordnance localization [3], to emerging medical treatment technologies, such as wireless capsule endoscopy [2].

Due to the difficulty (if not impossible) to precisely model the magnetic effect of an object with arbitrary shape, particularly when the distance is three or more times larger than the target dimension, an unknown magnetic object can be approximated as a magnetic dipole characterized by a magnetic moment **M** as a signature for identifying the magnetic object [3][9] and its location **R** for locating the target [10][11] or tracking its trajectory [2][12]. The problem is reduced to the formulation of an inverse model for solving the six independent component variables in **R** and **M** [9][12] by one of the two commonly used approaches: The 1st approach formulates new parameters or equations from the dipole model to estimate **R** and **M**; for examples, published literature [10][11][12][13]. The 2nd approach iteratively estimates **R** and **M** from the dipole equation with a set of field measurements (with methods such as Levenberg-Marquardt method [2] or iterative nonlinear least-squares estimation) [5][14][15]. In general, these approaches require multiple measurements of the fields at different locations, which may be taken by means of a fixed-sensor array, a moving sensor system or the target movement [6][12]. In either fixed or moving sensor system, the axes of the individual magnetometers must be

accurately aligned (or pre-calibrated) with specified directions, which make these approaches clumsy and time-consuming to implement in practice. In addition to multiple measurements, the inverse problems are non-linear and their formulations are often ill-posed for solving **R** and **M**; the problems (such as convergence, non-uniqueness and sensitive to initial guess) associated with iterative estimations could make these methods computationally unstable and difficult to implement.

When exploiting magnetostatic fields for locating magnetic objects, the effect of the geomagnetic field must be taken into account, especially when both the fields are in the same order, and accurate **R** and **M** estimates are of prime concern. Although the geomagnetic field can be subtracted from the measurements before applying the methods, the procedure for acquiring its prior knowledge could be complicated, especially when the orientation of the sensing system must change with measurements.

1.2.2 Indoor and Outdoor Navigation for VIPs

Many technologies have been applied to way-finding; for example [16], where auditory feedback was proposed as a navigation aid for the visually impaired. Methods for indoor/outdoor navigation can be broadly divided into three categories based on existing human-made signals, pre-deployed infrastructures and nature-generated physical fields. The first category utilizes signals such as Wireless Fidelity (Wi-Fi), Frequency Modulation (FM) radio, television and phone signals [17][18]. As these signals were originally developed for transferring voice and/or picture information, their accuracy is generally less than desired for positioning. The second category relies on pre-deployed infrastructures that use technologies such as ultra-wideband, radio frequency identification (RFID),

ultrasound and infrared [19][20][21][22] for navigation. The latter two, ultrasound and infrared sensors, provide proximity information but offers no physics-based information about the object, and thus require infrastructures with embedded data for location information. Pre-deployed infrastructures are costly and have limited area coverage. More recently, GPS is widely used for outdoor navigation. However, GPS cannot operate well in areas inaccessible to good-quality satellite signals, and their resolution (typically 10m) are inadequate to avoid dangers in way-finding applications. The third category takes advantages of some nature-generated physical parameters or signals (such as thermal infrared, acceleration and optical field) for positioning [23][24][25]. These natural or passive signal-based technologies offer a low-cost solution.

Methods of obstacle avoidance can be classified into human-generated (active) and nature-generated (passive) signals [26] with advantages and limitations similar to the above mentioned second and third categories for navigation respectively. Active-signal methods, which requires an emitter/receiver pair to generate/detect signals (like ultrasonic and sonar) to determine the existence of the obstacles and their locations [1][27][28], are less sensitive to environmental influences but have limited range of operation. Passive-signal methods (for example, the uses of thermal infrared or optical fields [28][29] naturally emitted/reflected from the obstacles to estimate the obstacle information), in general, have a potential to offer a low-cost solution.

High-resolution vision systems and algorithms are now widely available at relatively low-cost. Video information can be internet-transferred using personal digital assistant (PDA) without relying on pre-deployed or dedicated infrastructures. By transferring information collected by the wearable sensors through the internet, the VIP can require

assistance from host remotely to navigate indoor and outdoor [30][31]. More recently, rapid developing social networks (such as Twitter, Facebook and RSS), which act essentially as a "social sensor", can further enhance the global perception of the surrounding environments [32]. However, these technologies are generally ineffective for close range way-finding by a VIP.

Magnetic sensing technology, inheriting many advantages of magnetic fields (such as great penetration, fast response, and well-defined theory), has been applied to help VIPs, such as reaching ferrous objects [13] and transmitting images via retinal stimulation [33]. The observations of geomagnetic distortion or anomalies in the presence of magnetic objects have led some researchers to develop geomagnetic based methods to help the VIPs navigate; for example, guide walking direction [34][35] with a magnetic compass and localization utilizing the magnetic flux density (MFD) [36].

However, there are two potential barriers to adopting these methods; the accurate magnetic survey of a large area; and effective matching and pattern recognition algorithm. Meanwhile, in practice, the surroundings are unpredictable and uncontrollable which requires the sensing system to provide information in real-time. Moreover, magnetic information of the surrounds and environments may vary with time elapses. Even for the same object, the generated magnetic effects may be different at different moments. Thereby magnetic survey must be constantly updated to keep up with the change in magnetic surrounding conditions, otherwise, the use of obsolete survey data would be inaccurate or even dangerous.

1.2.3 Eddy-current Testing

Eddy-current testing, one important application of electromagnetic technologies, has been in commercial use since the 1950s as one key non-destructive testing. Because of its simple structure and many comparative advantages (such as the long-term reliability, wide measuring range, high sensitivity, high resolution, fast response, better anti-interference property, and oil or other media insensitivity), eddy-current sensors have been widely used in many fields especially in manufacturing [37][38].

Since it is almost impossible to directly measure the eddy current flowing inside the conductors, conventional eddy-current sensors primarily operate on two main methods to indirectly measure the eddy-current effects; namely, the characteristic impedance of the excitation coil [39][40], and the voltage of a secondary or receiver coil [41][42]. These traditional methods operated on the principle of inductive pick-up relying on high-frequency inputs to make a geometrical measurement generally have good linearity but suffer decreasing sensitivity at lower frequencies. More recently, high-precision magnetic sensors with advantages of being small-size, fast response and low power consumption offer the ability to fulfill requirements at both high and low frequencies while ensuring the compact structure integrity of eddy current sensors. Several sensor types, such as the hall-effect sensor, giant magnetoresistance (GMR) sensor and superconducting quantum interference device (SQUID) have been utilized in eddy-current sensor designs [43][44][45][46][47]. Nearly all eddy-current sensors that use magnetic sensors were designed with a single-axis magnetic sensor located at the center of their excitation coil [43][45]. Although lots of information and features of the targets can be estimated with eddy-current (EC) sensors, the single-axis magnetic sensor limits the applications.

Almost all the existing commercial EC sensors provide a single-function measurement; either one of the two geometrical (distance, thickness) parameters or the electrical conductivity. Significant research efforts have recently been directed towards simultaneous measurements by using special excitations instead of the traditional single-frequency sinusoidal signal; for examples, pulsed eddy-current (PEC) [47][48] and multi-frequency [49][50][51][52] eddy-current techniques. The pulsed eddy-current (PEC) techniques have the ability to contain nearly all frequencies but suffer several drawbacks including low signal-to-noise ratio (SNR) and unexpected effects. Although the techniques using multi-frequency excitation signals can significantly improve the SNR by choosing appropriate frequencies, they impose stringent requirements on hardware; for instance, excitation signals of very high frequency are required for distance measurements.

Normally, in the applications of eddy-current testing, to avoid the complicated electromagnetic theories and time-consuming and nonlinear calculation, lots of the researches directly establish the relationship of the measurements and the target parameters using calibration. With those methods, the target parameters of the workpiece at the specific locations can be precisely estimated. However, to obtain the certain parameter across the entire area instead of discrete locations, for instance, defect detection or electrical conductivity estimation, lots of measurements are required to fill the whole area and the area between the measurements can only be estimated using mathematical interpolation which may need precise motion mechanism and make sensing procedures complicated and time-consuming. This problem could be solved if the whole physical field (such as eddy-current field) can be reconstructed.

Because the relationships between the geometrical/material parameters and the indirect measurements of the eddy-current effect are highly coupled and spatially nonlinear, the potentials of EC sensors for manufacturing applications are underexploited.

1.3 Problem Description and Objectives

A common problem in the two above-mentioned applications (visually impaired assistance and geometrical feature detection in manufacturing) involves the reconstruction of an electromagnetic field from finite field measurements. The solutions to this problem can be divided into two parts: The *first* is to develop a real-time sensing system to accurately measure the electromagnetic field at appropriately designed locations. The *second* is to develop a computationally efficient method to reconstruct an electromagnetic field from the finite measurements and derive essential information from it.

Based on electromagnetic field reconstruction from the finite magnetic field measurements, this research aims at developing a novel electromagnetic sensing system which contains the characteristics of intelligence, multifunction and compact structure. Three objectives are needed to be achieved by this research.

- The *first* objective is to formulate the solutions to the forward and inverse electromagnetic models for developing a magnetic multi-sensor array to reconstruct an electromagnetic field from the finite magnetic field measurements.
- The *second* objective is directed towards the design of electromagnetic sensing systems for the two applications mentioned above and numerically analyze and optimize the design using the models developed in the first objective.

– The *final* objective is to experimentally investigate the effectiveness and accuracy of the electromagnetic field reconstruction and evaluate the performance of the sensing system in perspectives of two applications.

1.4 Outline and Organization of Thesis

The remainder of this dissertation is outlined as follows.

Chapter 2 presents a modeling method for electromagnetic field reconstruction which consists of two parts, the forward and inverse problem modeling: The former solves for the electromagnetic fields from the geometry, physical properties or electromagnetic source of a system whereas the latter solves for the geometry, physical properties or electromagnetic source of the system from measured electromagnetic fields. In Chapter 3, an electromagnetic sensing system with compact structure and multiple functions is designed, theoretically analyzed and optimized based on the theories of electromagnetic field reconstruction.

To illustrate the potential capability of being applied in visually impaired assistance and manufacturing for the combination of the electromagnetic field modeling/ reconstruction and the creatively designed sensing system, several simulations and experiments are performed to validate and evaluate the accuracy and efficiency of the sensing system in Chapter 4 and 5.

Finally, Chapter 6 summarizes the contributions of this research as well as the future works that can refine and extend these studies.

CHAPTER 2. ELECTROMAGNETIC FIELD MODELING FOR FIELD RECONSTRUCTION

2.1 Overview

Much like other physical fields, an electromagnetic field, which is three-dimensional (3D), invisible and continuous, can only be measured at finite and discrete locations. It is difficult to derive the continuous information of the whole electromagnetic field, which leads to the motivation of the field reconstruction using finite measurements. Normally, a field model is generally desired to facilitate the field reconstruction. Thereby, the field modeling for reconstruction consists of two parts, the forward and inverse problem modeling: The former solves for the electromagnetic fields from the geometrical, physical properties or electromagnetic source of a system whereas the latter solves for the geometrical, physical properties or electromagnetic source of a system from the measurements of the electromagnetic field.

Inspired by the simplicity of pole-based models such as a distributed multipole (DMP)[53] and a distributed multi-level current source (DMC)[54] models which offer computationally efficient closed-form solutions for characterizing electromagnetic fields, the solutions to the forward and inverse electromagnetic models for an electromagnetic field reconstruction from finite magnetic field measurements are based on the ranges defined in Figure 2.1 where the dipole modelled MFD **B** of a cubic source element (uniformly magnetized in y direction) formulated by (2.1a) is compared against analytic

solutions. As illustrated in Figure 2.1, the operating range can be broadly divided into three regions based on the differences between the dipole model and analytical solutions.

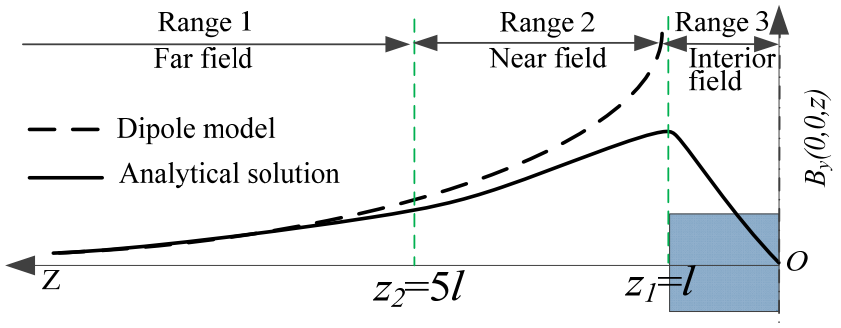

Figure 2.1 Comparison of dipole modeled MFD and analytical solution

$$\mathbf{B} = \frac{PR}{3}\left[-\mathbf{m} + 3(\mathbf{r}^{\mathrm{T}}\mathbf{m})\mathbf{r}\right] \text{ where } P = \frac{3\mu_0 M}{4\pi R^4}; \tag{2.1a, b}$$

where **R** and **M** are a position vector and magnetic moment respectively. μ_0 is the free-space permeability. $\mathbf{m} = \mathbf{M}/M$; $\mathbf{r} = \mathbf{R}/R$; and R and M are the magnitudes of **R** and **M** respectively.

In Range 1 (z>5l where l is the characteristic size of a magnetic object), the MFD can be described by a single dipole model with an error less than 5% of the analytic solution. In Range 2, the errors can be improved by using a DMP or a DCS modeling methods. In Range 3 (z<l or inside the magnetic material), the MFD can be reconstructed numerically using a recursive calculation method. Thereby, the method of electromagnetic field modeling for field reconstruction can be presented in the perspective of the field distance and far and near fields have been treated respectively in this chapter.

2.2 Far Field Magnetostatic Model and Sensing (Illustrated with Magnetostatic Fields)

As illustrated in Figure 2.1, the far MFD field generated by a cubic source element can be approximately modeled using a dipole (with magnetic moment **M)** as viewed by the sensor (at which the coordinate system *xyz* is assigned), which is particularly true when the sensor is far from the element. The MFD of the dipole at a location characterized by a position vector **R** is given by the forward model (dipole model) shown in (2.1a, b). The inverse model is to derive **R** and **M** in terms of dipole generated MFD and its derivations from (2.1a) indicating the presence of a magnetic object and its magnetic centroid and strength.

2.2.1 Magnetic Tensor

The incremental difference of the MFD field can be written in the form of a tensor [**G**] which is asymmetric traceless 3×3 matrix in (2.2a) where $\mathbf{B} = \begin{bmatrix} B_x & B_y & B_z \end{bmatrix}^{\mathrm{T}}$; and ∂_x, ∂_y and ∂_z denote the partial derivatives with respect to $\mathbf{R} = \begin{bmatrix} x & y & z \end{bmatrix}^{\mathrm{T}}$:

$$[\mathbf{G}] = \begin{bmatrix} G_{xx} & G_{yx} & G_{zx} \\ G_{xy} & G_{yy} & G_{zy} \\ G_{xz} & G_{yz} & G_{zz} \end{bmatrix} = \frac{\partial \mathbf{B}}{\partial \mathbf{R}} = \begin{bmatrix} \partial_x B_x & \partial_y B_x & \partial_z B_x \\ \partial_x B_y & \partial_y B_y & \partial_z B_y \\ \partial_x B_z & \partial_y B_z & \partial_z B_z \end{bmatrix} \tag{2.2a}$$

$$[\mathbf{G}]^{\mathrm{T}} = [\mathbf{G}] \text{ and } \partial_x B_x + \partial_y B_y + \partial_z B_z = 0 \tag{2.2b, c}$$

The determinant of [**G**] can be computed from the five independent elements:

$$\left|[\mathbf{G}]\right| = \left(G_{xx}+G_{yy}\right)\left(G_{xy}^2 - G_{xx}G_{yy}\right) - \left(G_{xx}G_{yz}^2 + G_{yy}G_{xz}^2\right) + 2G_{xy}G_{xz}G_{yz} \tag{2.3}$$

Another commonly used scalar parameter derived from the tensor $Q = \mathrm{tr}\left([\mathbf{G}]^{\mathrm{T}}[\mathbf{G}]\right)/2$ can also be similarly represented as below:

$$Q = G_{xy}^2 + G_{xz}^2 + G_{yz}^2 + G_{xx}^2 + G_{yy}^2 + G_{xx}G_{yy} \tag{2.4}$$

Considering the magnetic field generated by a magnetic dipole, the elements of the tensor [**G**] can be derived in (2.5a, b):

$$G_{xi} = \frac{P}{R}\left[xm_i + im_x + \left(\delta_{xi} - 5\frac{xi}{R^2}\right)\left(\sum_{i=x,y,z} im_i\right)\right] \tag{2.5a}$$

$$G_{yj} = \frac{P}{R}\left[ym_j + jm_y + \left(\delta_{yj} - 5\frac{yj}{R^2}\right)\left(\sum_{i=x,y,z} im_i\right)\right] \tag{2.5b}$$

where $\mathbf{m} = \left[m_x, m_y, m_z\right]^{\mathrm{T}}$ and $\delta_{ij} = \begin{cases} 0, & if\ i \neq j \\ 1, & if\ i = j \end{cases}$.

Substituting (2.5a, b) into (2.3) and (2.4) and noting that $\mathbf{m}^{\mathrm{T}}\mathbf{r} = \mathbf{r}^{\mathrm{T}}\mathbf{m} = \cos\theta$ where θ is the angle between **m** and **r**, $\left|[\mathbf{G}]\right|$ and Q for the dipole are

$$\left|[\mathbf{G}]\right| = -P^3\cos\theta(\cos^2\theta + 1) \tag{2.6}$$

$$Q = P^2\left(2\cos^2\theta + 1\right) \tag{2.7}$$

In terms of measured γ in (2.8a), $\cos^2\theta$ can be implicitly solved from the cubic polynomial equation derived by equating $\left|[\mathbf{G}]\right|^2$ in (2.6) to Q^3 in (2.7):

$$\gamma = \frac{\left|[\mathbf{G}]\right|^2}{Q^3} = \frac{C(C+1)^2}{(2C+1)^3} \text{ where } C = \cos^2\theta \tag{2.8a, b}$$

From (2.8a, b), $$aC^3 + 2bC^2 + bC - \gamma = 0 \tag{2.8c}$$

where $a = 1-8\gamma$ and $b = 1-6\gamma$. The solutions to (2.8c) are

$$C_1 = -2a_1 + \left[\left(a_2^3 + a_3^2\right)^{1/2} + a_3\right]^{1/3} - a_2\left[\left(a_2^3 + a_3^2\right)^{1/2} + a_3\right]^{-1/3}$$

$$C_2 = -\frac{C_1}{2} - \frac{b}{a}\left(1 - \sqrt{\frac{2\gamma}{b} - \frac{a}{b}C_1\left(1 + \frac{3a}{4b}C_1\right)}\right)$$

$$C_3 = -\frac{C_1}{2} - \frac{b}{a}\left(1 + \sqrt{\frac{2\gamma}{b} - \frac{a}{b}C_1\left(1 + \frac{3a}{4b}C_1\right)}\right) \tag{2.8d}$$

where $a_1 = \frac{b}{3a}$; $a_2 = \frac{-b}{9a^2}$ and $a_3 = \frac{\gamma}{2a} + 3a_1^2 - 8a_1^3$. Since C is real with a value between 0 and 1, it can be numerically shown using (2.8a, b) that $0 \le \gamma \le (4/27)$, within which only the 3rd solution (2.8d) satisfies $0 \le C_3 \le 1$; thus $\cos^2\theta = C_3$.

The orientation-insensitive P, which indicates the closeness of the object to the sensor, can be experimentally found with (2.9):

$$P = \frac{3\mu_0 M}{4\pi R^4} = \sqrt{\frac{Q}{2\cos^2\theta + 1}} \tag{2.9}$$

2.2.2 Tensor-based Dipole Location/Moment

To express the properties of the dipole (**R, M**) observed from point *O* as a function to the MFD and the tensor **G**, two arbitrary points (*a* and *b*) are introduced (Figure 2.2a). Point *a* is close to the point *O* and the coordinate system XYZ is assigned at the object, $d\mathbf{B} \approx (\mathbf{B}_a - \mathbf{B})$. Point *b* is on $\mathbf{R}_a$ ($\mathbf{r}_a = \mathbf{r}_b$) with equal distance ($R_b = R$) as *O* from the object: $R_a = R + dR$; $d\mathbf{R} = Rd\mathbf{r} + dR\mathbf{r}_b$; $\mathbf{r}_b = \mathbf{r} + d\mathbf{r}$ and $d\mathbf{r} = \mathbf{n}d\vartheta$

As shown in Figure 2.2b, where **n** is a unit vector perpendicular to **r**; and $d\vartheta$ is the angle between **r** and $\mathbf{r}_b$. In the following derivations, we neglect high order terms of *dR* and $d\vartheta$.

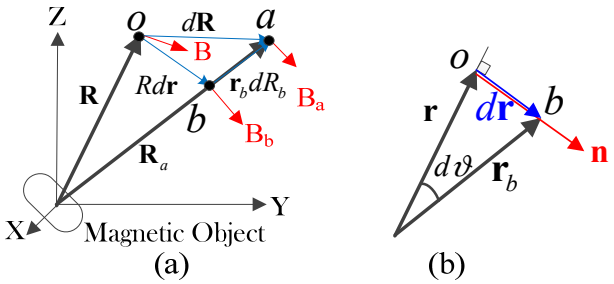

Figure 2.2 Schematics illustrating parameters used in derivation

The difference between the MFDs at points *a* and *b* can be written as

$$\mathbf{B}_a - \mathbf{B}_b = (\mathbf{B}_a - \mathbf{B}) - (\mathbf{B}_b - \mathbf{B}) \tag{2.10}$$

The left term can be derived from (2.1a) where $\mathbf{R}_a$ and $\mathbf{R}_b$ are in the same direction; and the 1st and 2nd terms on the right side are estimated using (2.1a) and (2.2a) respectively. The results are

$$\mathbf{B}_a - \mathbf{B}_b = -3\mathbf{B}_b dR_b / R \tag{2.11a}$$

$$\mathbf{B}_a - \mathbf{B} \approx [\mathbf{G}](R\mathbf{n}d\theta + \mathbf{r}dR) \tag{2.11b}$$

$$\mathbf{B}_b - \mathbf{B} \approx PR\left[(\mathbf{r}^{\mathrm{T}}\mathbf{m})\mathbf{n} + (\mathbf{n}^{\mathrm{T}}\mathbf{m})\mathbf{r}\right]d\theta \tag{2.11c}$$

Substituting the above results into (2.10) followed by equating terms of $d\theta$ and dR on both sides leading to (2.12) from which **R** and **m** can be solved:

$$[\mathbf{G}]\mathbf{n} = P\left[(\mathbf{r}^{\mathrm{T}}\mathbf{m})\mathbf{n} + (\mathbf{n}^{\mathrm{T}}\mathbf{m})\mathbf{r}\right] \tag{2.12a}$$

$$[\mathbf{G}]\mathbf{r} = -P\left[-\mathbf{m} + 3(\mathbf{r}^{\mathrm{T}}\mathbf{m})\mathbf{r}\right] \tag{2.12b}$$

Noting that the right side of (2.12b) can be written as $-3\mathbf{B}/R$ and $\mathbf{r} = \mathbf{R}/R$,

$$\mathbf{R} = -3[\mathbf{G}]^{-1}\mathbf{B} \tag{2.13a}$$

Noting that $P\mathbf{r}^{\mathrm{T}}\mathbf{m} = ([\mathbf{G}]\mathbf{n})^{\mathrm{T}}\mathbf{n}$ which can be derived by dot-multiplying both sides of (2.12a) with **n**, $\mathbf{r}^{\mathrm{T}}\mathbf{n} = 0$ and $\mathbf{n}^{\mathrm{T}}\mathbf{n} = 1$, the dipole moment **M** can be reduced from (2.12b) leading to

$$\mathbf{M} = \frac{4\pi R^3}{3\mu_0}\left([\mathbf{G}]\mathbf{R} + 3\left[([\mathbf{G}]\mathbf{n})^{\mathrm{T}}\mathbf{n}\right]\mathbf{R}\right) \tag{2.13b}$$

2.3 Near Field Magnetic Eddy-current Models (Illustrated with Eddy-current Field)

As illustrated in Figure 2.1, the near MFD field generated by a cubic source element cannot be simply modeled by the dipole model. Using the eddy-current field as an example, the near field has been modeled in this section.

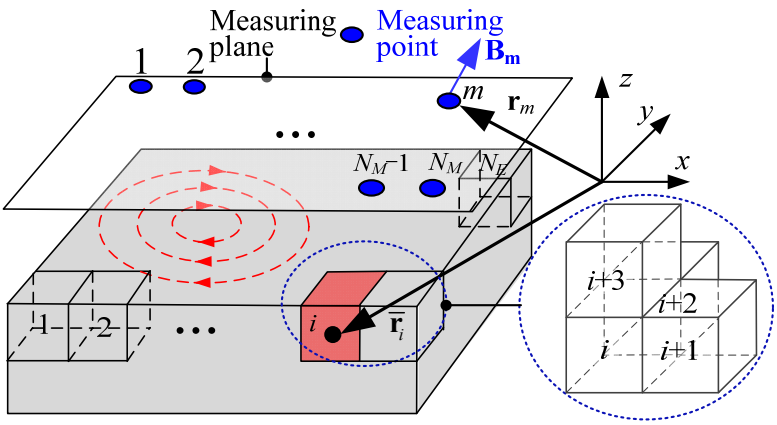

Figure 2.3 Schematics of EM and conductor

Figure 2.3 illustrates the schematics of an eddy-current sensing system, where a conductor made of non-ferrous and anisotropic material is placed in space filled with changing magnetic fields. An eddy current is induced in the conductor consequently, which in terms generates a magnetic field. Given the information of the external changing magnetic field or source, the geometry of the conductor and the relative position between the conductor and measuring points, the ECD field inside the conductor and generated MFD can be estimated (forward model).

2.3.1 State-space Representation of Eddy Current and Magnetic Fields

To establish the forward model, the conductor is evenly discretized into N_E elements with their locations denoted by the displacement vector $\mathbf{r}_i$ where i=1, …, N_E, as shown in Figure 2.3. Referring to Appendix A, the governing equation of an induced ECD $\mathbf{J}_i$ in the i^{th} element with the electrical conductivity $\boldsymbol{\sigma}_i \left(\in \mathbb{R}^{3\times3}\right) = diag\left(\sigma_{ix}, \sigma_{iy}, \sigma_{iz}\right)$, permittivity $\boldsymbol{\varepsilon}_i \left(\in \mathbb{R}^{3\times3}\right) = diag\left(\varepsilon_{ix}, \varepsilon_{iy}, \varepsilon_{iz}\right)$ and volume v_i can be expressed in terms of vector potentials due to an external excitation and its neighboring elements in (2.14) where $\mathbf{A}_{si}$ and $\mathbf{A}_{ki}$ are the magnetic vector potentials generated by the external source and neighboring k^{th} element respective at the i^{th} element[54], i, k = 1, …, N_E.

$$\mathbf{j}_i = -v_i \boldsymbol{\sigma}_i \left[\frac{\partial}{\partial t} \left(\mathbf{A}_{si} + \sum_{k=1}^{N_E} \mathbf{A}_{ki} \right) \right] \tag{2.14}$$

where $\mathbf{j}_i = \mathbf{J}_i v_i$, $\mathbf{A}_{ki} = \boldsymbol{\eta}_{\text{A1}}\left(r_{ik}\right)\mathbf{j}_{Pk} = \boldsymbol{\eta}_{\text{A1}}\left(r_{ik}\right)\mathbf{j}_k + \boldsymbol{\eta}_{\text{A2}}\left(r_{ik}\right)\dot{\mathbf{j}}_k$ referring to (A.7) and (A.8) in Appendix A, $\mathbf{j}_{Pi}\left(= \mathbf{j}_i + \boldsymbol{\varepsilon}_i \boldsymbol{\sigma}_i^{-1} \dot{\mathbf{j}}_i\right)$ is the equivalent current source in the i^{th} element.

$\boldsymbol{\eta}_{\text{A1}}\left(r_{ik}\right)\left(\in \mathbb{R}^{3\times3}\right) = \dfrac{1}{4\pi r_{ik}} diag\left(\mu_{ix}, \mu_{iy}, \mu_{iz}\right)$,

$\boldsymbol{\eta}_{\text{A2}}\left(r_{ik}\right)\left(\in \mathbb{R}^{3\times3}\right) = \dfrac{1}{4\pi r_{ik}} diag\left(\mu_{ix}\varepsilon_{ix}/\sigma_{ix}, \mu_{iy}\varepsilon_{iy}/\sigma_{iy}, \mu_{iz}\varepsilon_{iz}/\sigma_{iz}\right)$, $\boldsymbol{\eta}_{\text{A1}}$ and $\boldsymbol{\eta}_{\text{A2}}$ are the kernel functions of the vector potential, r_{ik} is the distance between the i^{th} and the k^{th} element.

Simplify (2.14) by representing $\mathbf{A}_{ki}$ using $\mathbf{j}_k$, $\boldsymbol{\eta}_{\text{A1}}$ and $\boldsymbol{\eta}_{\text{A2}}$,

$$\mathbf{j}_i = -\upsilon_i \boldsymbol{\sigma}_i \left[\dot{\mathbf{A}}_{si} + \sum_{k=1}^{N_E} \left(\boldsymbol{\eta}_{\mathrm{A}1}(r_{ik}) \dot{\mathbf{j}}_k + \dot{\boldsymbol{\eta}}_{\mathrm{A}1}(r_{ik}) \mathbf{j}_k + \boldsymbol{\eta}_{\mathrm{A}2}(r_{ik}) \ddot{\mathbf{j}}_k + \dot{\boldsymbol{\eta}}_{\mathrm{A}2}(r_{ik}) \dot{\mathbf{j}}_k \right) \right] \tag{2.15}$$

Assemble all N_E elements,

$$-[\mathbf{P}]\mathbf{J} = \dot{\mathbf{A}}_s + [\boldsymbol{\eta}_{A2}]\ddot{\mathbf{J}} + \left([\boldsymbol{\eta}_{A1}] + [\dot{\boldsymbol{\eta}}_{A2}]\right)\dot{\mathbf{J}} + [\dot{\boldsymbol{\eta}}_{A1}]\mathbf{J} \tag{2.16}$$

where $\mathbf{J}\left(\in \mathbb{R}^{3N_E \times 1}\right) = \left[\mathbf{j}_1 \cdots \quad \mathbf{j}_i \quad \cdots \mathbf{j}_{N_E}\right]^{\mathrm{T}}$,

$$\mathbf{A}_s\left(\in \mathbb{R}^{3N_E \times 1}\right) = \left[\mathbf{A}_s(\mathbf{r}_1) \quad \mathbf{A}_s(\mathbf{r}_2) \quad \cdots \quad \mathbf{A}_s(\mathbf{r}_{N_E})\right]^{\mathrm{T}}$$

$$[\mathbf{P}]\left(\in \mathbb{R}^{3N_E \times 3N_E}\right) = diag\left(\mathbf{P}_1, \ \cdots, \ \mathbf{P}_i, \cdots, \ \mathbf{P}_{N_E}\right); \mathbf{P}_i\left(\in \mathbb{R}^{3\times 3}\right) = diag\left(1/\sigma_{ix}\upsilon_i, \ 1/\sigma_{iy}\upsilon_i, 1/\sigma_{iz}\upsilon_i\right);$$

$$[\boldsymbol{\eta}_{\mathrm{A}\ell}]\left(\in \mathbb{R}^{3N_E \times 3N_E}\right) = \begin{bmatrix} \boldsymbol{\eta}_{A\ell}(r_{11}) & \boldsymbol{\eta}_{A\ell}(r_{1i}) & \cdots & \boldsymbol{\eta}_{A\ell}(r_{1N_E}) \\ \boldsymbol{\eta}_{A\ell}(r_{21}) & \boldsymbol{\eta}_{A\ell}(r_{2i}) & \cdots & \boldsymbol{\eta}_{A\ell}(r_{2N_E}) \\ \vdots & \vdots & \boldsymbol{\eta}_{A\ell}(r_{ii}) & \vdots \\ \boldsymbol{\eta}_{A\ell}(r_{N_E 1}) & \boldsymbol{\eta}_{A\ell}(r_{N_E 2}) & \cdots & \boldsymbol{\eta}_{A\ell}(r_{N_E N_E}) \end{bmatrix}, \quad \ell = 1, 2;$$

$\dot{\mathbf{A}}_s$ accounts for the external excitation that may be a time-varying MFD field or relative motion between the conductor and the field; $[\dot{\boldsymbol{\eta}}_{\mathrm{A}\ell}]$ characterizes the corresponding motion that may be due to the deflection of the conductor element and [**P**] accounts the non-uniform distribution of the electrical conductivity and element volume.

Assume there are N_M measuring points in nearby space as illustrated in Figure 2.3. At the m^{th} measuring point (m=1, …, N_M), the MFD $\mathbf{B}_{mi}$ generated by the eddy current

source $\mathbf{j}_i$ in the i^{th} element can be approximately estimated as (2.17) with the assumption that the characteristic dimension of the division being considered is much smaller than the distance between the measuring point and corresponding element[54].

$$\mathbf{B}_{mi} \approx \left[\boldsymbol{\eta}_{B1}(R_{mi})\mathbf{j}_i + \boldsymbol{\eta}_{B2}(R_{mi})\dot{\mathbf{j}}_i \right] \times \mathbf{e}_{mi} \tag{2.17}$$

where $\boldsymbol{\eta}_{B1}(R_{mi})\left(\in \mathbb{R}^{3\times 3}\right) = \frac{1}{4\pi R_{mi}^{\ 2}} diag\left(\mu_{ix}, \mu_{iy}, \mu_{iz}\right), R_{mi} = \left|\mathbf{r}_m - \overline{\mathbf{r}}_i\right|, \mathbf{e}_{mi} = \frac{1}{R_{mi}}\left(\mathbf{r}_m - \overline{\mathbf{r}}_i\right)$,

$\boldsymbol{\eta}_{B2}(R_{mi})\left(\in \mathbb{R}^{3\times 3}\right) = \frac{1}{4\pi R_{mi}^{\ 2}} diag\left(\mu_{ix}\varepsilon_{ix}/\sigma_{ix}, \mu_{iy}\varepsilon_{iy}/\sigma_{iy}, \mu_{iz}\varepsilon_{iz}/\sigma_{iz}\right)$. $\boldsymbol{\eta}_{B1}$ and $\boldsymbol{\eta}_{B2}$ are the kernel functions of the MFD for a point source. $\mathbf{r}_m$ and $\overline{\mathbf{r}}_i$ represent the location of the m^{th} measuring point and the center of the i^{th} conductor element respectively.

Contributed by all N_E elements, the measured $\mathbf{B}_m$ at the m^{th} observed point is given by (2.18). *skew* (**e**) is the skew matrix of the unit vector **e**:

$$\mathbf{B}_m = -\sum_{i=1}^{N_E}\left[\boldsymbol{\eta}_{B1}(R_{mi})skew\left(\mathbf{e}_{mi}\right)\mathbf{j}_i + \boldsymbol{\eta}_{B2}(R_{mi})skew\left(\mathbf{e}_{mi}\right)\dot{\mathbf{j}}_i \right] \tag{2.18}$$

For N_M observed points, the measurement equation in matrix form is given by

$$\mathbf{B}_E\left(\in \mathbb{R}^{3N_M\times 1}\right) = \left[\mathbf{U}_1\right]\mathbf{J} + \left[\mathbf{U}_2\right]\dot{\mathbf{J}} \tag{2.19}$$

where $\mathbf{B}_E(\in \mathbb{R}^{3N_M\times 1}) = \left[\mathbf{B}_{1E} \cdots \quad \mathbf{B}_{mE} \quad \cdots \mathbf{B}_{N_M E} \right]^{\mathrm{T}}$;

$$[\mathbf{U}_\ell]\left(\in \mathbb{R}^{3N_M \times 3N_E}\right) = -\begin{bmatrix} \mathbf{U}_{\ell 11} & \mathbf{U}_{\ell 1i} & \cdots & \mathbf{U}_{\ell 1 N_E} \\ \mathbf{U}_{\ell 21} & \mathbf{U}_{\ell 2i} & \cdots & \mathbf{U}_{\ell 2 N_E} \\ \vdots & \vdots & \mathbf{U}_{\ell mi} & \vdots \\ \mathbf{U}_{\ell N_M 1} & \mathbf{U}_{\ell N_M 2} & \cdots & \mathbf{U}_{\ell N_M N_E} \end{bmatrix}, \ell = 1, 2; .$$

In (2.19), [$\mathbf{U}_\ell$] contains the geometric information relating the N_M measuring locations to the N_E elements of the conductor and $\mathbf{U}_{\ell mi}\left(\in \mathbb{R}^{3\times 3}\right) = \boldsymbol{\eta}_{B\ell}\left(R_{mi}\right) skew\left(\mathbf{e}_{mi}\right)$.

By combining (2.16) and (2.19), the ECD field and generated MFD can be estimated using state-space representation (2.20a, b).

$$\begin{aligned} \dot{\hat{\mathbf{J}}} &= [\boldsymbol{\alpha}]\hat{\mathbf{J}} + [\boldsymbol{\beta}]\boldsymbol{\phi} \\ \mathbf{B}_E &= [\boldsymbol{\gamma}]\hat{\mathbf{J}} \end{aligned} \qquad \text{(2.20a, b)}$$

where $\hat{\mathbf{J}} = \begin{bmatrix} \mathbf{J} & \dot{\mathbf{J}} \end{bmatrix}^{\mathrm{T}}$, $[\boldsymbol{\alpha}] = \begin{bmatrix} \mathbf{0} & \mathbf{I} \\ -[\boldsymbol{\eta}_{A2}]^{-1}\left([\mathbf{P}] + [\dot{\boldsymbol{\eta}}_{A1}]\right) & -[\boldsymbol{\eta}_{A2}]^{-1}\left([\boldsymbol{\eta}_{A1}] + [\dot{\boldsymbol{\eta}}_{A2}]\right) \end{bmatrix}$,

$[\boldsymbol{\beta}] = -[\boldsymbol{\eta}_{A2}]^{-1}$, $[\boldsymbol{\gamma}] = [\mathbf{U}_1 \quad \mathbf{U}_2]$, $\boldsymbol{\phi} = \dot{\mathbf{A}}_s$.

2.3.2 Physical Constraints for Eddy Current

The eddy current induced in the conductor must satisfy two physical constraints:

1) The eddy current cannot pass through the boundary to non-electric elements. When the i^{th} element is a boundary, its current must satisfy the *boundary constraint* ($\mathbf{j}_i \bullet \mathbf{n} s_n = 0$) where **n** is the unit normal to the boundary surface area s_ℓ where $\ell = x, y, z$. In matrix form,

$$\left[\mathbf{0}(\in \mathbb{R}^{1\times 3(i-1)}) \quad s_\ell \mathbf{n}^{\mathrm{T}} \quad \mathbf{0}(\in \mathbb{R}^{1\times 3(N_E-i)})\right]\mathbf{J} = 0 \tag{2.21}$$

2) The *principle of charge conservation* implies that $\nabla\bullet\mathbf{j}_i = 0$. For a hexahedron element (surface areas s_ℓ and unit normal $\mathbf{e}_\ell$), the i^{th} element must satisfy the continuity equation:

$$(\mathbf{j}_{i+1} - \mathbf{j}_i)\bullet\mathbf{e}_x s_x + (\mathbf{j}_{i+2} - \mathbf{j}_i)\bullet\mathbf{e}_y s_y + (\mathbf{j}_{i+3} - \mathbf{j}_i)\bullet\mathbf{e}_z s_z = 0$$

In matrix form,

$$\left[\mathbf{0}(\in \mathbb{R}^{1\times 3(i-1)}) \quad -\mathbf{s}^{\mathrm{T}} \quad \mathbf{s}_x^{\mathbf{T}} \quad \mathbf{s}_y^{\mathbf{T}} \quad \mathbf{s}_z^{\mathbf{T}} \quad \mathbf{0}(\in \mathbb{R}^{1\times 3(N_E-i-3)})\right]\mathbf{J} = 0 \tag{2.22}$$

where $\mathbf{s}^{\mathrm{T}} = \begin{bmatrix} s_x & s_y & s_z \end{bmatrix}$ and $\mathbf{s}_\ell^{\mathrm{T}} = \mathbf{s}^{\mathrm{T}}$ (with $s_{\neq\ell} = 0$).

Assemble (2.21) and (2.22) for all the N_B boundary and N_C continuity constraints and represent in matrix form as (2.23a, b).

$$[\mathbf{H}_B]\left(\in \mathbb{R}^{N_B\times 3N_E}\right)\mathbf{J} = 0, \quad [\mathbf{H}_C]\left(\in \mathbb{R}^{N_C\times 3N_E}\right)\mathbf{J} = 0 \tag{2.23a, b}$$

For the forward model, mathematically, (2.23a, b) are utilized as the constraints when estimating the ECD field and generated MFD by solving the linear equations (2.20a, b).

2.4 Eddy-current Field Reconstruction

The reconstruction of the ECD field in the conductor from the measurement of the MFD involves two steps: 1) Establish a measurement model that represents the measurements of the eddy-current generated MFD with the information of the ECD field

mathematically and analytically; 2) With the derived model, estimate the ECD field distribution using finite MFD measurement which is generalized to be a mathematical linear inverse problem.

The measurement model is expressed in (2.24) where $\boldsymbol{\eta}_1$ is the measurement noise by integrating the constraints (2.23a, b) into the output matrix [$\boldsymbol{\gamma}$] in (2.20b),

$$\mathbf{Y}=[\boldsymbol{\varsigma}]\hat{\mathbf{J}}+\boldsymbol{\eta}_1 \tag{2.24}$$

where $\mathbf{Y}=\begin{bmatrix}\mathbf{B}_E & \mathbf{0}\left(\in \mathbb{R}^{(N_B+N_C)\times 1}\right)\end{bmatrix}^{\mathrm{T}}$, $[\boldsymbol{\varsigma}]\left(\in \mathbb{R}^{(3N_M+N_B+N_C)\times 3N_E}\right)=\begin{bmatrix}[\mathbf{U}]_2 & \mathbf{0} & \mathbf{0}\\ [\mathbf{U}]_1 & [\mathbf{H_B}] & [\mathbf{H_C}]\end{bmatrix}^{\mathrm{T}}$.

2.4.1 Solution to Inverse Problem

Unlike the forward model where the closed-form solutions of MFD measurements $\mathbf{B}_E$ can be solved in terms of known [$\boldsymbol{\alpha}$], [$\boldsymbol{\beta}$], [$\boldsymbol{\gamma}$] and $\boldsymbol{\phi}$ using the system model (2.20a, b) subject to the constraints (2.23a, b), the ECD field reconstruction from limited discrete measurements utilizing eddy-current effects is essentially an inverse problem that solves the induced ECD field $\hat{\mathbf{J}}$ using measurement model (2.24).

For noise-free system with nonsingular $[\boldsymbol{\varsigma}]$ and $(3N_M+N_B+N_C)>3N_E$, (2.24) can be solved using pseudoinverse (2.25):

$$\hat{\mathbf{J}} \approx \left([\varsigma]^{\mathrm{T}} [\varsigma] \right)^{-1} [\varsigma]^{\mathrm{T}} \mathbf{Y} \tag{2.25}$$

However, $(3N_M + N_B + N_C) < 3N_E$ in practice when reconstructing a physical field from limited measurement data. As a result, $[\varsigma]$ becomes increasingly ill-conditioned as measurement cost increases. The pseudo-inverse solutions (2.25) fail as the noise $\boldsymbol{\eta}_I$ in $\mathbf{Y}$ may be greatly amplified.

To address these problems in practice, Tikhonov regularization [55] commonly used in machine learning is employed to solve the ill-posed problem:

$$\hat{\mathbf{J}}_\alpha = [\mathbf{R}_\alpha]\mathbf{Y} \quad \text{where} [\mathbf{R}_\alpha] = \left([\varsigma]^{\mathrm{T}} [\varsigma] + \alpha [\mathbf{I}] \right)^{-1} [\varsigma]^{\mathrm{T}} \tag{2.26a, b}$$

In (2.26b), α (with range [0, 1]) is the regularization parameter to control noise effects and prevent overfitting. Very small α will result in the inadequate filtering of the noise and highly oscillatory solution. On the other hand, most components of the solution are also filtered out with overly smooth solutions. In this work, α is determined using the L-Curve graphical method [56][57] to trade off between noise filtering and solution smoothness which requires no prior information about sensor noise.

2.4.2 Adaptive Element Refinement

One important factor that dramatically affects the accuracy and efficiency of ECD field estimation for forward and inverse problems is how the conductor is discretized. The results of the forward and inverse models using coarse elements cannot represent the details

of the eddy current distribution. However, it is time-consuming to increase accuracy by keeping refining the elements. Meanwhile, for the inverse problem, the reconstruction resolution cannot be improved by refining the elements unlimitedly with the same measurements. Thereby, it is critical to analyze restriction of the element size before refining the elements.

A. Restriction of Element Refinement for Reconstruction

From (2.24), the error of the regularization method $\mathbf{e}_\alpha (= \hat{\mathbf{J}}_\alpha - \hat{\mathbf{J}})$ consists of two parts, regularization truncation $\hat{\mathbf{e}}_\alpha$ and noise amplification error $\tilde{\mathbf{e}}_\alpha$, which can be defined as

$$\hat{\mathbf{e}}_\alpha = \left([\mathbf{R}_\alpha][\varsigma] - [\mathbf{I}]\right)\hat{\mathbf{J}} \text{ and } \tilde{\mathbf{e}}_\alpha = [\mathbf{R}_\alpha]\boldsymbol{\eta}_1 \qquad (2.27a, b)$$

The element refinement for reconstruction is affected by the regularization method for inverse problems, which should satisfy the requirement that noise amplification error $\tilde{\mathbf{e}}_\alpha$ disappears when the data error $\boldsymbol{\eta}_1$ approaches to 0 ($\tilde{\mathbf{e}}_\alpha \to 0$ as $\boldsymbol{\eta}_1 \to 0$).

As outlined in Appendix B for the system with $[\varsigma]$, with α chosen to have the form (2.28a, b, c), $\tilde{\mathbf{e}}_\alpha \to 0$ as $\|\boldsymbol{\eta}_1\| \to 0$ (where $\|\bullet\|$ denotes the standard Euclidean norm) can be guaranteed:

$$\alpha = \delta^p \text{ where } \delta = \|\boldsymbol{\eta}_1\| > 0 \text{ and } 0 < p < 2 \qquad (2.28a, b, c)$$

Too much regularization (large α) leads to too smooth results whereas too little regularization (small α) leads to highly oscillatory artifacts. With the same circumstance, the element refinement will result in the tremendous decrease of the regularization parameter. In practice, the element refinement is limited by the range of p since δ will keep relatively constant for the same sensing systems.

B. Forward Model Modification for Element Refinement

In the forward model, the scalar kernel function of vector potential $\boldsymbol{\eta}_{A\ell}$ (ℓ=1,2) is based on the assumption that the distance between two sources is relatively larger than their characteristic dimension or both sources are point sources. Thereby, the original scalar kernel is only valid for cube elements and this assumption would increase the number of elements which results in long calculation time. To decrease the calculation, the original kernel function is modified to overcome the requirement of the cube elements and extend to the cases with the rectangular elements.

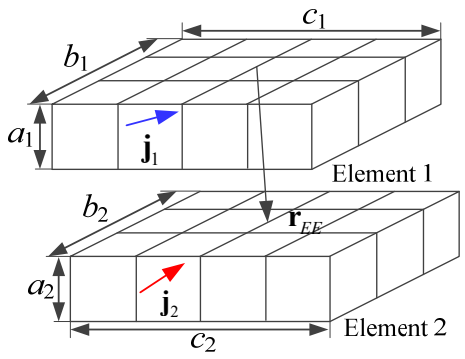

Figure 2.4 Schematics illustrating kernel function modification

To illustrate the modification, two nearby rectangular elements with relative position $\mathbf{r}_{EE}$ (center to center) are utilized as illustrated in Figure 2.4. Assume the size of

two elements are $a_1 \times b_1 \times c_1$ and $a_2 \times b_2 \times c_2$ respectively with the conditions $a_1 < b_1 < c_1$ and $a_2 < b_2 < c_2$. Two rectangular elements are divided into K_1 and K_2 approximative cubes with edge a_1 and a_2 respectively. The new-generated cubes in each element have the same current source $\mathbf{j}_1$ and $\mathbf{j}_2$. The vector potential $\mathbf{A}_{2i}$ generated by Element 2 at the i^{th} cube of Element 1 can be calculated by averaging the vector potential generated by all the K_2 cubes in Element 2 with the scalar kernel function of the vector potential for the cube element.

$$\mathbf{A}_{2i} = \sum_{j=1}^{K_2} \left[\boldsymbol{\eta}_{A1}\left(r_{ij}\right) \mathbf{j}_2 + \boldsymbol{\eta}_{A2}\left(r_{ij}\right) \dot{\mathbf{j}}_2 \right] \tag{2.29}$$

where $\boldsymbol{\eta}_{A\ell}\left(r_{ij}\right)$ is the scalar kernel function between the i^{th} cube in Element 1 and the j^{th} cube in Element 2.

The vector potential $\mathbf{A}_E$ between these two elements approximately equals to the average of the vector potential of Element 2 at each cube in Element 1.

$$\mathbf{A}_E = \frac{1}{K_1} \sum_{i=1}^{K_1} \sum_{j=1}^{K_2} \left[\boldsymbol{\eta}_{A1}\left(r_{ij}\right) \mathbf{j}_2 + \boldsymbol{\eta}_{A2}\left(r_{ij}\right) \dot{\mathbf{j}}_2 \right] \tag{2.30}$$

With the current source in Element 2 $K_2 \mathbf{j}_{E2}$, the kernel function $\boldsymbol{\eta}_{A\ell}$ between two rectangular elements can be approximately derived with (2.30).

$$\boldsymbol{\eta}_{EA\ell} = \frac{1}{K_1 K_2} \sum_{i=1}^{K_1} \sum_{j=1}^{K_2} \boldsymbol{\eta}_{A\ell}\left(r_{ij}\right), \quad \text{where } \ell = 1, 2 \tag{2.31a, b}$$

Since two rectangular elements can be assumed to be cube when the distance between them $\left|\mathbf{r}_{EE}\right|$ is relatively large comparing the characteristic dimension ($\left|\mathbf{r}_{EE}\right| > c_1, c_2$),

the kernel function of the rectangular elements can be calculated using original kernel function for cube elements which will reduce the computation.

Each element is also affected by the eddy current inside itself. Thereby, the kernel function describing this effect is expressed in (2.32a, b) using Element 2 as an example.

$$\boldsymbol{\eta}_{EA\ell} = \frac{1}{K_2^2}\sum_{i=1}^{K_2}\sum_{j=1}^{K_2}\boldsymbol{\eta}_{A\ell}\left(r_{ij}\right), \quad \text{where } \ell=1,2 \tag{2.32a, b}$$

The kernel function is determined only by how the elements are divided, which makes it possible to be calculated previously. This modification will make it possible to refine the elements in a certain direction (if needed) instead of all three directions to keep the shape of a cube, which will tremendously decrease the number of elements and consequently decrease calculation time.

C. Procedure of Element Refinement

To increase the efficiency and accuracy of ECD field estimation, the elements are refined based on the gradient of the estimated ECD field. There are three criterions for element refinement.

- Absolute current density

  Only the dominant parts of the conductor that contain relative large ECD are considered for refinement, which is expressed mathematically as $\|\mathbf{j}_i\| \geq k\|\mathbf{j}_{\max}\|$. $\mathbf{j}_{\max}$ is the maximum ECD pre-calculated in the conductor, k is a factor with the range of $0<k<1$.

- Gradient of the estimated ECD

The elements with a relative large gradient of the ECD are considered as candidates for refinement. Three parameters for the i^{th} element with the characteristic length l_i are introduced to describe the changes of ECD in the nearby elements.

$$f_\ell = \frac{l_i}{\|\mathbf{j}_i\|}\left\|\frac{\partial \mathbf{j}_\ell}{\partial \ell}\right\| \times 100\% \tag{2.33}$$

If $f_\ell > g$, where $\ell = x, y, z$, g is a constant decided by users, Element i should be divided into two even elements in ℓ direction. Element i will be divided into four/eight even elements in corresponding directions if two/three f_ℓ are greater than the given g as illustrated in Figure 2.5.

- Element refinement restriction

  As represented in the last subsection, with the same measurements, over element refinement leads to the increase of reconstruction error. The elements can be refined when satisfying $0<p<2$.

The first two criterions are used for the forward model whereas all three criterions are used for the inverse model. Figure 2.6 graphically illustrates the procedure used in refining the elements, which consists of the following step: Given the MFD data and conductor shape, Step 1 begins with evenly spaced elements. Next, the elemental variables of the field to be reconstructed are estimated using (2.26a) integrated with proper constraints in the 2nd step. In the 3rd step, given k, g and Q_M which is the maximum iteration, the refinement criteria are examined to determine whether the elements should be further sub-divided. The 2nd and 3rd steps are repeated until the criteria are met or the algorithm

exceeds the maximum iteration Q_M. To decrease the calculation, only the eddy current in the refined elements need to be recalculated.

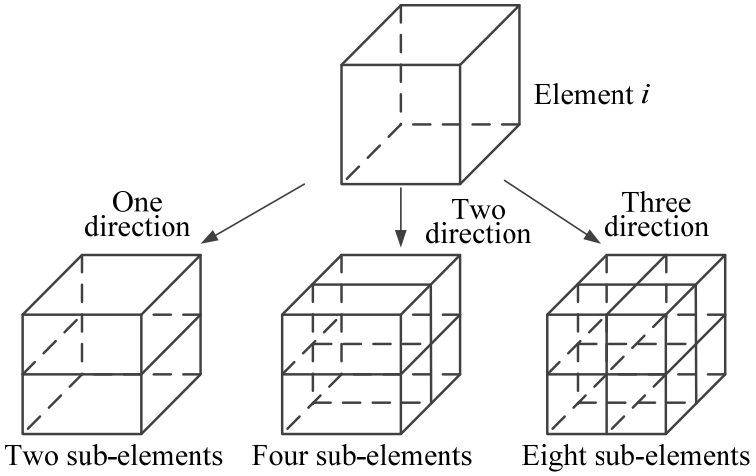

Figure 2.5 Element division using gradient criterion

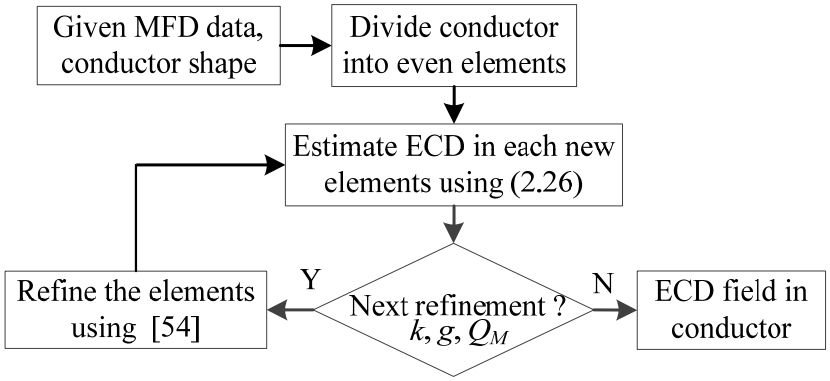

Figure 2.6 Flowchart for element refinement

2.5 Summary

An analytical model of electromagnetic field reconstruction using the finite measurements of the magnetic field has been presented inspired by the simplicity of pole-based models. Illustrated with the magnetostatic fields, the far field generated by a magnetic source element can be approximately modeled as a dipole which simplifies the

field reconstruction to the problem of deriving location **R** and moment **M** using finite field measurements. A gradient-based method for **R** and **M** estimation has been provided.

For the near field (illustrated with Eddy-current field), an analytical model of eddy-current field reconstruction (including the forward and inverse models) using the finite measurements of the MFD field generated by the ECD field has been presented. By discretizing the target/conductor, the forward model is linearly expressed using state-space representation (matrix form). The mathematical method of Tikhonov regularization is utilized to estimate the ECD field with the derived matrix expression.

Some improvements have been provided for the reconstruction model. The physical constraints are developed and integrated into the reconstruction model and the resolution of the reconstruction model is analyzed, which provides the requirements for the measurements (number and location) and the criterions for the refinement method. An automatic refinement method based on the gradient of pre-calculated ECD field is also provided to improve the accuracy of the field reconstruction and reduce calculation

CHAPTER 3. ELECTROMAGNETIC SENSING SYSTEM DESIGN AND ANALYSIS

3.1 Overview

Based on the model of the electromagnetic field reconstruction expressed in the last chapter, an electromagnetic sensing system with compact structure and multiple functions has been creatively designed, theoretically analyzed and optimized.

3.2 Sensing System Design

The objective of the electromagnetic sensing system is to provide finite and discrete electromagnetic information to reconstruct the invisible and unmeasurable electromagnetic fields using the model of electromagnetic field reconstruction presented in Chapter 2.

More specifically, the far electromagnetic field can be modeled by the dipole model. The magnetic tensor and MFD generated by the dipole are required for the dipole location/moment identification. Near electromagnetic field modeling becomes complicated and multiple measurements of the MFD are desired to reconstruct the ECD field inside the conductor. Thereby, the sensing system should be able to measure the magnetic fields at multiple desired locations and derive magnetic tensor from the measurements.

3.2.1 Structure of Sensing System

Not only the MFD **B**, but also its derivation magnetic tensor [**G**] are involved. Because of the properties of magnetic tensor [**G**] shown in (2.2b, c), only five elements of [**G**] require calculation. A small sensing unit of a magnetic sensor array that is capable of

measuring [**G**] consists of two orthogonal pairs of 3-axis magnetic sensors mounted on $\pm w/2$ of the x and y axes of its local coordinate system as shown in Figure 3.1(a); the five elements of [**G**] are defined in (3.1a, b) where $i = x, y, z$ and $j = y, z$ define the i^{th} and j^{th} MFD components respectively:

$$G_{xi} = \partial_x B_i = \frac{B_{i,x+} - B_{i,x-}}{w};\ G_{yj} = \partial_y B_j = \frac{B_{j,y+} - B_{j,y-}}{w} \qquad (3.1a, b)$$

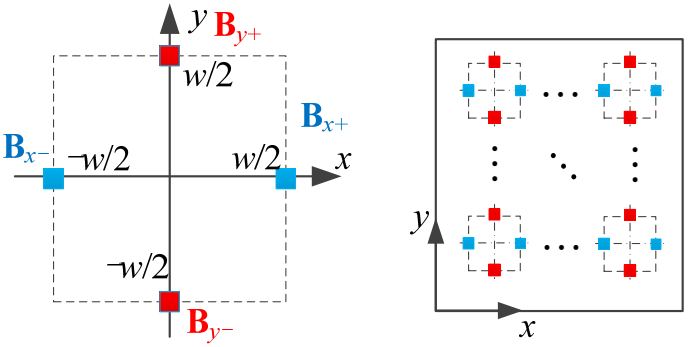

(a) Small unit measuring [**G**] (b) Sensor array with multiple units

Figure 3.1 Schematics of sensor array

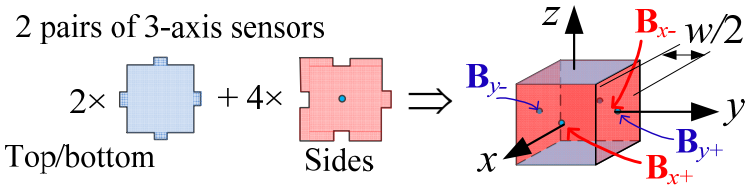

Figure 3.2 Schematics illustrating MTS

The small sensing units can be duplicated to construct a large sensor array if more measurements of magnetic tensor and MFD are needed as shown in Figure 3.1(b). The number and location of the unit are determined by the actual requirement.

To make the sensing unit measuring [**G**] compact and easy to build, a magnetic tensor sensor (MTS) which is a small cube with 2 pairs of 2-axis sensor mounted is illustrated in Figure 3.2.

For eddy-current reconstruction, a magnetic sensor array consisting of multiple sensing units is desired to measure the MFD generated by the eddy current. Figure 3.3 conceptually illustrates a sensing system for ECD field reconstruction using MFD measurements. A conductor is placed under the influence of a changing magnetic field, an eddy current represented with red dash circle will be generated. To make the eddy current flow through the whole surface area, several coils are introduced to construct an EM array. A magnetic sensor array is placed close to the conductor to measure the MFD and analyze the effect of the generated eddy current.

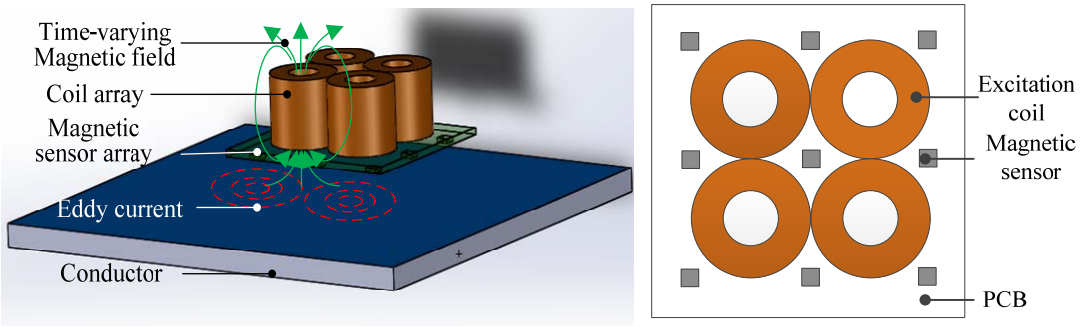

Figure 3.3 Schematics illustrating the eddy-current sensor

Figure 3.3 gives one example of a sensing system for ECD field reconstruction using a flat conductor, which consists of one 2×2 coil array and one 3×3 magnetic sensor array or four small sensing units.

3.2.2 Elimination of Unwanted Magnetic Field in Measurements

For the magnetostatic field measurement, normally, the effects of the geomagnetic field should be considered. Thereby, the total MFD **T** at a point in space consists of three contributions [9]; $\mathbf{B}_G$ due to the geo-magnetics and **B** due to man-made magnetic objects and un-modeled magnetic field $\mathbf{B}_U$:

$$\mathbf{T} = \mathbf{B}_G + \mathbf{B} + \mathbf{B}_U \tag{3.2}$$

Direct measurements of **B** are often challenging due to the relatively large earth magnetic field $\mathbf{B}_G$ ($0.5G$ at mid-latitude) which must be eliminated from measurements. However, the earth magnetic field is relatively uniform and its gradient is typically small as compared to that of the man-made object; $\left|\nabla \mathbf{B}_G\right| \approx 0.02(\text{nT/m})$ [9]; $\nabla \mathbf{T} \approx \nabla \mathbf{B}$ if $\mathbf{B}_U$ is negligible. Thus, the magnetic tensor does not contain the geomagnetic effects.

To locate and identify compact man-made magnetic objects for the VIP in presence of geomagnetic field, the properties of one magnetic object (**R** and **M**) related to the measured MFD **B** and tensor [**G**] shown in (2.13) are required.

However, besides the magnetic tensor, (2.13a) requires that **B** is measurable for locating and identifying the magnetic object. Due to the presence of geomagnetic fields as shown in (3.2), a direct measurement of **B** is impractical when the geomagnetic fields are not predictable. Instead, a sensor pair [$\mathbf{G}_{\pm}$] (spaced by known **d** such that $\mathbf{R}_{\pm} = \mathbf{R} \pm \mathbf{d}/2$) as shown in Figure 3.4 is used to locate the object from the difference of the total MFDs. Since the geomagnetic field is relatively uniform, $\mathbf{T}_{-} - \mathbf{T}_{+} \approx \mathbf{B}_{-} - \mathbf{B}_{+}$. Rewriting (2.13a) as

$[\mathbf{G}_{\pm}]\mathbf{R}_{\pm} = -3\mathbf{B}_{\pm}$ and from their difference, the object location (as viewed by the object) can be determined from (3.3):

$$\mathbf{R} = \left[[\mathbf{G}_{+}] - [\mathbf{G}_{-}]\right]^{-1}\left[3(\mathbf{T}_{-} - \mathbf{T}_{+}) - [\mathbf{G}_{-}]\mathbf{d}\right] - \mathbf{d}/2 \tag{3.3}$$

In (3.3), each of the magnetic tensors [$\mathbf{G}_{\pm}$] can be measured; and **T** is its average MFD at the sensor origin. Once **R** is known and hence its unit vector **r** and normal **n**, the magnetic moment **M** has been given in (2.13b).

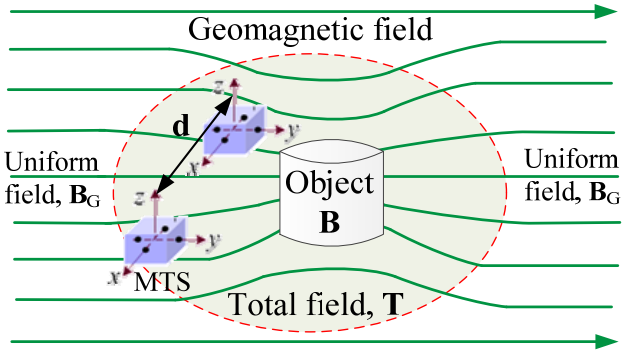

Figure 3.4 Magnetic object in geomagnetic field

The relative constant geomagnetic field can be eliminated from the sinusoidal magnetic field measurement when reconstructing ECD field. However, the direct measurements of the magnetic sensor array $\mathbf{B}_S$ consist of two components: the primary MFD $\mathbf{B}_C$ generated by the EMs and the eddy-current generated MFD $\mathbf{B}_E$ which is desired. Thereby, $\mathbf{B}_E$ can be derived using the total measurements $\mathbf{B}_S$ subtract $\mathbf{B}_C$ which can be measured by the sensor array without the conductor.

$$\mathbf{B}_S = \mathbf{B}_C + \mathbf{B}_E \tag{3.4}$$

Since $\mathbf{B}_E$ is relatively small comparing to $\mathbf{B}_C$ and the magnetic field decreases exponentially with the increase of distance, the sensor array should be placed close the conductor and cover the area where the ECD field needs to be estimated.

3.3 Sensing System Analysis

3.3.1 System Analysis for Far Field Sensing

The MTS system constructed by one sensing unit (containing 4 3-axis magnetic sensors) is analyzed for the far-field sensing.

A. Characteristics of Magnetic Tensor [**G**]

The characteristics of the magnetic tensor [**G**] can be formulated as an eigenvalue problem**:**

$$[\mathbf{G}]\mathbf{V} = [\lambda_1 \quad \lambda_2 \quad \lambda_3]\mathbf{V} \text{ where } \mathbf{V} = [\mathbf{v}_1 \quad \mathbf{v}_2 \quad \mathbf{v}_3]^{\mathrm{T}} \tag{3.5a}$$

Since [**G**] is symmetric and traceless, the eigenvalues satisfy two equations:

$$\left|[\mathbf{G}]\right| = \lambda_1\lambda_2\lambda_3 \text{ and } \lambda_1 + \lambda_2 + \lambda_3 = 0 \tag{3.5b, c}$$

For **r** pointing at the dipole, a particular **n** is normal to the plane formed by **r** and **m**; mathematically, $\mathbf{m} \times \mathbf{r} = \mathbf{n}\sin\theta$ and $\mathbf{r}^{\mathrm{T}}\mathbf{m} = \cos\theta$ As (2.12a) can be written as

$[\mathbf{G}]\mathbf{n} = P\cos\theta\mathbf{n}$, $\mathbf{n}$ is an eigenvector of [**G**] corresponding to $\lambda_1 = P\cos\theta$ which can be substituted into (3.5b,c) for solving the 2nd and 3rd eigenvalues. Hence,

$$\frac{\lambda_1}{P} = \cos\theta \text{ and } \frac{\lambda_{2,3}}{P} = -\frac{1}{2}\left(\cos\theta \mp \sqrt{5\cos^2\theta + 4}\right) \tag{3.6a, b}$$

where $|\lambda_3| > |\lambda_2| > |\lambda_1|$. A similar expression has been derived in [58] for a 2D dipole. However, unlike [58] where cosθ is expressed in terms of eigenvalues for a planar **B** field, cosθ and P can be calculated directly from the [**G**] measurements in closed-form solutions (2.8) and (2.9).

$$\mathbf{v}_1 = \mathbf{n} \tag{3.7}$$

The other two eigenvectors are solved by noting that ($\mathbf{v}_2$, $\mathbf{v}_3$) and (**r**, **m**) are on the same plane:

$$\mathbf{r} = \alpha_{-}\mathbf{v}_2 + \alpha_{+}\mathbf{v}_3 \text{ where } \alpha_{-}^2 + \alpha_{+}^2 = 1 \tag{3.8a, b}$$

$$\begin{bmatrix}\mathbf{v}_2 \\ \mathbf{v}_3\end{bmatrix} = \begin{bmatrix}b_{-}\mathbf{r} + c_{-}\mathbf{m} \\ b_{+}\mathbf{r} + c_{+}\mathbf{m}\end{bmatrix} \tag{3.8c}$$

Since $\mathbf{v}_2$ and $\mathbf{v}_3$ are unit vectors and orthogonal to each other,

$$\mathbf{v}_2^{\mathrm{T}}\mathbf{v}_2 = 1;\ \mathbf{v}_3^{\mathrm{T}}\mathbf{v}_3 = 1 \text{ and } \mathbf{v}_2^{\mathrm{T}}\mathbf{v}_3 = 0 \tag{3.9a, b, c}$$

In (3.8c), $b_{\pm}$ and $c_{\pm}$ are found in terms of $\alpha_{\pm}$ as follows. Substituting **r** from(3.8) and $[\mathbf{G}]\mathbf{v}_{2,3} = \lambda_{2,3}\mathbf{v}_{2,3}$ into (2.12b),

$$\alpha_{-}\lambda_2\mathbf{v}_2+\alpha_{+}\lambda_3\mathbf{v}_3=P\left[\mathbf{m}-3\cos\theta\mathbf{r}\right] \tag{3.10}$$

Dot multiplying (3.10) with $(\alpha_{-}\mathbf{v}_2+\alpha_{+}\mathbf{v}_3)$ leads to

$$\alpha_{-}^2\lambda_2+\alpha_{+}^2\lambda_3=-2P\cos\theta \tag{3.11}$$

Along with (3.8b), the above is solved for $\alpha_{\pm}$ in (3.12):

$$\alpha_{\pm}=s\sqrt{\frac{1}{2}\pm\frac{3\cos\theta}{2\sqrt{5\cos^2\theta+4}}}\quad\text{where } s=\pm1 \tag{3.12}$$

Each of the α_{+} and α_{-} has two solutions because of $s = \pm1$. Four independent equations for solving the unknown $b_{\pm}$ and $c_{\pm}$ in terms of $\alpha_{\pm}$ are formulated by noting that

$$\mathbf{v}_2^{\mathrm{T}}\mathbf{r}=\mathbf{v}_2^{\mathrm{T}}\left(\alpha_{-}\mathbf{v}_2+\alpha_{+}\mathbf{v}_3\right)=\left(b_{-}\mathbf{r}+c_{-}\mathbf{m}\right)^{\mathrm{T}}\mathbf{r}\ \text{ and }\ \mathbf{v}_3^{\mathrm{T}}\mathbf{r}=\mathbf{v}_3^{\mathrm{T}}\left(\alpha_{-}\mathbf{v}_2+\alpha_{+}\mathbf{v}_3\right)=\left(b_{+}\mathbf{r}+c_{+}\mathbf{m}\right)^{\mathrm{T}}\mathbf{r}$$

Using the properties of orthogonality and unit vector, the above equations can be reduced to

$$b_{\pm}+c_{\pm}\cos\theta=\alpha_{\pm} \tag{3.13a, b}$$

$$b_{\pm}^2+c_{\pm}^2+2b_{\pm}c_{\pm}\cos\theta=1 \tag{3.13c, d}$$

Equations (3.13) lead to a pair of solutions for each of the four unknowns. However, the unique solutions must satisfy the following three constraints; (3.9c), $\mathbf{m}\times\mathbf{r}=\mathbf{n}\sin\theta$ and (3.10), which are simplified and given as follows:

$$\left(b_{-}b_{+}+c_{-}c_{+}\right)+\left(b_{-}c_{+}+c_{-}b_{+}\right)\cos\theta=0 \tag{3.14a}$$

$$\alpha_{-}b_{-} + \alpha_{+}b_{+} = 1 \tag{3.14b}$$

$$\begin{cases} \lambda_2\alpha_{-}b_{-} + \lambda_3\alpha_{+}b_{+} = -3P\cos\theta \\ \lambda_2\alpha_{-}c_{-} + \lambda_3\alpha_{+}c_{+} = P \end{cases} \tag{3.14c, d}$$

It can be shown that four of the solutions to (3.13) satisfying (3.14) lead to the following unique solutions for $\theta \neq 0$:

$$c_{\mp} = \pm\alpha_{\pm} / (\sin\theta) \text{ and } b_{\mp} = \alpha_{\mp} - (c_{\mp}\cos\theta) \tag{3.15a}$$

For the case, $\theta = 0$ (**r** = **m**), (2.12b) reduces to $[\mathbf{G}]\mathbf{r} = -2P\mathbf{r}$ implying that **r** is an eigenvector. Hence,

$$\mathbf{v}_3 = \mathbf{r} \text{ and } \mathbf{v}_2 = \mathbf{v}_1 \times \mathbf{v}_3 \tag{3.15b}$$

In (3.15a), $c_{\pm}|_{s=1} = -c_{\pm}|_{s=-1}$; $b_{\pm}|_{s=1} = -b_{\pm}|_{s=-1}$ and from (3.8c), $[\mathbf{v}_2 \quad \mathbf{v}_3]^{\mathrm{T}}_{s=1} = -[\mathbf{v}_2 \quad \mathbf{v}_3]^{\mathrm{T}}_{s=-1}$. Because both eigenvectors (**v** and −**v**) satisfy (3.5a), $s = 1$ is selected in computing (3.8c).

B. Operating Range of MTS

For computing the gradient of the measured MFD, the required resolution q of the magnetic sensor-pair (space w) along an arbitrary unit-vector **N** must satisfy

$$q \le w\left|\frac{d\mathbf{B}}{d\mathbf{N}}\right| \text{ where } \mathbf{N} = a_x\mathbf{v}_1 + a_y\mathbf{v}_2 + a_z\mathbf{v}_3 \text{ and } a_x^2 + a_y^2 + a_z^2 = 1$$

From (3.5a), $\left|\frac{d\mathbf{B}}{d\mathbf{N}}\right| = \left|[\mathbf{G}]\mathbf{N}\right| = \sqrt{(\lambda_1 a_x)^2 + (\lambda_2 a_y)^2 + (\lambda_3 a_z)^2}$. $|\lambda_1|$ is the smallest implying $\min\left(\left|\frac{d\mathbf{B}}{d\mathbf{N}}\right|\right) = |\lambda_1|$ which occurs at a_x=1 and a_y=a_z=0, and **N** is parallel to $\mathbf{v}_1$. Hence,

$$q \le w \min\left(\left|\frac{d\mathbf{B}}{d\mathbf{N}}\right|\right) = w\lambda_1 \tag{3.16a}$$

For objects that can be treated as a dipole, the operating range of the MTS formulated in (3.1a, b) for a given object with magnetization **M** can be determined from (3.16a) where the smallest eigenvalue λ_1 is given by (3.6a). Hence,

$$R(x, y, z) \le \sqrt[5]{\mathbf{M}^{\mathrm{T}}\mathbf{R}(3\mu_0 w)/(4\pi q)} \tag{3.16b}$$

With **R** and **M** expressed in Cartesian coordinates, (3.16b) provides a basis for graphing the operating range of an MTS in 3D space for specified q and w.

3.3.2 System Analysis for Near Field Sensing

Sinusoidal MFD fields have been commonly used to induce eddy-current in a conductor. Thereby, the sensing system is analyzed in harmonic form.

A. Eddy Current in Harmonic Form

For applications with the sinusoidal external source, the state and output equations (3.17a, b) can be expressed in harmonic forms where $\tilde{\mathbf{B}}_E = [\mathbf{B}_{E\mathrm{Re}} \quad \mathbf{B}_{E\mathrm{Im}}]^{\mathrm{T}}$, $\tilde{\mathbf{J}} = [\mathbf{J}_{\mathrm{Re}} \quad \mathbf{J}_{\mathrm{Im}}]^{\mathrm{T}}$, the subscripts (Re and Im) denote the (real and imaginary) parts; and ω is the operating frequency:

$$\begin{bmatrix} [\mathbf{P}]+[\dot{\boldsymbol{\eta}}_{A1}]-\omega^2[\boldsymbol{\eta}_{A2}] & -\omega([\boldsymbol{\eta}_{A1}]+[\dot{\boldsymbol{\eta}}_{A2}]) \\ \omega([\boldsymbol{\eta}_{A1}]+[\dot{\boldsymbol{\eta}}_{A2}]) & [\mathbf{P}]+[\dot{\boldsymbol{\eta}}_{A1}]-\omega^2[\boldsymbol{\eta}_{A2}] \end{bmatrix} \tilde{\mathbf{J}} = \begin{bmatrix} \mathbf{0} \\ -\omega \mathbf{A}_s \end{bmatrix}$$

$$\tilde{\mathbf{B}}_E = \left[\tilde{\boldsymbol{\gamma}}\right] \tilde{\mathbf{J}} \qquad (3.17a, b)$$

where $\left[\tilde{\boldsymbol{\gamma}}\right] \left(\in \mathbb{R}^{6N_m \times 6N_c}\right) = \begin{bmatrix} [\mathbf{U}_1] & -\omega[\mathbf{U}_2] \\ \omega[\mathbf{U}_2] & [\mathbf{U}_1] \end{bmatrix}$

The (real and imaginary) parts of $\mathbf{j}_i$ and $\mathbf{B}_m$ are respectively given by $\left(j_{i\ell}\cos\theta_{i\ell}, j_{i\ell}\sin\theta_{i\ell}\right)$ and $\left(\beta_{m\ell}\cos\varphi_{m\ell}, \beta_{m\ell}\sin\varphi_{m\ell}\right)$, where $(j_{i\ell}, \beta_{m\ell})$ and $(\theta_{i\ell}, \varphi_{m\ell})$ are their corresponding (amplitude, phase) in the $\ell\left(=x, y, z\right)$ directions.

Consequently, the physical constraints and measurement model can be represented in harmonic form:

$$[\mathbf{H}_B]\mathbf{J}_{\mathrm{Re}} = 0, \quad [\mathbf{H}_B]\mathbf{J}_{\mathrm{Im}} = 0, \quad [\mathbf{H}_C]\mathbf{J}_{\mathrm{Re}} = 0, \quad [\mathbf{H}_C]\mathbf{J}_{\mathrm{Im}} = 0 \qquad (3.18a, b, c, d)$$

$$\tilde{\mathbf{Y}} = \left[\tilde{\boldsymbol{\varsigma}}\right] \tilde{\mathbf{J}} \qquad (3.19)$$

where $\tilde{\mathbf{Y}} = \left[\mathbf{B}_{E\mathrm{Re}} \quad \mathbf{B}_{E\mathrm{Im}} \quad \mathbf{0}\left(\in \mathbb{R}^{2(N_B+N_C)}\right)\right]^{\mathrm{T}}$

$$\left[\tilde{\boldsymbol{\varsigma}}\right] \left(\in \mathbb{R}^{6N_m \times 6N_c}\right) = \begin{bmatrix} -\omega[\mathbf{U}_2] & [\mathbf{U}_1] & \mathbf{0} & [\mathbf{H}_B] & \mathbf{0} & [\mathbf{H}_C] \\ [\mathbf{U}_1] & \omega[\mathbf{U}_2] & [\mathbf{H}_B] & \mathbf{0} & [\mathbf{H}_C] & \mathbf{0} \end{bmatrix}^{\mathrm{T}}$$

B. Frequency Effect on Skin Depth

As shown in (3.20) (in Table 3.1), the distribution and penetration of the induced eddy current depend on the excitation frequency f for a given material (electrical conductivity σ and relative magnetic permeability μ_r). The specific skin depth δ_d, which is

defined by the penetration depth at which the eddy current density decreases to e^{-1} (or about 37%) of its surface density, can be estimated by (3.20) in Table 3.1 where the penetration depths of the eddy-current excited with at f=50Hz alternating current for several commonly used materials are compared. In (3.20), μ_o is the permeability of free space, $\mu_o = 4\pi \times 10^{-7}$H/m.

$$\delta_d \approx \frac{(\pi \mu_o)^{-1/2}}{\sqrt{f \mu_r \sigma}} \tag{3.20}$$

Table 3.1 Penetration depth of typical materials at frequency 50Hz

Material	μ_r	σ (MS/m)	δ (mm)
Copper	1	59.98	9
Aluminum	1	37.74	12
Iron	4k	11.20	0.34
Stainless steel	1	1.14	67
Titanium	1	0.59	90

Using commercial finite element method (FEM) software, the effects of excitation frequencies on the eddy-current in a plate (at d=3mm) is illustrated in Figure 3.5, which compares the effects of three frequencies (10kHz, 100kHz and 1MHz) on the eddy-current distribution in a 1mm-thick aluminum plate.

Thereby, the dependency of skin-depth excitation frequency f for a specified material provides an effective means to meet a variety of targeted parameters in the specific applications:

– At low frequency, the full eddy-current penetration in a metal object enables measurements of the material thickness and internal defects.

– At high frequency, the eddy current distributed on the metal surface allows measurements of in-feed depth and vibration and surface integrity monitoring.

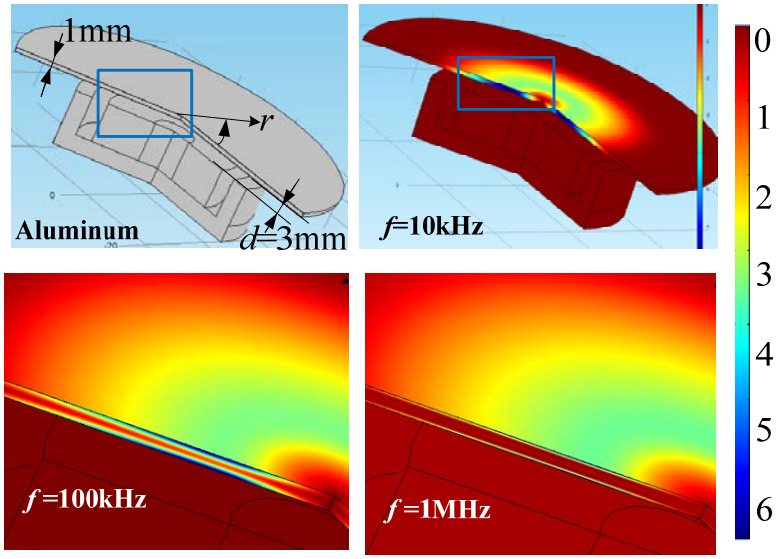

Figure 3.5 Frequency effect on eddy-current distribution

3.4 Summary

An electromagnetic sensing system which provides finite and discrete electromagnetic information at multiple desired locations to reconstruct the invisible and unmeasurable electromagnetic fields using the model of electromagnetic field reconstruction has been conceptually designed and theoretically analyzed in this chapter.

A small sensing unit of a magnetic sensor array (or MTS) consisting of two orthogonal pairs of 3-axis magnetic sensors is capable of measuring magnetic tensor and MFD and consequently used for dipole location and moment estimation. The small sensing units can be duplicated to construct a large sensor array if more measurements of magnetic tensor and MFD are required for the near-field reconstruction.

The characteristics and operating range of an MTS are introduced and theoretically analyzed for future sensing system design. Meanwhile, for near-field (or ECD field) reconstruction, the reconstruction system is simplified using harmonic form. Moreover, the distribution and penetration of the induced ECD field, which depend on the excitation frequency *f* and the conductivity of the conductor/target, have been conceptually illustrated with simulation. The principle of frequency selection is provided consequently.

CHAPTER 4. VISUALLY IMPAIRED ASSISTANCE USING MAGNETOSTATIC FIELD

4.1 Overview

To validate and evaluate the accuracy and efficiency of the designed magnetic sensing systems used for the applications of the visually impaired assistance which consists of two subtasks, arm reaching and way finding, several simulations and experiments have been performed.

4.2 Visually Impaired Assistance

Consider the subtask arm reaching, where a compact man-made magnetic object is placed in the geomagnetic field and can be treated as a dipole (with magnetic moment **M)** as viewed by the sensor, which is particularly true when the sensor is far from the magnetic object. The MFD of the compact magnetic objects (which have high magnetic susceptibility with dominant magnetization induced primarily from geomagnetic fields and negligible remnant magnetization) at a location **R** in the geomagnetic field is given by the dipole model. The method of locating and identifying the magnetic object has been presented in chapter 3 using the MTS system.

The geomagnetic field anomalies around ferrous objects placed in the relatively uniform geomagnetic field also have the potential to be used for the subtask way finding, which includes indoor navigation and magnetic obstacle avoidance. The novel MTS system designed for the subtask arm reaching are sufficient to be applied for the subtask way finding.

4.2.1 Obstacle Avoidance Using Geomagnetic Field Anomalies

Magnetic anomalies generated by objects are often difficult (if not impossible) to model because they are influenced by many factors (such as materials, shapes and their magnetic orientation relative to the geomagnetic field). Fortunately, humans do not rely on dimensionally accurate observations to make decisions as their non-contact feels are insensitive to small dimensional changes. Thus, two additional measurable parameters, Q and $d\mathbf{T}/dt$, are introduced in (2.4) and (4.1) where the dot over the variables represents their time derivatives:

$$\left|\dot{\mathbf{T}}\right| = \sqrt{\dot{T}_x^2 + \dot{T}_y^2 + \dot{T}_z^2} \tag{4.1}$$

The parameter Q indicates the relative distance between the sensor and the magnetic object; and its value dramatically increases in magnitude as the sensor approaches the object. The parameters, $\mathbf{T}$, Q and the absolute time-derivative $\left|\dot{\mathbf{T}}\right|$ in (3.2), (2.4) and (4.1) respectively, offer a means to determine the motion **Status** of the magnetic object relative to the sensor:

$$\textbf{Status} = \begin{cases} 0 & \mathbf{T} \approx \mathbf{B}_G \text{ and } \left|\dot{\mathbf{T}}\right|, Q \to 0 \\ 1 & \text{Large changes in } \mathbf{T},\ \left|\dot{\mathbf{T}}\right| \text{ and } Q \\ 2 & \mathbf{T} \to \mathbf{T}_0,\ \left|\dot{\mathbf{T}}\right| \to 0 \text{ and } Q \to Q_0 \end{cases} \tag{4.2}$$

where $\mathbf{T}_0$ and Q_0 are constants. In (4.2), the **Status** 0, 1 or 2 indicate that there is no magnetic object, a moving magnetic object, or a magnetic object but stationary, respectively.

4.2.2 Dynamic Time Warping (DTW) for Map-Following

The map-following method consists of a magnetic map, data collection and localization algorithm; the first two are closely related and inputs to the location algorithm analogous to a leader-follower approach. The leader prepares a one dimensional (1D) magnetic map along a route of interest to help the follower determine the location in real time by matching measured data with the prerecorded magnetic map. Since both the magnetic map and real-time sampled-data (that vary in time or speed under certain restrictions) are time-series with M and N elements respectively, the algorithm estimates the spatial location by evaluating similarities between the two temporal sequences to find an optimal alignment between them using a DTW method. The largest similarity implies that the magnetic samples most likely correspond to the location on the magnetic map. DTW is time-independent making it suitable for this application since travelers walk with different speeds and on varying paths.

Unlike the algorithms where numerical data are sent to machines for direct execution, the algorithm outputs qualitative information (for example, audio texts similar to that delivered to a GPS-guided car-driver) to a human who generally has the knowledge and intelligence to make better decisions. Additionally, it must be computationally robust and can be computed in real-time and embedded in a wearable device that is often limited in memory for computation. For robustness, an improved DTW method for processing multiple pairs of temporal sequences is formulated as a multi-dimensional problem to determine the 1D location along a route.

A. <u>Magnetic map and data collection</u>

Without relying on a two- or three-dimensional (2D or 3D) magnetic map which is often difficult to construct accurately, data collection along the 1D route is greatly simplified. In this method, magnetic data are pre-collected at a constant moving speed along the route of interest. The data themselves, however, do not contain location information and cannot be used for localization directly. To be effective, the magnetic data are coordinated on the floor map as *waypoints* to indicate "landmarks" (such as stair, gate and corner along a corridor) providing a reference to determine locations in real time. By mapping magnetic waypoints onto that of the floor map, spatial information is integrated to the magnetic map.

B. Improved DTW algorithm for location estimation

MTS simultaneously measures **T** (3 elements) and [**G**] (5 independent elements); each of the eight time-sequence pairs is associated with a cost. The element C_{mn} of the total cost matrix [**C**] for the m^{th} element of the map sequence ($\mathbf{x}_{\mathbf{B}m}$, $\mathbf{x}_{\mathbf{G}m}$) and the n^{th} element of the sample sequence ($\mathbf{y}_{\mathbf{B}n}$, $\mathbf{y}_{\mathbf{G}n}$) is expressed as

$$C_{mn} = \mathbf{w}_{\mathbf{B}}^{\mathrm{T}}\mathbf{d}_{\mathbf{B}mn} + \mathbf{w}_{\mathbf{G}}^{\mathrm{T}}\mathbf{d}_{\mathbf{G}mn} \tag{4.3}$$

where $\mathbf{d}_{\mathbf{B}mn} = \left|\mathbf{y}_{\mathbf{B}n} - \mathbf{x}_{\mathbf{B}m}\right|$; $\mathbf{d}_{\mathbf{G}mn} = \left|\mathbf{y}_{\mathbf{G}n} - \mathbf{x}_{\mathbf{G}m}\right|$; and $\mathbf{w}_{\mathbf{B}}$ and $\mathbf{w}_{\mathbf{G}}$ contain the weight factors which are utilized to adjust the relative importance between the MFD **B** and its gradients for location estimation. In this dissertation, the weight factors are assigned to 1. The DTW method minimizes the total cost to determine an optimal alignment p for these two (map and sample) sequences, which intuitively runs along a "valley of low-cost" within the cost matrix [**C**]. Thus, the optimal alignment is also a warping path having a minimal total cost

among all possible warping paths defined in (4.4a, b) where the subscript l indicates an element along the warping path with length L in [**C**]:

$$\mathrm{DTW}(\mathbf{x},\mathbf{y}) = \min\left\{c_p(\mathbf{x},\mathbf{y}) \middle| p \text{ is a } (M,N) \text{ alignment}\right\} \tag{4.4a}$$

$$\text{where } c_p(\mathbf{x},\mathbf{y}) = \sum_{l=1}^{L} C_{m_l n_l}. \tag{4.4b}$$

In (4.4b), $C_{m_l n_l}$ is the element chosen from each row of the cost matrix [**C**] such that the chosen L elements are connected forming a warping path. To avoid tedious computation (exponential in M and N) when finding the optimal path, an accumulated matrix [**D**] is generated; its element D_{nm} is the lowest accumulated cost or sum of the elements in [**C**] for an optimal alignment between the first n and m elements of the two sequences respectively:

$$D_{nm} = \mathrm{DTW}\left[\mathbf{x}(1:m), \mathbf{y}(1:n)\right] \tag{4.5}$$

The indices of the lowest cost path over [**D**] represent the optimally warped indices for the two time-series.

C. Illustrative example

Figure 4.1 and Figure 4.2 illustrate the leader-follower approach in the context of an indoor navigation.

In Figure 4.1(a), the red circles indicate the magnetic waypoints (table/chairs and handrails) as data are collected along the red dashed line in Figure 4.1(a, b). The symbols **a** (chair), **b** (chair), and **c** (handrail) are detected waypoints appeared in Figure 4.1(c) as local peaks on the map (red-dashed) and measured data (blue curve); only 1 of the 8 pairs

is presented to avoid repetition. To estimate the current location (blue dot) near **c**, a sample-window (width w_d) determined by the data feature and a corresponding search window (width w_m) based on the previous location (black dot) are defined, which are shaded in pink and blue respectively. The costs are computed using the sequences in the sampled-data and search windows; the lowest cost indicates the best-fit window (shaded in green) where the calculated location (red dot) corresponds to current location blue dot) in the sampled-data window.

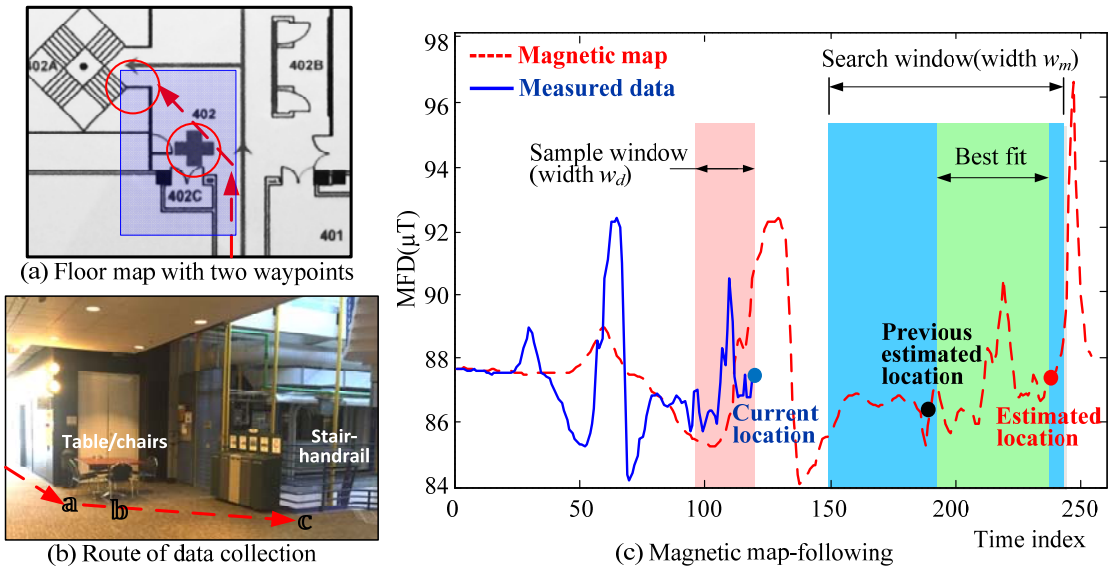

Figure 4.1 Magnetic map-following using improved subsequence DTW

The location estimations using the improved DTW subsequence are detailed in Figure 4.2(a) where the right and bottom plots of the cost matrix represent the data in sampled-data and search windows respectively. The optimal warping path (green line) for these two sequences is plotted on the accumulated matrix in Figure 4.2(b). The path covers only the cells in the matrices that exhibit low costs. With the estimated optimal path, the spatial location can be estimated.

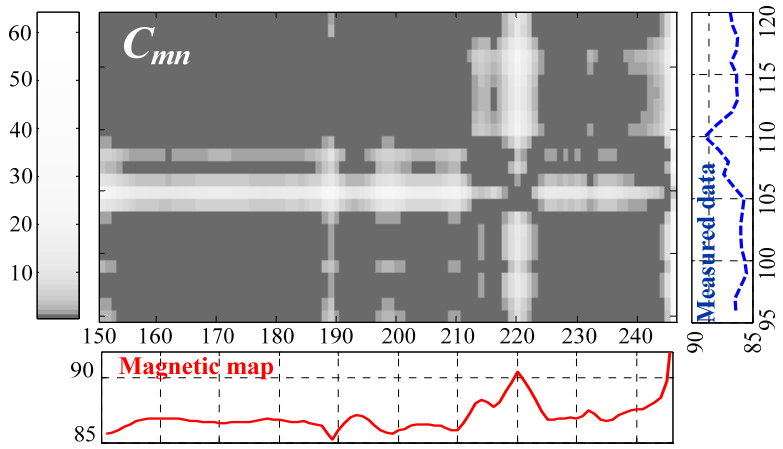

(a) Cost matrix showing relation between map and sampled-data

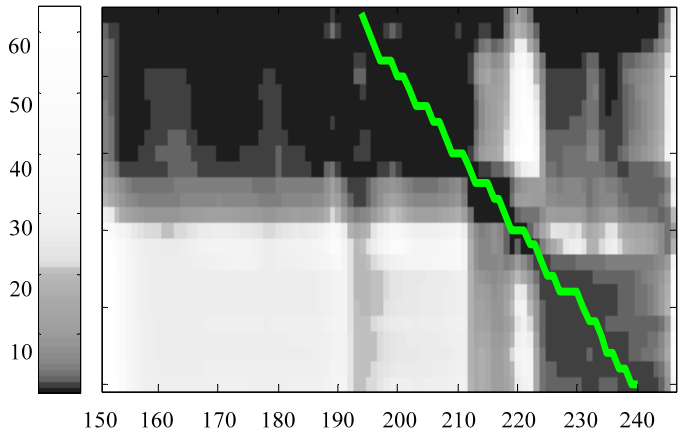

(b) Accumulated cost matrix between the map and sample

Figure 4.2 Cost and accumulated matrixes and search windows

4.3 Simulation Results and Discussion

4.3.1 Identifying Compact Magnetic Object

The formulation and the physical significance of the MTS model used in Range 1 are illustrated with a numerical example. Each MTS sensor has four orthogonally spaced magnetic sensors as discussed in (3.1a, b) where w=10mm.

For identifying the magnetic moment/location of a magnetic object, the numerical illustration involves a pair of MTS spaced d=20mm apart on a common y-axis (with one

located at the origin). In this analysis, the magnetic field of a rectangular object (50×20×10mm) with a magnetic moment **M** (0, 5, 2) Am^2 is simulated using analytical equations in Appendix C. Intuitively, this specific **M** is on the *yz* plane with its magnetic field symmetric about this plane. The magnetic object moves along a specified path relative to the sensor. With simulated measurements **B** and hence tensors **G** from (3.1a, b), the position vector **R** and moment **M** are calculated from (3.3) and (2.13b).

Four paths on the *yz* plane are simulated. Paths 1 to 4 correspond to $\varphi = 0°$, 30°, 60° and 90° respectively, where the angle φ is measured clockwise from the *z* axis. The exact MFD solutions are plotted in Figure 4.3(a); since **M** and the four object paths are on the *yz* plane, $B_x = 0$. The MFD (proportional to $1/R^3$ and singular at $R=0$) decreases dramatically with *R*. Figure 4.3 (b) shows the errors E_R and E_M which are the % difference between the simulated and exact values normalized to *R* and *M* respectively:

$$E = \frac{Simulated - Exact}{Exact} \times 100\%$$

The estimated *R* and *M* based on dipole model (2.1a) are within 10% when *R/L* is larger than 2 and 3 respectively, where *L* is the largest dimension of the object (50mm). To achieve an accuracy of less than 1% of E_R and E_M errors, *R/L* must be larger than 5 and 9 respectively.

Figure 4.4 (a) and (b) plot the calculated γ from (2.8a, b) with three different *R* values, and *P* from (2.1b) for the four paths respectively for a rectangular object and an ideal magnetic dipole with the same *M*. In Figure 4.4(a, b), the computed curves for the object nearly coincide with the dipole model, justifying dipole assumption in the range

considered and illustrating the physical significances observed in (2.1b) where P depends only on R^4 and in (2.8a, b) where γ is only a function of $\cos^2\theta$.

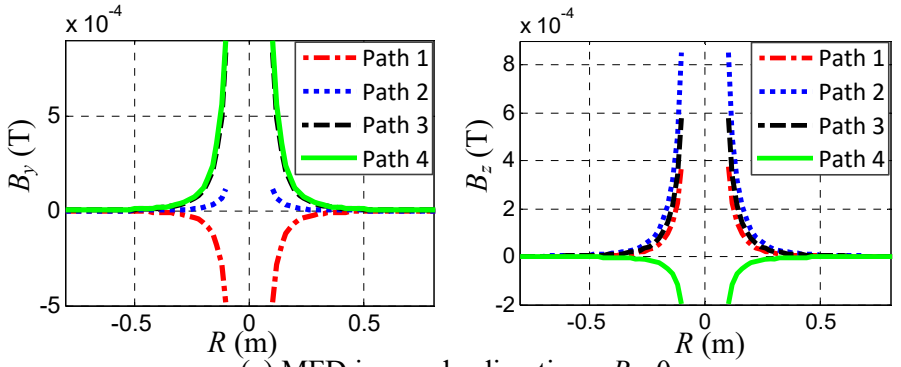

(a) MFD in y and z directions, B_x=0

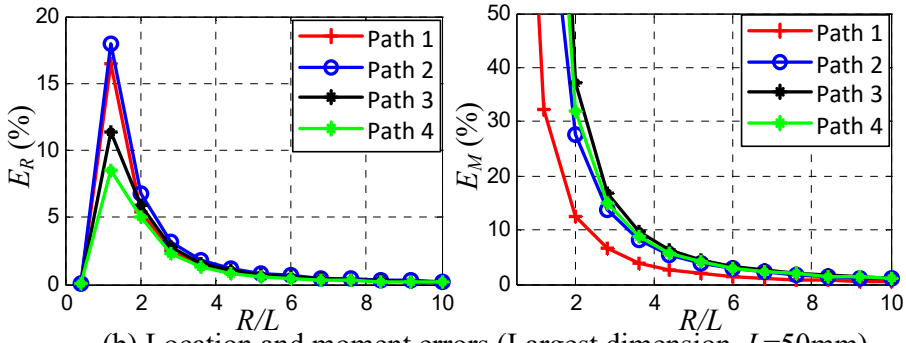

(b) Location and moment errors (Largest dimension, L=50mm)

Figure 4.3 Numerically simulated measurements

Table 4.1 Computed eigenvalues and eigenvectors, $\mathbf{v}_1 = [-1\ 0\ 0]^T$

Path	**P1**($\varphi = 0°$)	**P2**(φ=30°)	**P3**($\varphi = 60°$)	**P4**($\varphi = 90°$)
γ, θ	0.086, 111.8°	0.145, 141.8°	0.148, 171.8°	0.148, 158.2°
λ_1:λ_2:λ_3	1:2.25:−3.25	1:1.125: −2.125	1:1: −2	1 : 1.11 : −2.11
$\mathbf{v}_2^T$	[0 0.87 0.49]	[0 0.96 –0.28]	[0 –0.54 0.84]	[0 –0.13 –0.99]
$\mathbf{v}_3^T$	[0 0.49 –0.87]	[0 -0.28 –0.96]	[0 0.84 0.54]	[0 –0.99 0.13]
Path	**PA** ($\varphi = 68.20°$)		**PB**($\varphi = 21.8°$)	
γ, θ	0.1481, **180°**		0, **90°**	
λ_1:λ_2:λ_3	1 : −2 : 1		0 : 1 : 1	
$\mathbf{v}_2^T$, $\mathbf{v}_3^T$	[0 0.93 0.37], [0 –0.37 0.93]		[0 –0.92 0.39], [0 0.39 0.92]	

The magnetic tensor [**G**] can be graphically represented by an ellipsoid with its radii equal to the three eigenvalues and its orientation is characterized by the eigenvector of the largest eigenvalue. Along a path φ pointing towards the object, the (λ_1: λ_2: λ_3) ratios

and eigenvectors are constant and thus the ellipsoids maintain the same orientation and shape. As derived in (3.6), all three normalized eigenvalues (λ_i/P where i=1, 2, 3) depend on θ only. The results for the four paths are given in Figure 4.4(c) and Table 4.1.

The computation procedure for these results can be illustrated numerically by considering the instant when the object is at R=0.4m and φ=30° along Path 2. Given the simulated measurements (exact) are

$$\mathbf{B}_{i,x\pm}=\left[\pm 0.0147 \quad 2.08 \quad 14.0\right]\times 10^{-6}$$

$$\mathbf{B}_{j,y+}=\left[0 \quad 2.09 \quad 14.0\right]\times 10^{-6};\ \mathbf{B}_{j,y-}=\left[0 \quad 1.79 \quad 12.1\right]\times 10^{-6}$$

The tensor [**G**], $\left|\left[\mathbf{G}\right]\right|$ and Q can be calculated using (2.3), (2.4) and (3.1a, b):

$$(G_{xx},\ G_{xy},\ G_{xz},\ G_{yy},\ G_{yz},\ G_{zz}) = (0.491,\ 0,\ 0,\ 0.461,\ -0.446,\ -0.953)\times 10^{-4}$$

$$\left|\left[\mathbf{G}\right]\right| = -3.1345\times 10^{-13},\ Q = 8.214\times 10^{-9}$$

The characteristic parameters (γ, P, θ, λ_i, $\mathbf{v}_i$) can be calculated from (2.8), (2.9), (3.6), (3.7) and (3.8c):

$$P=6.088\times 10^{-5};\ \gamma=0.1445;\ \theta=141.25°;$$

$$\begin{bmatrix}\lambda_1\\ \lambda_2\\ \lambda_3\end{bmatrix}=\begin{bmatrix}4.91\\ 5.9\\ 10.8\end{bmatrix}\times 10^{-5};\ \mathbf{v}_1=\begin{bmatrix}1\\ 0\\ 0\end{bmatrix},\ \mathbf{v}_2=\begin{bmatrix}0\\ 0.961\\ 0.278\end{bmatrix},\ \mathbf{v}_3=\begin{bmatrix}0\\ -0.278\\ 0.961\end{bmatrix}$$

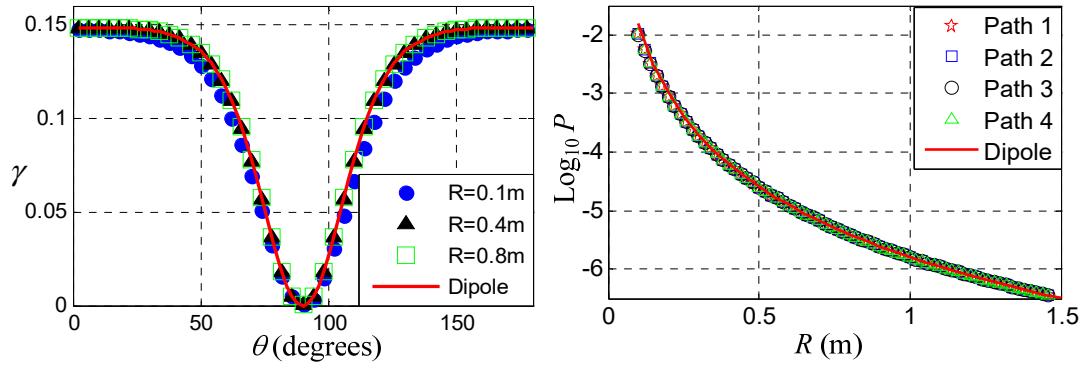

(a) Distance-insensitive parameter, γ (b) Orientation-insensitive parameter, P

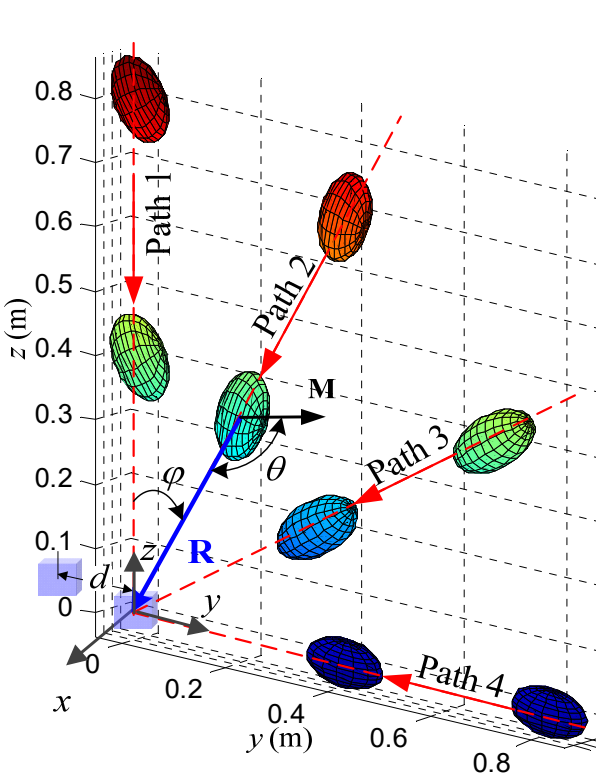

(c) Ellipsoid representation of measure [**G**]

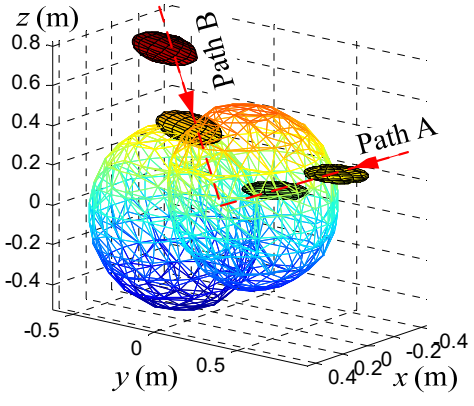

(d) Sensing range in 3D space

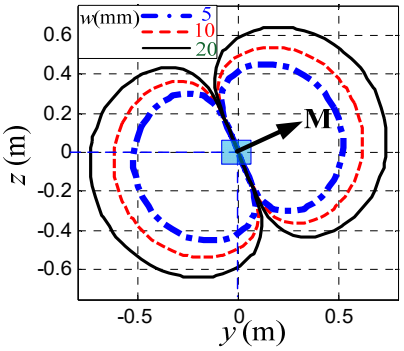

(e) Sensing range on yz plane

Figure 4.4 MTS characteristics and operating range

The characteristic parameters for the other paths, which can be calculated similarly are graphically displayed in Figure 4.4(c, d). In Figure 4.4(d), Paths A and B are two special cases where $\theta = 180°$ (parallel to **M**) and 90° respectively; the ellipsoid (representing the eigenvalues) of the latter is essentially a plane circle ($\lambda_1 = 0$) as shown in Table 4.1. As an illustration, the operating range of the MTS (w=10mm) consisting of four MFD sensors

(q=10^{-7}T) for detecting the rectangular object is numerically computed using (3.16b) and graphed in Figure 4.4 (d). in Figure 4.4(e) helps visualize the effects of w on the sensing range which is projected on the yz plane. The sensing range is symmetric about Path A (along **M)** and Path B (λ_1 =0 that corresponds to the smallest MFD gradient along $\mathbf{v}_1$).

4.3.2 Magnetic Obstacle Avoidance

Only one MTS which is the same as that used in Subtask arm reaching is involved in Subtask way finding. Magnetic obstacle avoidance using geomagnetic field anomalies will be numerically illustrated in this section whereas indoor navigation will be directly evaluated using experiments in the next section.

The physical significance of the orientation-insensitive parameter Q used for obstacle avoidance is best illustrated with FEM numerically using commercial software, COMSOL. Many outdoor objects (such as fire hydrants, poles and traffic sign-posts) as well as indoor objects (like handrails) can be characterized as cylindrical steel objects which are thus chosen here for illustration.

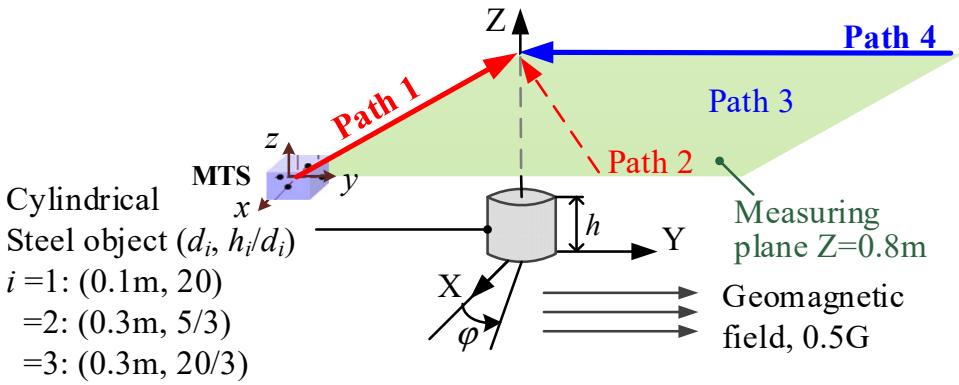

(a) Parameters used in simulations

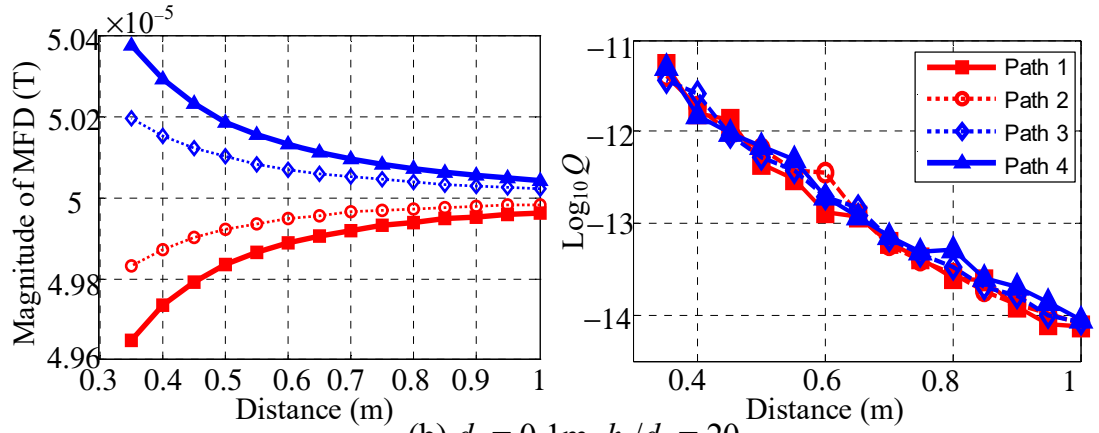

(b) $d_1 = 0.1$m, $h_1/d_1 = 20$

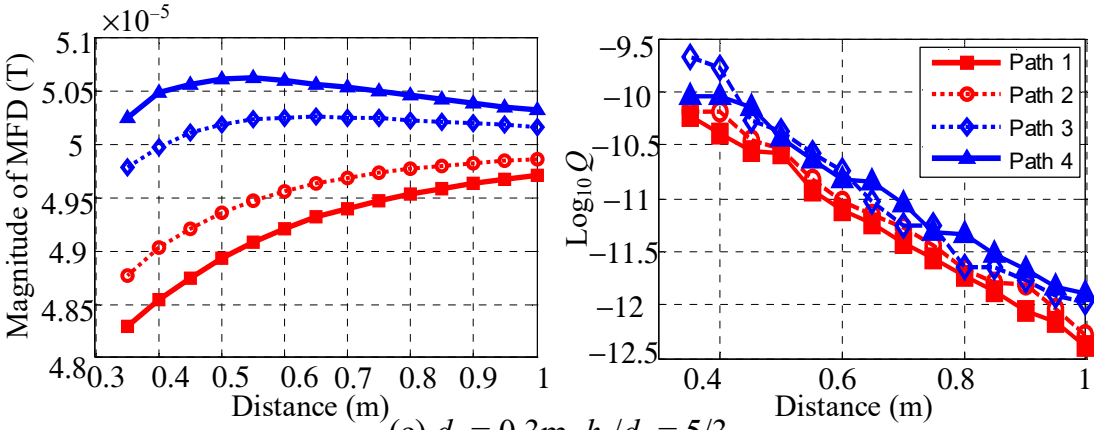

(c) $d_2 = 0.3$m, $h_2/d_2 = 5/3$

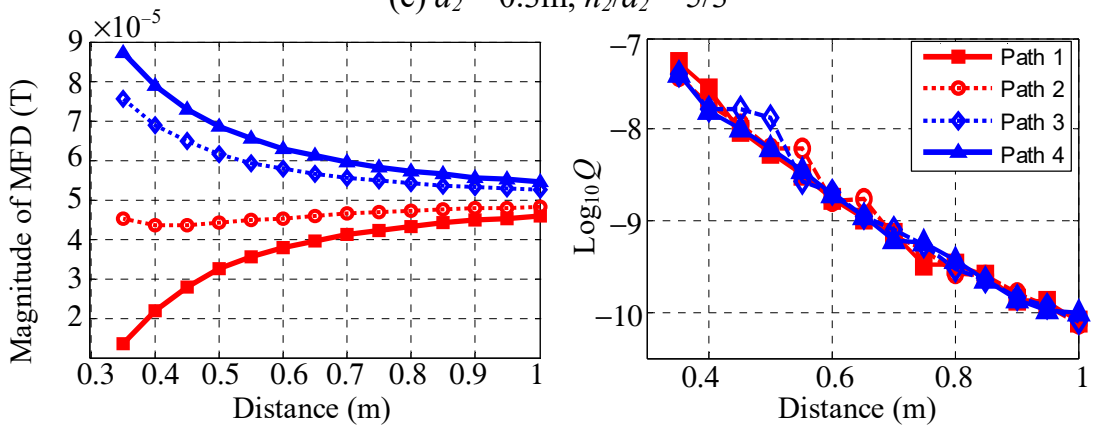

(d) $d_3 = 0.3$m, $h_3/d_3 = 20/3$

Figure 4.5 Schematics and simulations showing effects on MFD and Q

As illustrated in Figure 4.5(a), the steel object (where the XYZ coordinate system is assigned) is stationary in the uniform geomagnetic field (0.5G pointing in the Y direction). In order to comprehensively describe the geomagnetic field effects on the steel

object, four different paths along which the MTS (at Z=0.8m) moves towards the object are simulated. The paths are denoted by φ= 0°, 30°, 60° and 90° measured clockwise from the X axis in Figure 4.5(a). Simulation results are presented in Figure 4.5(b, c, d) where MFD and Q are plotted as a function of the distance traveled, from which some observations are made:

- As Q is inversely proportional to a high-power of the distance between the MTS and the magnetic object [59], its values are graphed in a $\log_{10}$ scale for clarity. As the MTS moves near the object, $\log_{10} Q$ increases approximately linearly but is path-insensitive particularly for objects with a large aspect-ratio ($h/d \geq 5$). Unlike Q, the MFD and its gradient (magnitude/direction) are path-dependent.
- Q approaches zero monotonically as the MTS is far from the object in all cases whereas the measured MFD approaches a constant value equal to the geomagnetic field.

4.4 Experimental Results and Discussion

4.4.1 Experimental Setup

Figure 4.6 illustrates the design prototype of an MTS and the applications of the way finding and guiding visually impaired person. When a magnetic object is in space, the earth- magnetic (or geomagnetic) field around it is "distorted". This distorted field can be used to derive information in the immediate surroundings of the VIP. However, the geomagnetic anomaly is difficult to be evaluated using direct MFD measurements. Thereby, the magnetic tensor [**G**] is utilized to interpret the geomagnetic effects. In addition, magnetic sensors in digital format are chosen to minimize the noise effect. Figure 4.6(b) shows a prototype MTS consisting of two orthogonal pairs of digital 3-axis magnetic

field sensors (BMC050) mounted at $\pm w/2$ (where w=10mm) from the x and y axes of the sensor local coordinate system. Packaged in a small footprint, BMC050 [60] has a relatively large measurement range, high resolution, low output noise, and low energy consumption; see Table 4.2. In operation, the MTS communicates with a laptop PC through an inter-integrated circuit (I^2C) bus and a USB adaptor, where the MTS output signals are filtered using a 1D median filter to remove noise.

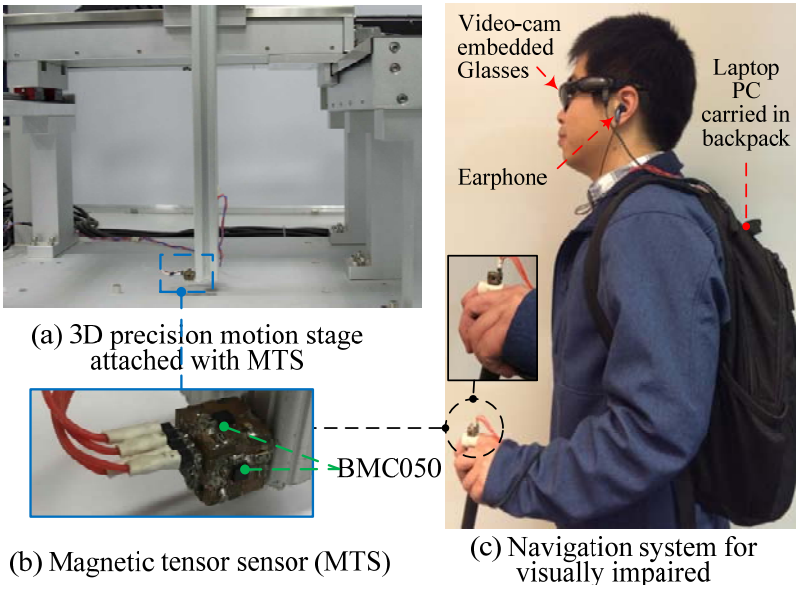

Figure 4.6 Schematics illustrating MTS-based sensing system

To precisely validate the methods of magnetic object localization and identification, the MTS is first attached to the 3D precision motion stage as shown in Figure 4.6(a). As will be shown, the MTS can effectively supplement image-based information to improve the indoor/outdoor navigation of the visually impaired user. Carried in a backpack by the VIP as shown in Figure 4.6(c), the MTS-measurements (with data from GPS and wearable camera) provide the user with surrounding information (by means of an earphone and/or stimulator).

MTS was calibrated with the procedure and results described in Appendix D to eliminate the effect of different scale factors and misalignment errors of four magnetometers. The calibration results are given in (D.5a, b, c); the maximum misalignment (estimated from the off-diagonal terms) is within 5° which could be due to a combination of sensor noise, geometrical and positioning errors. MFD data (ranging from 0 to 200μT) were sampled at a rate of 20Hz. The average standard deviation for the four magnetometers was found to be 0.162μT.

Table 4.2 Sensor parameters

Three-axis magnetic sensor Model: BMC050		**Wearable digital video camera** Model: POV ACG-20	
Size (mm)	3×3×0.95h	Resolution (pixels)	1280×1024 (image)
Range(μT)	±1000		640×480 (video)
Resolution (μT)	0.3 (at 20Hz)	Frame rate	30 frames/s (FPS)
Output noise (μT)	0.3	Connection	Mini USB

4.4.2 Arm Reaching

Experiments were conducted on two different types of compact objects. The first object is a uniformly magnetized cylindrical PM commonly used as an "engineered landmark" for machine applications, where the interest is to accurately determine **M** and/or **R**. The second object is an example of a general ferrous object with a non-uniform shape to illustrate the detection and approximate localization of a ferrous object for applications such as visually impaired assistance.

4.4.2.1 Uniformly magnetized cylindrical PM

For a PM with uniform magnetization $\mathbf{m} = [0 \quad 0 \quad 1]^T$, the eigenvectors corresponding to the minimum and maximum eigenvalues are along the *y* (radial) and *z*

(axial) axes. As a basis for illustration, their corresponding inverse solutions are derived analytically from (2.1a):

1) Radial $x=z=0$ and $y \geq r_o (\neq 0)$,

$$y = \sqrt[3]{\frac{\mu_0}{4\pi}\left(\frac{M}{-B_z}\right)} \text{ or } M = \frac{4\pi y^3}{\mu_o}\left(-B_z\right) \tag{4.6a, b}$$

2) Axial $x = y = 0$ and $z \geq r_o (\neq 0)$,

$$z = \sqrt[3]{\frac{\mu_0 M}{2\pi B_z}} \text{ or } M = \frac{2\pi z^3}{\mu_o} B_z \tag{4.6c, d}$$

More general solutions to the inverse model can be numerically obtained using MATLAB function *fsolve* to solve the nonlinear equation (2.1a) with the Trust-region-dogleg algorithm[61].

For validating the MTS, the MFD and its tensors of a cylindrical PM (radius r_o) with a unit aspect ratio (length=diameter=$2r_o$) were determined experimentally. To experimentally simulate an MTS with w=4mm, the MTS was attached to a 3-axis translational stage (1μm resolution in each axis) but only one of 4 magnetic sensors was used. For each **R**, five points (center and four neighbors at ±2mm from the center) were measured. The magnetic field **B** of the compact object was isolated by eliminating $\mathbf{B}_G$ from measurements. The measured geomagnetic field (without object) was found to be relatively constant:

$$\mathbf{B}_G = \begin{bmatrix} -40.04 & -3.49 & 3.89 \end{bmatrix}^{\mathrm{T}} \mu\mathrm{T}.$$

With $\mathbf{B}_G$ subtracted from data, the experimentally measured B_z and gradient parameter Q along the y and z axes for two different sized magnets are plotted in Figure 4.7(a, b) where the dashed lines are analytical solutions based on the dipole approximation,(2.1) and (2.7). Equations (2.13b) and (3.3) were then used to calculate the two unknown vectors, **M** and **R**, along the radial and axial axes. The estimated M and errors of the estimated R are given in Figure 4.8. Figure 4.9 shows the corresponding characteristic parameters (P; λ_1, λ_2, λ_3) of the measured (**B**, Q). In Figure 4.7 to Figure 4.9, specific (B_o, Q_o, M_o, P_o) values for normalizing the graphed variables are computed at y (or z) equal to 31mm; and the abbreviations are as follows:

LM: Large magnet ($2r_o$ = 9.63mm); and

SM: Small magnet ($2r_o$ = 5.92mm).

The MTS is compared with two other commonly used methods (single-sensor and dual-sensor). The following three cases are compared in Table 4.3:

Case 1 (C1): **R** is determined from a single measurement with known **M**.

Case 2 (C2): **M** is determined from a single measurement with known **R**.

Case 3 (C3): Both **M** and **R** are simultaneously determined based on the dipole approximation from a pair of measurements.

G: No assumptions on the dipole approximation but the parameters are determined using the MTS.

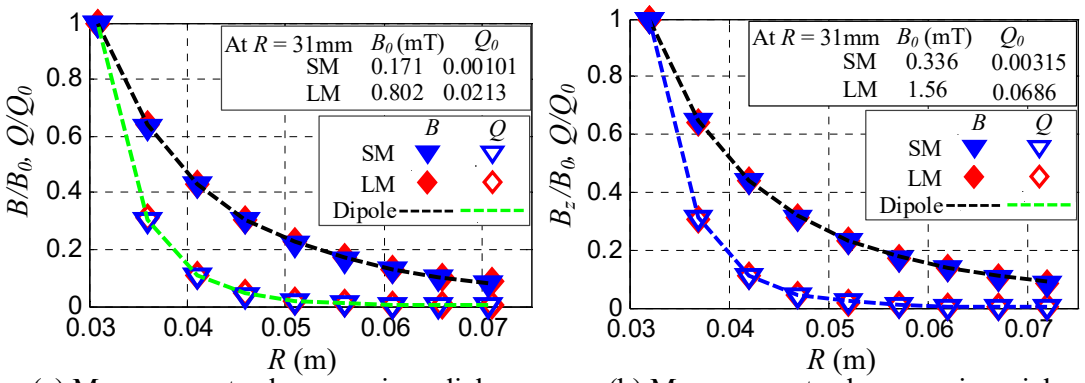

(a) Measurements along *y*-axis, radial (b) Measurements along z-axis, axial

Figure 4.7 Experimentally measured MFD B and gradient parameter Q

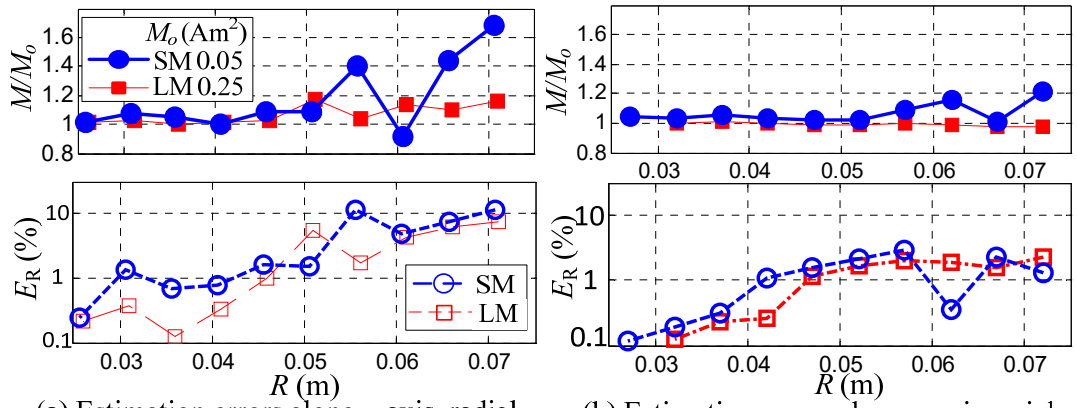

(a) Estimation errors along *y*-axis, radial (b) Estimation errors along z-axis, axial

Figure 4.8 Percentage errors of estimated R and moment M

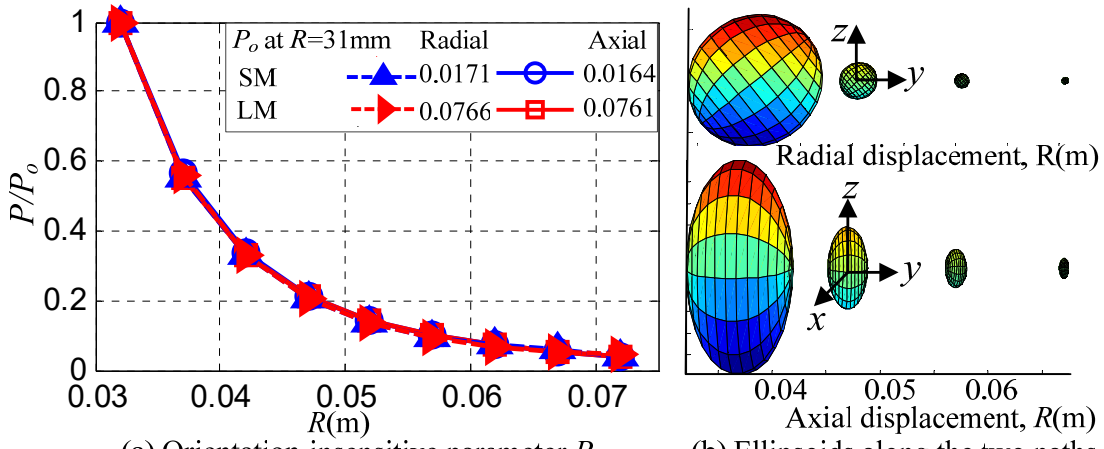

(a) Orientation-insensitive parameter P (b) Ellipsoids along the two paths

Figure 4.9 Characteristics of measured magnetic tensor [**G**]

Table 4.3 Comparison of estimation errors among different methods

		Location	*y*=36mm	*y*=61mm	*z*=36mm	*z*=61mm
C1 (E_R), Known **M**, LM (WO)			(4.6, NA)	(2.6, NA)	(2.7, NA)	(0.8, NA)
C2 (E_M), Known **R** , LM (WO)			(NA, 3.8)	(NA, 2.3)	(NA, 2.6)	(NA, 2.4)
C3 (E_R, E_M)	LM (W)		(28, 65)	(79, 99)	(42, 65)	(8.9, 56)
	LM (WO)		(1.2, 1.6)	(2.9, 4.2)	(0.8, 1.4)	(1.3, 1.2)
G (E_R, E_M)	SM (W/WO)		**(0.6, 0.5)**	**(4.8, 5.2)**	**(0.3, 1.2)**	**(2.3, 1.9)**
	LM (W/WO)		**(0.1, 1.1)**	**(4.2, 4.8)**	**(0.2, 0.8)**	**(4.2, 2.1)**

In Table 4.3, W indicates original measurements containing geomagnetic field $\mathbf{B}_G$; and WO indicates that data are the magnetic field **B** of the compact object (without geomagnetic fields which were subtracted from measurements).

Observations made from the results are discussed as follows:

1) For a constant **M**, **B** and Q are inversely proportional to R^3 and R^8 respectively. For $R/(2r_o) > 3$, measured data in Figure 4.7(a, b) well agree with (4.6) and (2.7):

$$B_z(0,0,R) = -2B_z(0,R,0) \text{ and } Q(0,0,R) = 3Q(0,R,0)$$

Figure 4.8 shows that as **B** decreases the estimation errors in R and M increase. For the same distance, the estimation errors for LM are lower than that for SM and are also lower along the axial direction than that along the radial direction, which are because of the stronger magnetic fields. Less than 2% estimation errors of R and M can be obtained in the range $3 \le R/(2r_o) \le 4.8$ for LM, beyond which measurement errors increase as the generated magnetic field decreases dramatically.

2) Unlike the direct **(B**, Q) measurements which depend on paths (radial and axial), all data of the orientation-independent P collapse into a single curve in Figure 4.9(a).

As shown in Figure 4.9(b), the ellipsoids (3.6a, b) along the radial direction are disc-like (λ_1=0) indicating no change in the gradient of B_z with respect to x circumferentially; this is expected for an axially magnetized PM. The disc rapidly decreases in size because (λ_2, λ_3) are inversely proportional to R^4, and approaches the shape of a circle indicating similar changes in B_z gradient with respect to y and z.On the other hand, the ellipsoids along the axial direction are elongated with (λ_3=2λ_2=2λ_1) indicating that the change in the B_z gradient is symmetric with respect to x and y, and maximum along the z-axis.

3) The MTS performance is quantitatively evaluated at two specified locations (R=36 and 61mm) for LM in Table 4.3 by comparing against commonly used methods (which rely on direct **B** measurements). With appropriate assumptions (Cases 1 or 2) and geomagnetic field subtracted from measurements, both single and dual sensor methods work well within the operating range of the dipole model. In general, two or more 3-axis sensors are needed to simultaneously determine all six parameters of **R** and **M** in Case 3 where the assumption of known **R** or **M** is relaxed. However, these traditional methods **B**- measurement only generally require a prerequisite of subtracting the geomagnetic field from measurements; which are often clumsy as it is difficult to maintain consistent alignments between two different sets of measurements. Additionally, **R** and **M (**for Case 3) must be simultaneously solved from the inverse model of (2.1a); the associated problems of multiple solutions and convergence often make these methods unstable and difficult to implement in practice.

The MTS offers an effective means to determine **R** and **M** in the presence of the geomagnetic field. As shown in the last two rows in Table 4.3, the errors in the estimated

R for SM and LM at location *R*=36mm are 0.6% (0.2mm) and 0.1% (36μm) along the *y*-axis, and 0.3% (0.1mm) and 0.2% (72μm) along the *z*-axis respectively; these results represent nearly an order-of-magnitude improvement over methods based on direct **B** measurements. However, the estimation errors at *R*=61mm vary approximately from 2% to 5%, and are in the same order-of-magnitude as its counterparts.

The effect of *w* on low accuracy at large *R* can be explained as follows: As **G** is computed from the difference between **B** measurements, exact gradient calls for an infinitesimally small *w* demanding a sufficiently high sensor-resolution to discriminate the very small change of MFDs. In practice, the accuracy and range of the MTS are limited by the magnitude of **B** being measured, and the physical size and resolution of the 3-axis sensors; both impose a lower limit on *w*.

4.4.2.2 General ferrous object with non-uniform shape

As an illustration, a wrench (made of ferrous material) was placed on a table in this experiment as shown in Figure 4.10(a), where the geomagnetic field was measured to be

$$\mathbf{B}_G=\begin{bmatrix}-41.77 & -3.42 & -4.46\end{bmatrix}^{\mathrm{T}}\ \mu\mathrm{T}.$$

To facilitate applications, two MTSs (separated by a distance *d*=20mm) were utilized to eliminate the geomagnetic field effect on localization, where the reference frame *x*-*y* is defined on one of two MTSs.

As the wrench that has an irregular shape and a length *L*=150mm, its lumped-parameter model as a magnetic dipole would gradually deviate from exact solutions

especially when the sensor is very close to the object. To relax the assumptions that limit the localization, experiments were conducted to identify key parameters and develop methods to characterize the location and orientation of an irregular magnetic object from the measured total-MFD **T** and tensor **G** defined in (3.2) and (2.2a) respectively:

Method 1 (M1) indirectly estimates the magnetic moment **M** and the location **R** from the inverse model of a dipole approximation in (2.13b) and (3.3) respectively.

Method 2 (M2) uses the parameters (P, γ) to gauge the closeness of the magnetic object and to provide an estimation of its orientation. Two different ways of computing (P, γ) are compared:

(M2a): P is calculated from (2.1b) where (**M**, **R**) are obtained from M1. γ is analytically calculated from (2.8a).

(M2b): As defined in (2.8a), γ is experimentally found from measured $|\mathbf{G}|$ and Q. P is determined from (2.9) with θ approximated from (2.8d).

Unlike the methods (M1, M2a) derived from a dipole model, the method M2b directly computes (P,γ) experimentally.

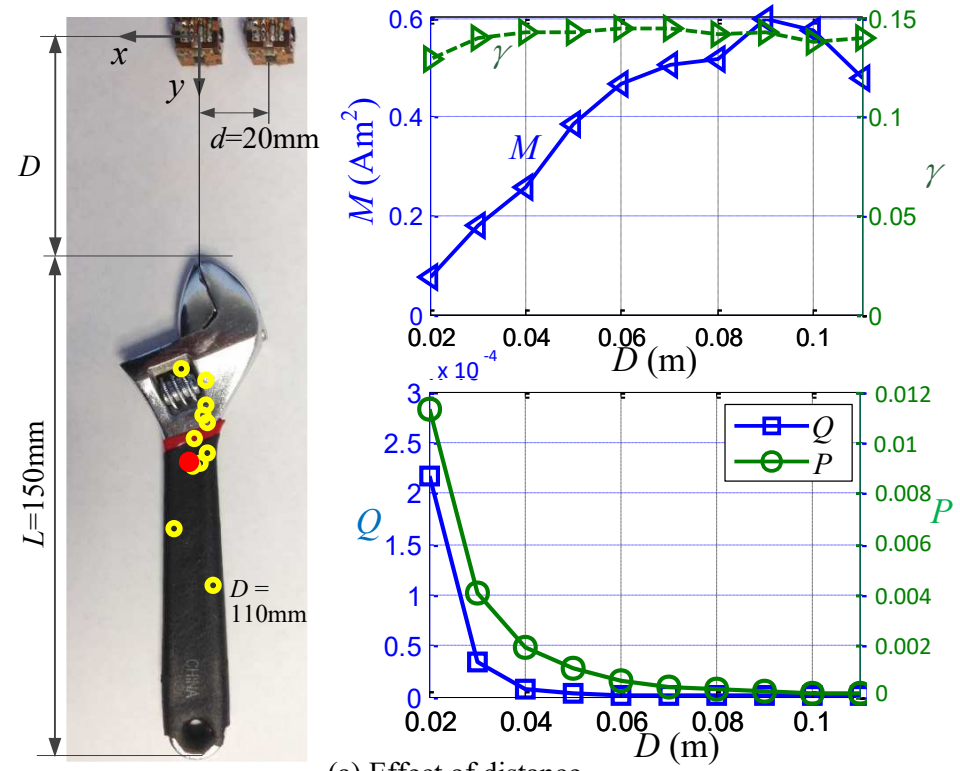

(a) Effect of distance

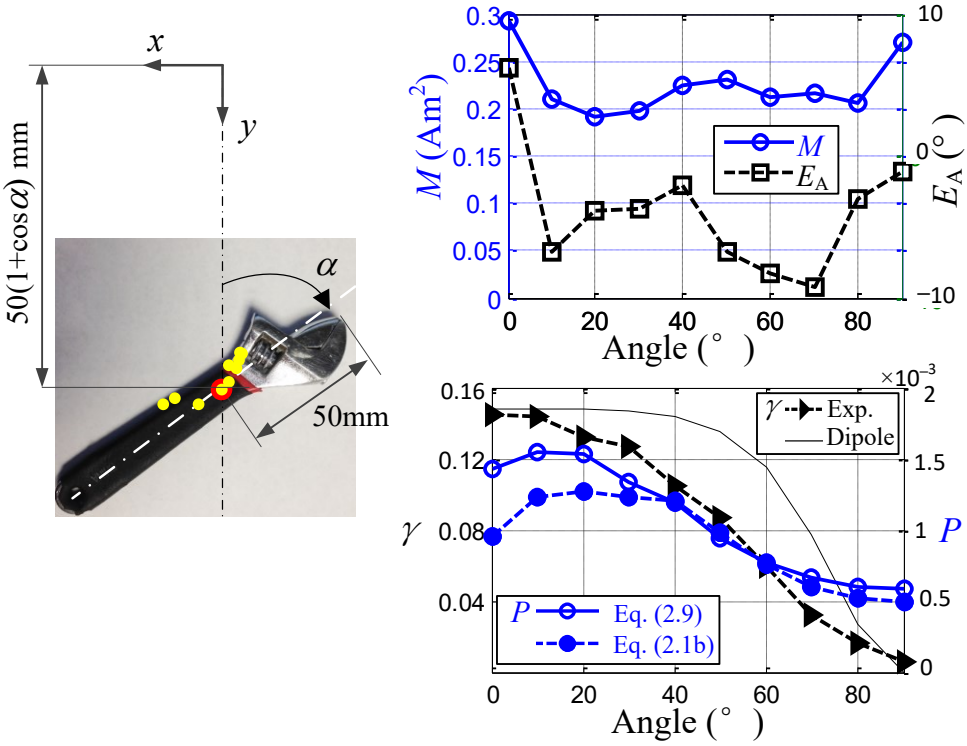

(b) Effect of orientation

Figure 4.10 MTS for [**G**] measurement

The effects of different methods on the estimation of the location and orientation for two different cases (Cases A and B) are compared in Figure 4.10(a, b) where the superimposed (yellow colored) circles on the images are the estimated locations **R** using M1. In Case A (Figure 4.10a), the pair of MTSs move towards the wrench (fixed) in the *y* direction while **T** and [**G**] were measured along the path. Figure 4.10(a) plots the computed *M*, and the experimentally measured (γ, *Q, P*) as a function of the distance *D* between the sensor and the tip of the wrench. Case B (Figure 4.10b) analyzes the effect of the orientation with respect to the pair of MTSs placed at 50mm from the rotational center (red-colored) circle about which the wrench was rotated ($0° \le \alpha \le 90°$). Figure 4.10(a, b) offer some insights for magnetically characterizing the location and orientation of an irregular magnetic object:

1) In Figure 4.10(a), *M* (that should be a constant for a given object) varies with the distance *D*, showing that the dipole model is a poor approximation for the wrench when $D<2L$. For the same reason, the analytically calculated γ in Figure 4.10(b) deviates from experimental measurements. However, the equivalent locations **R** (indicated as circles in images) are all located within the wrench; this provides a rough but practical position-estimation for locating the wrench.
2) The experimentally obtained γ is largely constant in Figure 4.10(a) and decreases monotonically from 0.15 to 0 as α rotates from 0° to 90° in Figure 4.10(b); these results confirm that γ depends only on θ. On the other hand, *P* increases drastically as *D* decreases and is insensitive to orientation.

The above results suggest that the measurable (γ, P) parameters offer an excellent alternative to (**M**, **R**) for magnetically characterizing the location and orientation of an irregular magnetic object when the dipole model is a poor approximation.

4.4.3 Way Finding

The performance of the prototype MTS (Figure 4.6b) and navigation system (Figure 4.6c) has been experimentally evaluated involving both indoor and outdoor applications. The flowchart (Figure 4.11) shows the relations among the magnetic map, magnetic/vision data collection and localization algorithms for the indoor (E1) and outdoor (E2) navigation examples. In E1, vision images are utilized to predict and identify an upcoming critical waypoint (such as a stair) or danger whereas in E2, vision images are introduced to extract and locate moving vehicles and zebra crossings. In both indoor and outdoor experiments, the MTS is attached to the VIP (at a height approximately 0.6m from the floor/ground); and the MTS coordinate system is defined such that its y-axis points to the moving direction. As will be shown, when coupled with information derived from images, magnetic information can significantly improve the safety of the blind user.

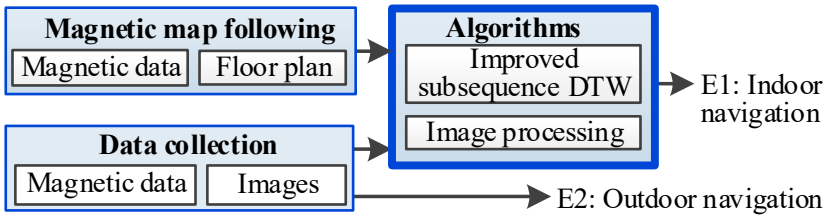

Figure 4.11 Flowchart illustrating MTS-based applications

4.4.3.1 Magnetic map following for indoor navigation

Figure 4.12 shows the emergency excavation route (Figure 4.12a) of an office building and the magnetic map (Figure 4.12b) for a VIP to follow, which provides the environment for the indoor navigation experiment to evaluate the prototype MTS and the location algorithm. The symbols ① to ⑧ indicating the waypoints (red numbers in Figure 4.12a), which are specified landmarks and alert critical and dangerous locations along the path from Room 474 (red star) to the stair (red dot), are defined in Table 4.4 and Figure 4.12 (c, d).

A. Geomagnetic waypoints

Table 4.4 illustrates three different types of geomagnetic waypoints which are defined before data collection: The first type is characterized by magnetic property in an object or a structure, which may be general steel or embedded components such as reinforced bars in a concrete pillar or column. The second type exists by virtue of its current-induced magnetic anomaly; the electrical closet ② where power lines, electrical equipment and network switches are housed is a good example. The third type is caused by the changes in sensor orientation relative to the uniform geomagnetic field without a magnetic anomaly (because geomagnetic field effects are directional); for example, the corner along the corridor ④ is a non-magnetic waypoint which helps locate the direction change. Unlike the 1st or 2nd type waypoint at which the specified location is defined, Waypoint ④ has little anomalies in the area but can be detected by the sensor after an actual geographical change in direction has taken place. For simplicity, only the MFD components along the route are shown here on the magnetic map in Figure 4.12 (b) which shows several significant MFD changes due to the magnetic waypoints marked in the pink-

shaded window. The field changes at ④ and ⑥ are caused by the changes in sensor orientation relative to the uniform geomagnetic field, and that in ① to ③ and ⑤ are due to magnetic objects.

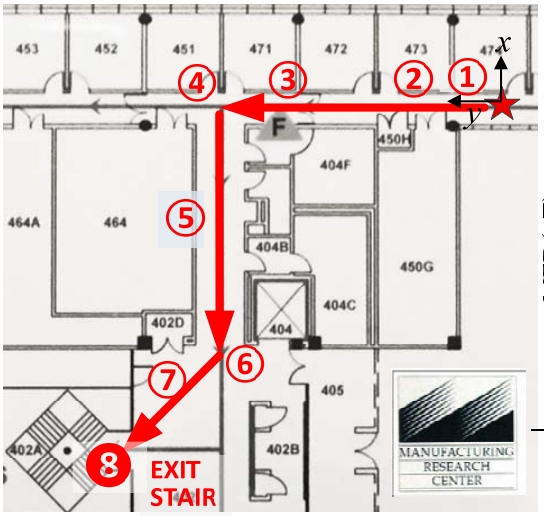

(a) Floor plan for emergency evacuation route

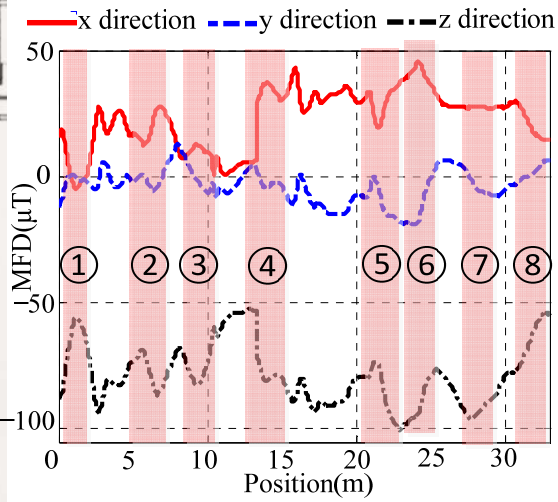

(b) MFD along the route

(c) Objects along the route: pillars ①, ③, electrical closet ② and dispenser ⑤

(d) Critical waypoint along the route: stair ⑧

Figure 4.12 Schematics showing path/waypoints for indoor experiments

Table 4.4 Description of waypoints

①Pillar	②Electrical closet
③Pillar/Steel door frame	④Corner along the corridor
⑤Water dispenser	⑥End of corridor (elevator with first-aid box)
⑦Table and chairs	⑧Stair with steel handrails

With the magnetic map, the localization algorithm described in chapter 3 was utilized to estimate the actual location using measured **T** and [**G**]. The concept feasibility of the MTS-guided indoor navigation is evaluated by computing the errors of the estimated locations with respect to the actual locations. Based on four data sets collected along the route, the mean errors and their ranges at the eight waypoints are plotted in Figure 4.13, the standard deviation of all experimental data is 81mm; and the position errors at stair-waypoint ⑧ are within ± 0.075m.

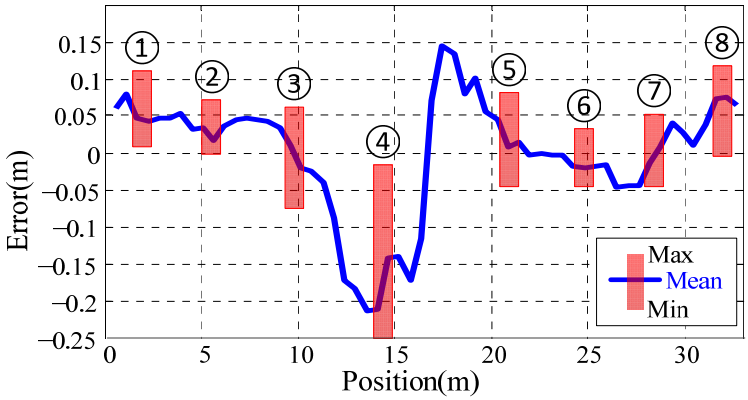

Figure 4.13 Position errors

As shown in Figure 4.13, the largest error occurs at ④ where the magnetic anomalies (or changes) are relatively small. The positive peak between Waypoints ④ and ⑤ is associated with the error in the corner ④ which is utilized to extract specified spatial/orientation information. In this method, the sensing system with its DTW algorithm

uses the most recently collected data to estimate the current location and anticipate the corner-waypoint. Since the four different trails were not on the exact same path and did not make the left-turn on the same location and walk with the same speed, the variations in the estimation results (after the left-turn has actually occurred) should be expected. In this specific example, this specific waypoint represents a left-turn along the specified path from a 1.65m-wide corridor to a 2.5m-wide corridor; in other words, the positive peak (0.15m error) is less than 6% of the 2.5m range within which the VIP may make the turn. These results demonstrate the robustness and efficiency of this method.

B. Image-enhanced waypoints for dangerous Location

Unlike the corner-waypoint ④ where some position errors around it are acceptably safe, position errors at stair-waypoint ⑧ could be dangerous for a VIP. To help guide the VIP stepping down the stairs safely, additional image-based data that offer predictive information are used to enhance the magnetic map by including the falling floor-edge and black-colored handrail as waypoint characteristics at ⑧. Without loss of generality, the widely known Hough-transform (HT) line-detection [62] and principal component analysis (PCA) color-classification vision algorithms [63] are used to characterize the falling floor-edge of the stairs (Figure 4.14) and black-colored handrail (Figure 4.15) in images captured by the wearable camera.

Figure 4.14 illustrates the HT procedure (with ρ and θ as parameters in the straight-line equation) to define the path and detect the falling floor-edge. The procedure begins with searching in the two regions for the left and right side-lines ending at the floor-edge; $20° \le \theta \le 75°$ and $-75° \le \theta \le -20°$. Figure 4.14(a, b) show the edge detection and HT

results, where the two peak values that characterize the (ρ, θ) parameters of the left and right side-lines occur at (774, 55.3°) and (−219, −61°). To locate the falling edge, a second HT is performed within the enclosed area bound by the two side-lines and a horizontal line as shown in Figure 4.14(c, d, e). Computed using MATLAB, the time required to locate the falling edge from the original color images with resolution 1280×1024 and 640×480 were found to be 0.67s and 0.23s respectively.

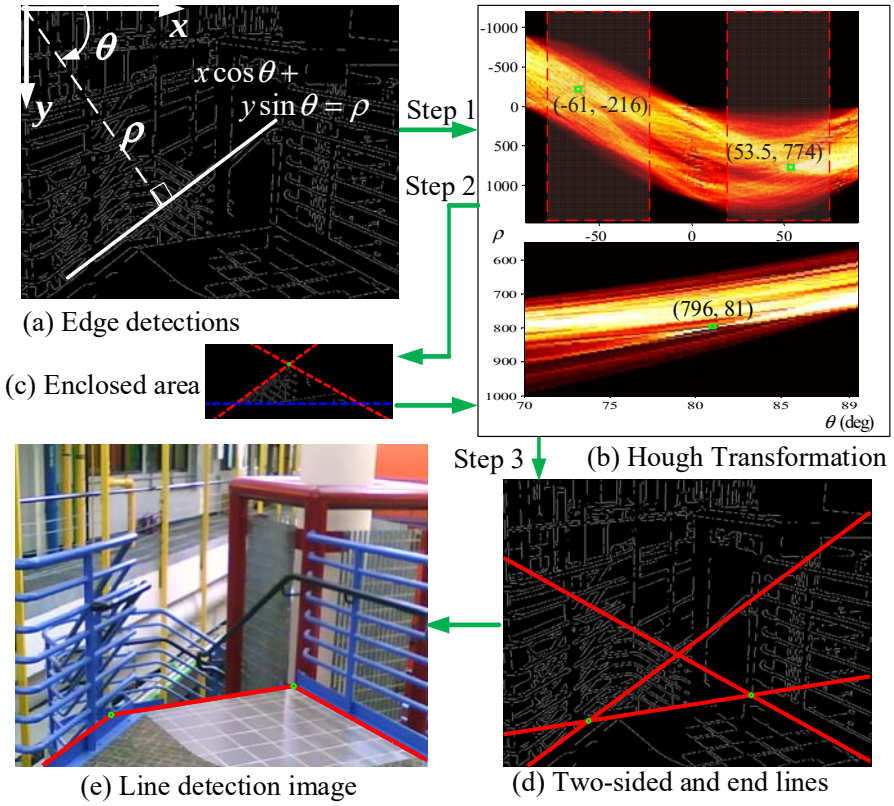

Figure 4.14 Procedures of the algorithm applied at the stairs

Figure 4.15 shows the procedure to detect the handrail using color segmentation to isolate the black-color followed by using MTS to detect the steel handrail. Five 20×20 pixels of the black-colored handrail are cropped from the RGB image for PCA-based color classification [63]. As shown in Figure 4.15(b), a bounding box (with its boundary set at

two standard deviations along the principal component's axes from the mean RGB values) characterizes the black-color for filtering other colors. Pixels in the bounding box are extracted and followed by connected-component labeling with the size threshold value (=2% pixel number of the image) to filter out small fragments; the results are superimposed in Figure 4.15(a). Figure 4.15(c) illustrates the experimentally measured MFD components and calculated Q as the user's hand (with the MTS attached) moves in the direction that Q increases to reach the handrail by simply.

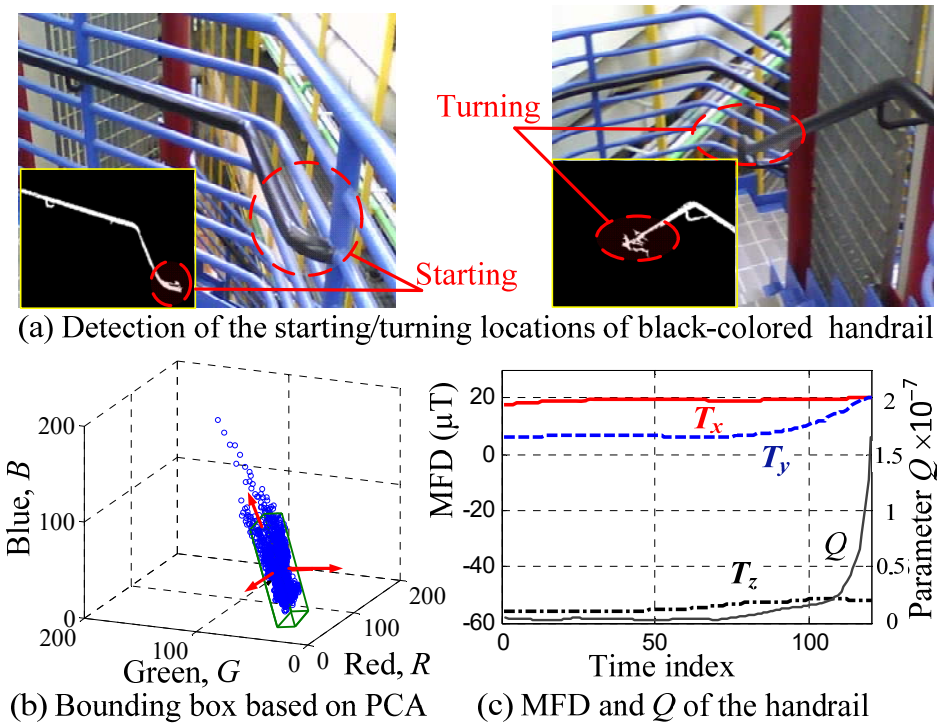

(a) Detection of the starting/turning locations of black-colored handrail

(b) Bounding box based on PCA

(c) MFD and Q of the handrail

Figure 4.15 Color-based object detection

4.4.3.2 Outdoor navigation

The MTS and its wayfinding algorithm can be integrated into a VIP white cane (Figure 4.16) and embedded in a personal mobile device to take advantages of the rapidly developing internet, GPS and digital imaging technologies to enhance the outdoor

navigation experience of a VIP. To avoid repetition, experimental results of two practical applications are discussed here: The first analyzes the magnetic anomalies due to commonly seen objects along a typical outdoor walkway (Figure 4.16), where the experimental results also serve as a basis for validating the observations in Figure 4.5. The second illustrates some dangerous waypoints in the context of street-crossing.

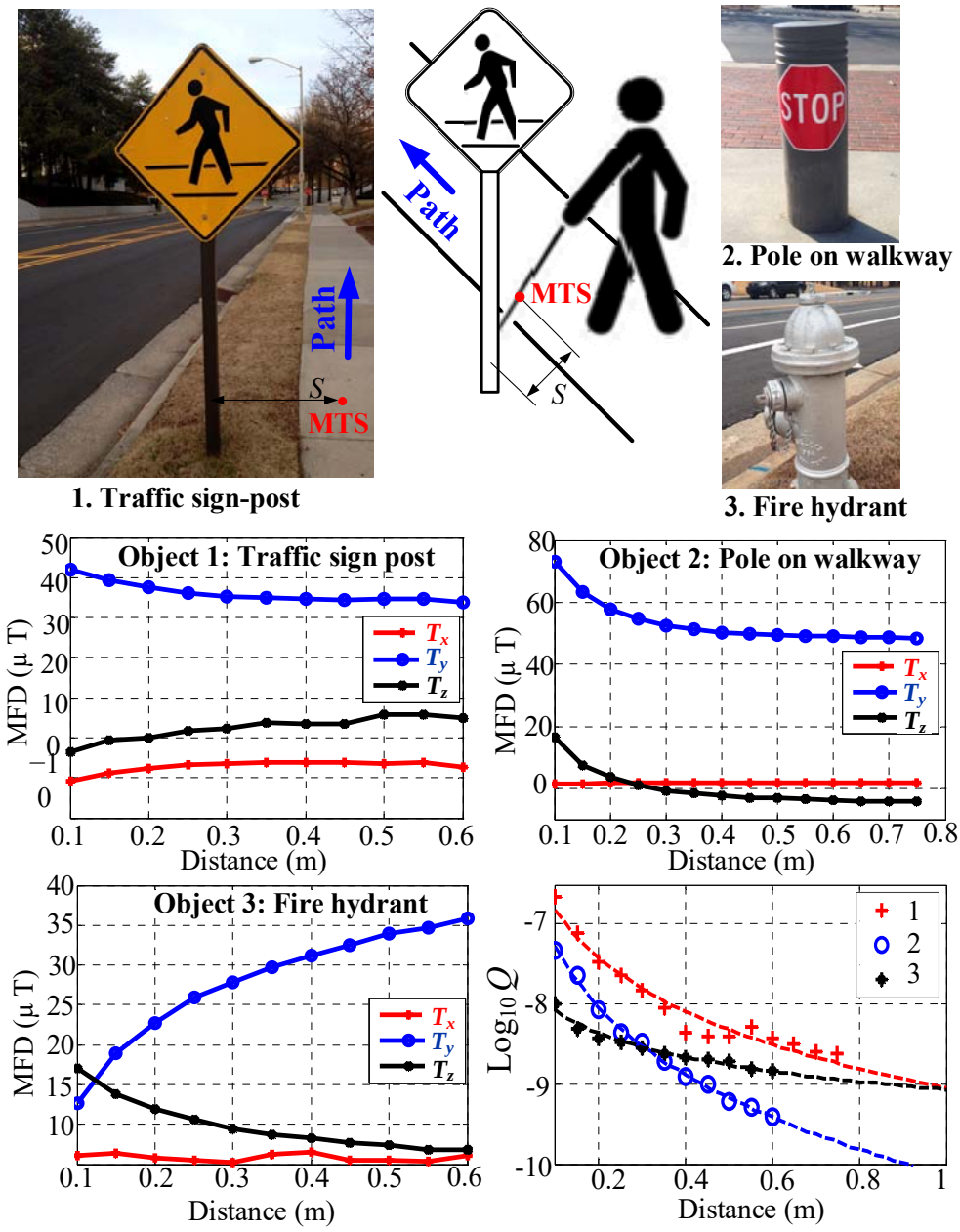

Figure 4.16 Measured **B** and Q of stationary objects

A. Experimental illustration of the parameter Q

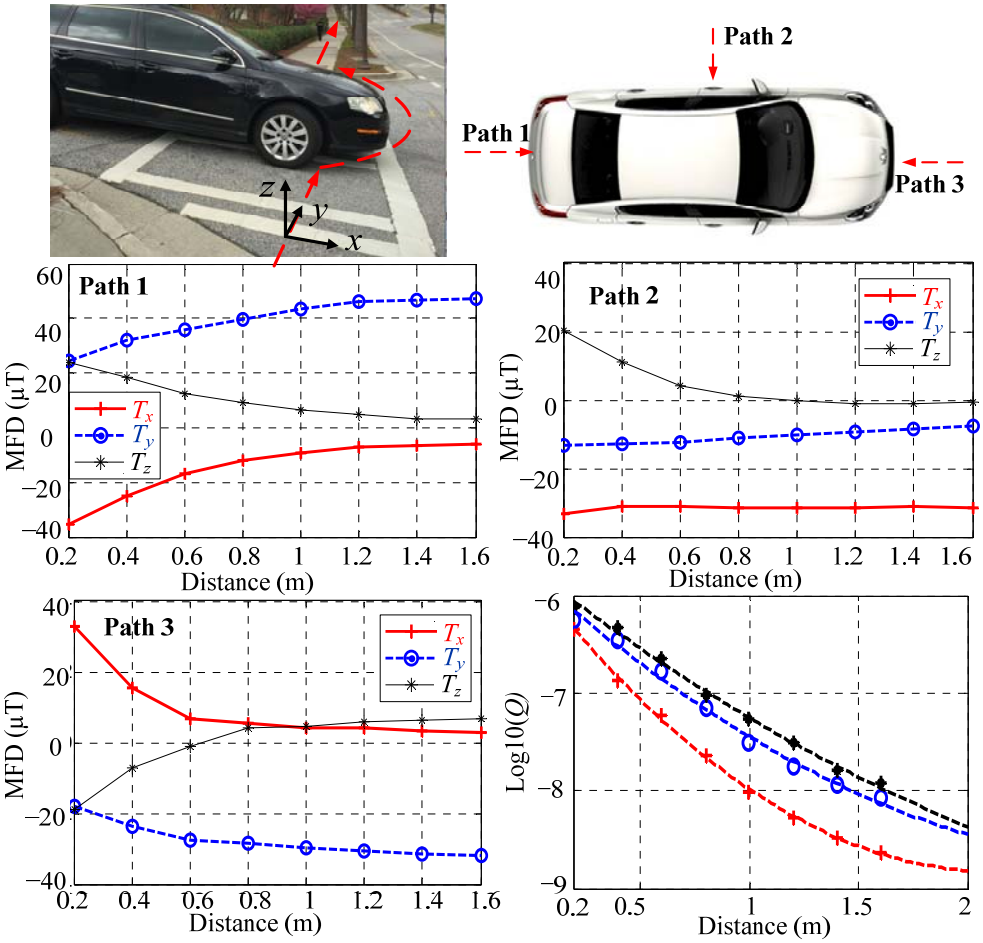

Figure 4.17 Vehicle avoidance

The observations in Figure 4.5 were validated experimentally using the MTS described in Figure 4.6(b, c) on three commonly seen outdoor objects (Objects 1, 2 and 3) and a vehicle; results are summarized in Figure 4.16 and Figure 4.17 respectively. In experiments for Figure 4.16, the MTS moved along a path (geographically from east to west) towards each obstacle. Figure 4.17 shows the MTS-measured data along the paths

around the vehicle (2008 VW Passat). Similar to Figure 4.5, Q approaches zero monotonically when the sensor is far from the object but each measured MFD approaches a constant corresponding to the path direction (relative to the geomagnetic field). Q increases drastically as the sensor moves near the object.

B. Technology-enhanced validation

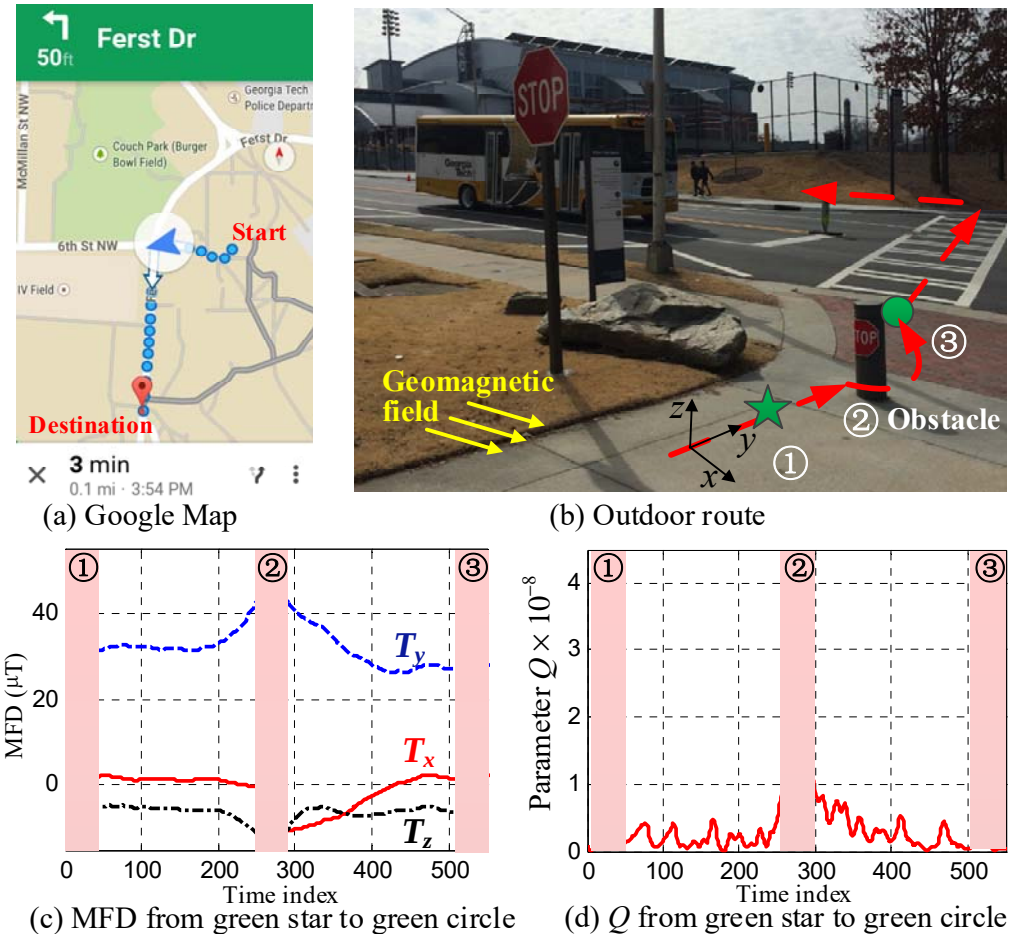

(a) Google Map (b) Outdoor route

(c) MFD from green star to green circle (d) Q from green star to green circle

Figure 4.18 Experimental results illustrating outdoor obstacle avoidance

GPS are widely available in personal devices for outdoor navigation but their resolutions (<10m) are inadequate to help VIPs avoid obstacles along the path; for examples, signposts and moving vehicles are not on the map. While these obstacles can be

avoided by healthy people, they cannot be seen by the VIPs. The MTS as an effective sensor for close-range navigation is best illustrated with a practical example which begins at location ① with a screen-captured Google map showing the specific route photographed in Figure 4.18(a, b). At ②, a commonly seen steel "stop" sign-pole (not on Google map) is on a pathway. The visually impaired user needs to avoid this obstacle before crossing the street at ③.

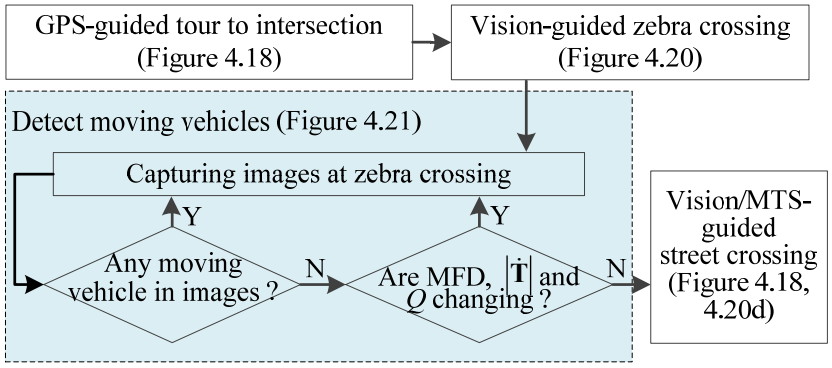

Figure 4.19 Flow chart illustrating the process of outdoor navigation

The flowchart (Figure 4.19) summarizes the sensing, computing and decision processes of the outdoor navigation system. As shown in Figure 4.19, the navigation system provides the (GPS, MTS and camera) information to the VIP to help derive decisions to overcome the following problems commonly encountered along the route:

– Avoids Stationary obstacles (Figure 4.18c),

– Locate/follow a zebra-crossing (Figure 4.20),

– Detect motion status of a vehicle (Figure 4.21)

1) Avoidance of stationary obstacles

As photographed in Figure 4.18(b), the VIP must avoid a steel "stop" sign-pole on the route. In this experiment, the sensor *y*-axis pointed in the moving direction (from east to west). The experimentally measured MFD components and calculated Q values along the path from ① (green star) to ③ (green circle) are plotted in Figure 4.18(c, d). Because the steel-pole obstacle ② distorts the geomagnetic field, its presence is detected by the blind user carrying an MTS which calculates the Q values in real time. As shown in Figure 4.18(d), the Q value increases dramatically as the people approach the obstacle signaling the user to go around to avoid the obstacle.

2) Locate/follow the zebra-crossing

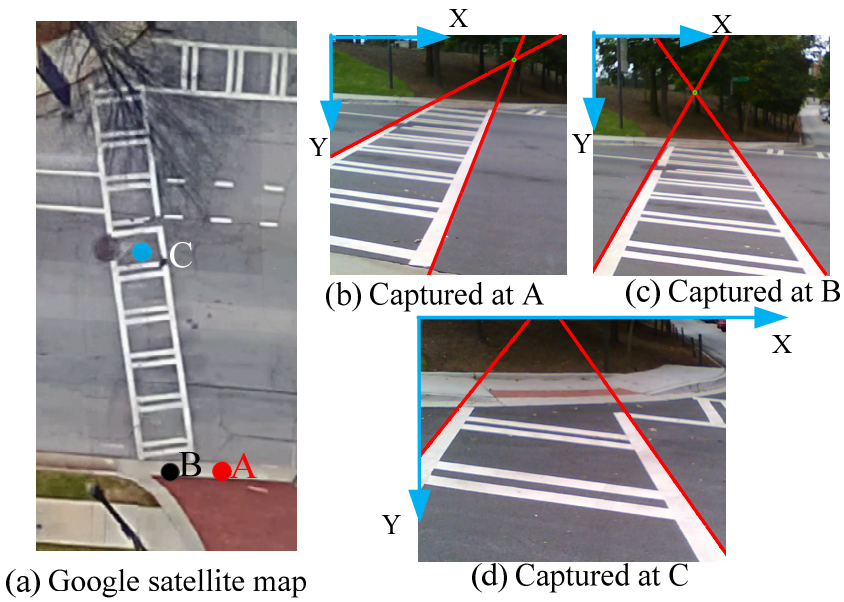

(a) Google satellite map (b) Captured at A (c) Captured at B (d) Captured at C

Figure 4.20 Zebra detection using vision image

Figure 4.20(a) shows a GPS bird-eye view of the zebra-crossing that is not perpendicular to the street. To help the VIP walk within the bounds, the wearable camera captured images as the person walks. Typical images captured at positions A, B and C are

shown in Figure 4.20(b, c, d) respectively. The two high-contrast straight (red) lines in each position image are detected using the HT method to mark the outlines of the zebra-crossing. The procedures for the HT are similar to that discussed in Figure 4.14 except both lines are searched in the region ($-75° \le \theta \le 75°$). The VIP's position relative to the zebra-crossing can be determined from their slopes: For the case in Figure 4.20, the two lines have negative slopes at A indicating the zebra-crossing is still on the left; once within the bounds at B or C, the two detected lines have opposite signs; and if the two slopes were positive, the person would have passed the zebra-crossing. The simple slope computation provides the basis for the image-based wayfinding at the zebra-crossing.

3) Detect motion status of the vehicle

Before crossing the street at position B (Figure 4.20a), the VIP must ensure that there are no moving vehicles from all sides of the street. An optical flow method which describes the pattern of apparent object motion between two consecutive images caused by the movement of objects is utilized to overcome the limited range of the MTS. In this paper, the iterative Lucas-Kanade method [64] with pyramids in OpenCV library is used for a sparse feature set. For local streets where vehicle speeds are no more than 40 mph, the optical flow method detects any moving vehicle within 15m of distance. Figure 4.21(a) illustrates typical optical flow results of the two images captured at position B, where the blue points mark the features; and the red lines display the motion trajectories.

As the vehicle approaches the zebra-crossing, the MTS detects the geomagnetic field distorted by the vehicle when it moves into the sensing range (a circle of approximately 2m radius). The detected changes in the distorted MFD or the time-

derivative of **T** can be utilized to determine the motion status of the vehicle. Figure 4.21(b) and Figure 4.21(c) compare the experimentally measured MFD (T_x, T_y, T_z) components, calculated Q values and time-derivative of **T** between **Status** 1 and **Status** 2 respectively, where **Status** 0 indicates no vehicle initially in the sensing range. Figure 4.21(b) shows the case of **Status** 1, where the vehicle slows down and stops. In Figure 4.21(c), the vehicle passes by the VIP without stopping; the VIP needs to wait until the motion **Status** equals to 0 or 1.

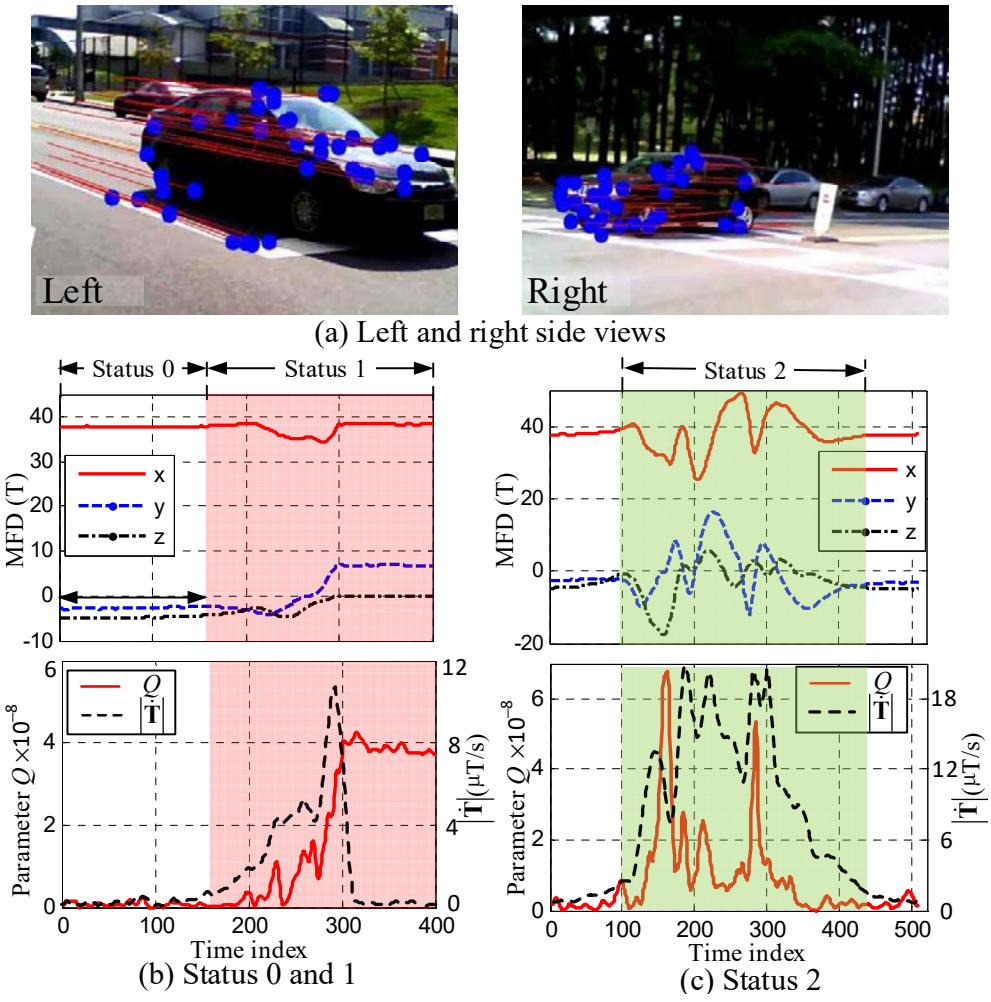

(a) Left and right side views

(b) Status 0 and 1

(c) Status 2

Figure 4.21 Vehicle detection

4.5 Summary

The creatively designed electromagnetic sensing system has been applied for the visually impaired assistance. A prototype of the gradient-based MTS system consisting of two orthogonal pairs of three-axis magnetic sensors has been developed for this application. The effectiveness and accuracy of the sensing system have been numerically and experimentally validated and evaluated.

A gradient-based method, along with an MTS, for the subtask arm reaching has been presented. By analyzing the characteristics of the magnetic tensor [**G**], the design concept, characteristics and operating range of MTS have been numerically illustrated. The effectiveness and accuracy of the sensing system have been numerically illustrated and experimentally validated with two different types of compact objects: a uniformly magnetized cylindrical PM and a ferrous wrench with a complex geometry. Numerical results illustrate that the theoretical errors in the estimated **M** and **R** are less than 1% when the ratio of the distance-to-object (largest dimension) is larger than 5 and 9. Using the prototype MTS, experiments on the cylindrical PM show that an accuracy with less than 2% errors can be achieved when the distance-to-radius ratio is between 6 and 10, and that the estimation errors increase as the generated magnetic field dramatically decreases with distance. It also offers some intuitive insights on the parameters P and γ for characterizing the location and orientation of an irregular magnetic object when the dipole model is a poor approximation. Experiments on the wrench confirm that the (P and γ) parameters offer an excellent alternative and/or supplement to traditional (**M**, **R**) for the visually impaired assistance where human plays a role.

A method utilizing geomagnetic field effects to guide the VIPs (way finding) has been presented. Along with the prototype MTS, a navigation system that combines the

advantages of the geomagnetic field effects commonly found in nature and the rapidly developing (internet, GPS, digital video imaging, and computing) technologies has been developed. Both numerical and experimental results show that the orientation-insensitive tensor-based parameter Q is a useful indicator to gauge the closeness of a magnetic object; and when simultaneously measuring the MFD and its time-rate, the MTS can be used to determine the motion status of the moving magnetic object (such as a vehicle) within a circular range of approximately 2m radius. As compared to GPS resolution of 10m, the MTS-enhanced navigation is capable of relatively accurate magmatic-map following (with a maximum mean position error of 0.21m and 0.08m standard deviation). Results also show that when coupled with information derived from images, magnetic information can significantly enhance the navigation performance of a VIP, especially for areas with large magnetic anomalies and/or potentially dangerous waypoints. The effectiveness of the MTS-enhanced method has been experimentally validated and illustrated with several practical applications; indoor magmatic-map following, obstacle avoidance and street-crossing at locations with no traffic lights.

CHAPTER 5. MANUFACTURING APPLICATIONS BASED ON ECD RECONSTRUCTION

5.1 Overview

To illustrate the potential capability of the combined the ECD field modeling/reconstruction and sensing system applied in manufacturing, two specific applications, conductivity estimation and defect localization/identification are presented, along with simulation and experiment results that validate and evaluate the accuracy and efficiency of the sensing system.

5.2 Feature Estimation Using ECD Field

For the manufacturing applications, the electromagnetic system is assumed to operate in magneto quasi-static (MQS) conditions: $2\pi L_o f \ll 1/\sqrt{\mu\varepsilon} \approx 3\times10^8$ where ε and μ are the permittivity and magnetic permeability of the conductor; f is the operating frequency, and L_o is the characteristic length of the system. The kernel functions η_{A2} and η_{B2} in (A.7b) and (A.8b) can be ignored. The conductor is assumed isotropic, free of deformation and no relative motion between the conductor and attached coil (no time derivative terms). Thereby, the state model (3.17) can be simplified as below:

$$\begin{bmatrix} [\mathbf{P}] & -\omega[\boldsymbol{\eta}_{A1}] \\ \omega[\boldsymbol{\eta}_{A1}] & [\mathbf{P}] \end{bmatrix} \begin{bmatrix} \mathbf{J}_{\mathrm{Re}} \\ \mathbf{J}_{\mathrm{Im}} \end{bmatrix} = \begin{bmatrix} \mathbf{0} \\ -\omega\mathbf{A}_s \end{bmatrix}$$

$$\widetilde{\mathbf{B}}_E = \begin{bmatrix} [\mathbf{U}_1] & \mathbf{0} \\ \mathbf{0} & [\mathbf{U}_1] \end{bmatrix} \begin{bmatrix} \mathbf{J}_{\mathrm{Re}} \\ \mathbf{J}_{\mathrm{Im}} \end{bmatrix} \qquad (5.1a, b)$$

Given the operating frequency and material properties, MQS assumption implies that the smallest dimension of the elements l should be smaller than the characteristic length of the system L_o, which is mathematically expressed as $l < L_o \ll 1/\left(2\pi f\sqrt{\mu\varepsilon}\right)$.

5.2.1 Conductivity Estimation

Many researches results have demonstrated that the conductivity measurements have the potential to explore the nondestructive evaluation of multiple material properties, such as subsurface residual stresses [67][68]. Two implementation methods for estimating the electrical conductivity based on ECD field reconstruction with the MFD measurements is illustrated.

A. Conductivity Estimation without Boundary Effect (Method 1)

For the applications where the boundary effects on the ECD field is neglected, the eddy current distribution ($\mathbf{J}_{\mathrm{Re}}$, $\mathbf{J}_{\mathrm{Im}}$) can be estimated using the solution to the inverse model (2.26a, b) with limited MFD measurements. Since the matrix [**P**] has diagonal structure, (5.2a, b) can be directly derived from (5.1a).

$$\sigma_i \upsilon_i \omega \mathbf{e}_i = \mathbf{j}_{i\mathrm{Re}},\ \sigma_i \upsilon_i \omega \mathbf{s}_i = -\mathbf{j}_{i\mathrm{Im}} \qquad (5.2a, b)$$

where i=1, 2, 3, …N_E, two 3×1 vectors $\mathbf{e}_i$ and $\mathbf{f}_i$ which are respectively constructed by the $(3i-2)^{\mathrm{th}}$, $(3i-1)^{\mathrm{th}}$ and $3i^{\mathrm{th}}$ elements of the vector $(\left[\boldsymbol{\eta}_{\mathrm{Al}}\right]\mathbf{J}_{\mathrm{Im}})$ and $(\left[\boldsymbol{\eta}_{\mathrm{Al}}\right]\mathbf{J}_{\mathrm{Re}} + \mathbf{A}_S)$ can be estimated given the external source, conductor shape and the MFD measurements.

Applying (5.2a, b) for all N_E elements and expressing the results in the matrix form lead to

$$[\mathbf{E}]\boldsymbol{\sigma}=\mathbf{J}_{\mathrm{Re}},[\mathbf{S}]\boldsymbol{\sigma}=-\mathbf{J}_{\mathrm{Im}} \tag{5.3a, b}$$

where $\boldsymbol{\sigma}\left(\in \mathbb{R}^{N_E\times 1}\right)=\begin{bmatrix}\sigma_1 & \sigma_2 & \cdots & \sigma_{N_E}\end{bmatrix}^{\mathrm{T}}$; $[\mathbf{E}]\left(\in \mathbb{R}^{3N_E\times N_E}\right)=\omega\begin{bmatrix}\upsilon_1\mathbf{e}_1 & \mathbf{0} & & \mathbf{0}\\ \mathbf{0} & \upsilon_2\mathbf{e}_2 & \ddots & \mathbf{0}\\ \mathbf{0} & \mathbf{0} & & \upsilon_{N_E}\mathbf{e}_{N_E}\end{bmatrix}^{\mathrm{T}}$,

$[\mathbf{S}]\left(\in \mathbb{R}^{3N_E\times N_E}\right)=\omega\begin{bmatrix}\upsilon_1\mathbf{s}_1 & \mathbf{0} & & \mathbf{0}\\ \mathbf{0} & \upsilon_2\mathbf{s}_2 & \ddots & \mathbf{0}\\ \mathbf{0} & \mathbf{0} & & \upsilon_{N_E}\mathbf{s}_{N_E}\end{bmatrix}^{\mathrm{T}}$.

Combining (5.1b) and (5.3a, b), the relationship between the MFD measurements and electrical conductivity distribution can be established in (5.4) where $\boldsymbol{\eta}_2$ accounts for the errors in the measured $\widetilde{\mathbf{B}}_E$.

$$\widetilde{\mathbf{B}}_E=[\mathbf{K}]\boldsymbol{\sigma}+\boldsymbol{\eta}_2 \tag{5.4}$$

where $[\mathbf{K}]\left(\in \mathbb{R}^{6N_M\times N_E}\right)=\begin{bmatrix}[\mathbf{U}_1][\mathbf{E}] & \mathbf{0}\\ \mathbf{0} & -[\mathbf{U}_1][\mathbf{S}]\end{bmatrix}$

To handle the high matrix condition of the matrix [**K**] which indicates the sensitivity of the computed solution to the measurement noise, the regularization method is used to calculate the conductivity $\boldsymbol{\sigma}$ as shown in (5.5) with the regularization parameter α derived using the L-Curve graphical method.

$$\boldsymbol{\sigma}_\alpha=\left([\mathbf{K}]^{\mathrm{T}}[\mathbf{K}]+\alpha[\mathbf{I}]\right)^{-1}[\mathbf{K}]^{\mathrm{T}}\widetilde{\mathbf{B}}_E \tag{5.5}$$

B. Conductivity Estimation with Boundary Effect (Method 2)

The boundary effects can tremendously affect the distribution of the eddy current and consequently the conductivity estimation. Because the model of ECD estimation is based on non-linear regularization when considering the boundary effects, it is almost impossible to get a mathematical model for electrical conductivity estimation directly from (5.1a, b). Thereby, the measurement vector $\mathbf{B}_E$ that is a nonlinear function of the N_E elemental conductivities, $\mathbf{B}_E\left(\sigma_1,\cdots,\sigma_{N_E}\right)$. Linearized about the mean operating point $\left(\bar{\sigma},\overline{\mathbf{B}}_E\right)$, the reconstruction of the conductivity distribution is formulated in (5.6) where $\boldsymbol{\eta}_3$ accounts for the errors in the measured deviation $\hat{\mathbf{B}}_E$:

$$\hat{\mathbf{B}}_E=[\mathbf{W}]\hat{\boldsymbol{\sigma}}+\boldsymbol{\eta}_3 \tag{5.6}$$

where $[\mathbf{W}]=\left[\begin{array}{cccc}\frac{\partial \mathbf{B}_E}{\partial \sigma_1} & \frac{\partial \mathbf{B}_E}{\partial \sigma_2} & \cdots & \frac{\partial \mathbf{B}_E}{\partial \sigma_{N_E}}\end{array}\right]$ is the Jacobian matrix; and the conductivity deviation $\hat{\boldsymbol{\sigma}}=\left[\hat{\sigma}_1\cdots \quad \hat{\sigma}_i \quad \cdots\hat{\sigma}_{N_E}\right]^{\mathrm{T}}$. The column vector $\partial\mathbf{B}_E/\partial\sigma_i$ is given by

$$\frac{\partial \mathbf{B}_E}{\partial \sigma_i}=\left(\tilde{\mathbf{B}}_{Ei}-\overline{\mathbf{B}}_E\right)\Big/\Delta\sigma \tag{5.7}$$

where $\tilde{\mathbf{B}}_{Ei}$ represents the MFD measurements of all the sensors assuming a plate with constant conductivity $\bar{\sigma}$ except the i^{th} element with conductivity $\bar{\sigma}+\Delta\sigma$. $\overline{\mathbf{B}}_E$ corresponds to the measurements for the same metallic plate with constant conductivity $\bar{\sigma}$. Given the external source and conductor, [**W**] can be pre-calculated using (5.1a, b) given the external source, conductor shape and the operating point. Similarly, the conductivity can be estimated using regularization method from (5.6).

5.2.2 Defect Localization and Identification

The presence of any cavity inside the non-magnetic conductor can significantly influence the eddy current distribution generated by external sources as illustrated in Figure 5.1 where a small slot inside the conductive plane is an example cavity and an electromagnet (EM) is the external source for creating the induced eddy current. The eddy current represented using red dash curves has an irregular closed loop instead of a perfect circle which is the eddy-current loop for the case without any defect. Thereby, the eddy current can indicate the shape and location of the cavity.

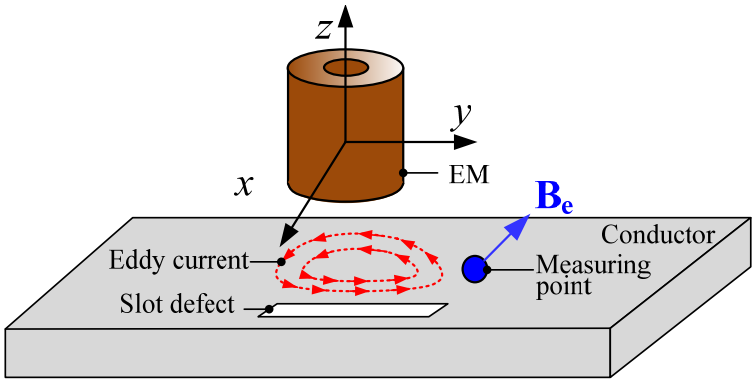

Figure 5.1 Schematics of cavity defect localization and identification

The existence of the cavity, within which no eddy current is generated, can be interpreted as the absence of the elements at the corresponding position. The MFD generated by the eddy current can be considered as the sum of the effects of all the conductor elements. Thereby, for this application where the external source inducing the ECD in the metallic plate (with known exterior geometry) is known, the reconstruction of the interior geometry is formulated in (5.8) where $\boldsymbol{\eta}_4$ accounts for the errors in the data $\hat{\mathbf{B}}_E \left(= \tilde{\mathbf{B}}_E - \overline{\mathbf{B}}_E\right)$ and $\overline{\mathbf{B}}_E$ corresponds to data for the same metallic plate but homogenous with constant conductivity:

$$\hat{\mathbf{B}}_E = [\mathbf{Q}]\mathbf{V} + \boldsymbol{\eta}_4 \tag{5.8}$$

where $[\mathbf{Q}]=\begin{bmatrix}\mathbf{q}_1 & \mathbf{q}_2 \cdots & \mathbf{q}_i \cdots & \mathbf{q}_{N_E}\end{bmatrix}$ is the sensitivity matrix with its column vector $\mathbf{q}_i$ in $[\mathbf{Q}](\in \mathbb{R}^{6N_M \times N_E})$ given by (5.9) where $\breve{\mathbf{B}}_{Ei}$ is the MFD measurements of all the sensors assuming a homogeneous plate (with constant conductivity) except the i^{th} element:

$$\mathbf{q}_i \left(\in \mathbb{R}^{6N_M \times 1}\right) = \breve{\mathbf{B}}_{Ei} - \overline{\mathbf{B}}_{E0} \tag{5.9}$$

The sensitivity matrix [**Q**] can be pre-calculated using (5.1a, b) given for the external source and conductor. In (5.8), the existent probability $\mathbf{V}(\in \mathbb{R}^{N_E \times 1})$ characterizes the interior geometry of the conductor. Each element in **V** has a value between 0 (conductive) and 1 (non-conductive).

With (5.8) and pre-calculated [**Q**], the distribution of the defects represented by **V** can be estimated using the Regularization methods expressed by (5.10).

$$\mathbf{V}_\alpha = \left([\mathbf{Q}]^{\mathrm{T}}[\mathbf{Q}] + \alpha[\mathbf{I}]\right)^{-1}[\mathbf{Q}]^{\mathrm{T}}\hat{\mathbf{B}}_E \tag{5.10}$$

where α with the range of [0, 1] is the regularization parameter to be determined. With the estimated **V** representing the existence probability of cavity defects in all N_E element, the locations and shapes of the cavity defects can be estimated.

5.3 Simulation Results and Discussion

The ECD field reconstruction and the extended applications (cavity defect localization/identification and conductivity estimation) have been numerically investigated

in this section. An EM with schematics illustrated in Figure 5.2(a) is placed above the conductive plate with its axis perpendicular to a conductive plate made of aluminum. The detail parameters are represented in Table 5.1. I_o and N represent the amplitude of the excitation current and number of turns respectively. The top surface of the plate is located at the plane z_C = 5.5mm whereas the MFD generated by the eddy current is collected on the plane z_S = 7mm.

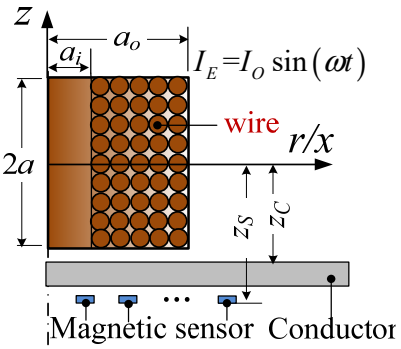

(a) The schematic of EM

Table 5.1 Parameters of the coil

a_i	3.75mm	I_o	1A
a_o	6.5mm	N	60 #
a	2mm	z_C	5.5mm

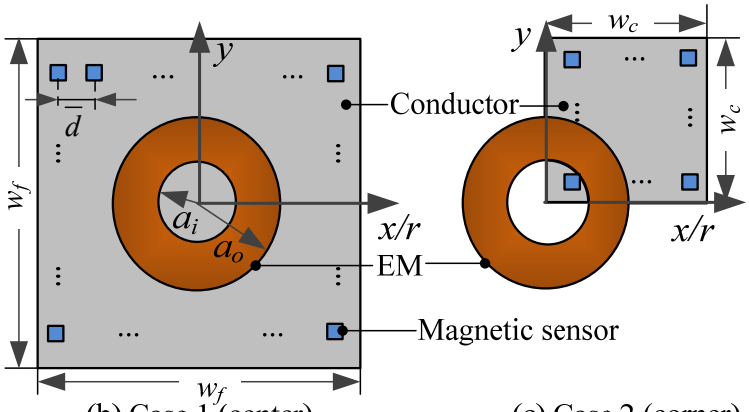

(b) Case 1 (center) (c) Case 2 (corner)

Figure 5.2 Two cases for simulations

In the simulations, two types scenarios are considered as shown in Figure 5.2(b) and (c), where the EM is placed at the center and corner of the conductive plate made of aluminum respectively with the sensor interval $\bar{d}$.

5.3.1 ECD Field Reconstruction and Tracking

In this section, simulation results are presented to demonstrate the accuracy and efficiency of the ECD field reconstruction involving forward and inverse models along with numerical analysis for the localization of the eddy-current center.

5.3.1.1 ECD and MFD estimation (Forward Model)

The ECD field reconstruction and its extended applications are based on the forward model, which makes it essential to evaluate and validate it.

A. Case 1 (center)

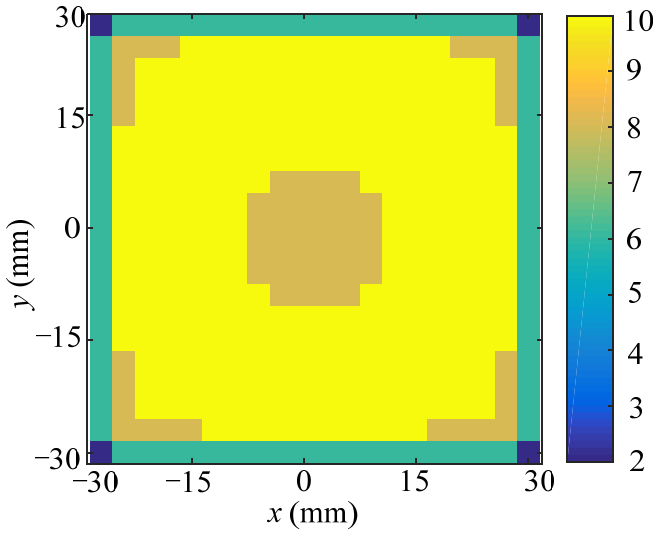

Figure 5.3 The initial and final mesh for Case 1

For the case with the EM placed at the center as shown in Figure 5.2(b), the estimated ECD and MFD (generated by the eddy current) are compared with the analytical solution provided in [65][66]. To analyze to the skin effect of the eddy current, two cases with different excitation frequency (1kHz and 10kHz) are presented and the element

refinement is only performed in the axial direction. The parameters of the ECD and MFD field estimation for both 1kHz and 10kHz cases are presented in Table 5.2.

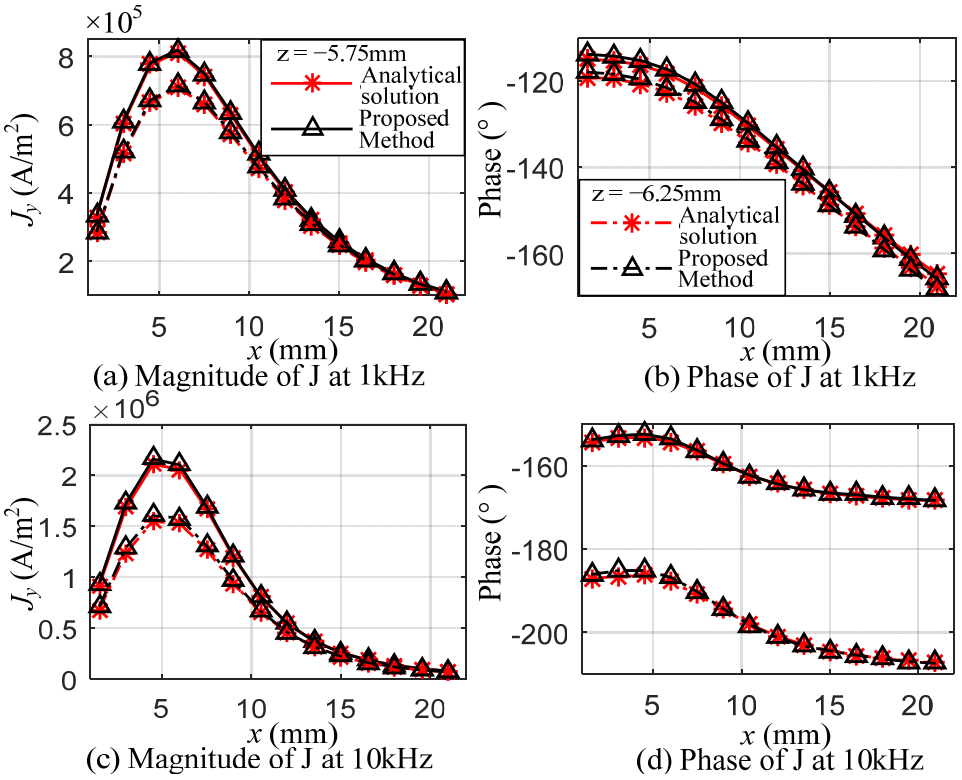

Figure 5.4 Eddy current density distribution

The initial element division is good for the low-frequency case whereas the elements need to be refined for the high-frequency case which is illustrated in Figure 5.3.

Table 5.2 The parameters of the field estimation for Case 1

Initial element size	1.5×1.5×0.5(mm)	Q_M	4
Conductor size	60×60×1(mm)	g	30%
Element number	1600	k	0.1

The simulated results for ECD and MFD are compared with analytical solution. Figure 5.4 represents the magnitude and phase distribution of ECD J_y (y component) for the low- and high-frequency cases along the x axis with z = −5.75mm, −6.25mm. The

magnitude and phase distribution of the MFD (z component) along the x axis with z =−4.5mm for low and high-frequency cases are plotted in Figure 5.5.

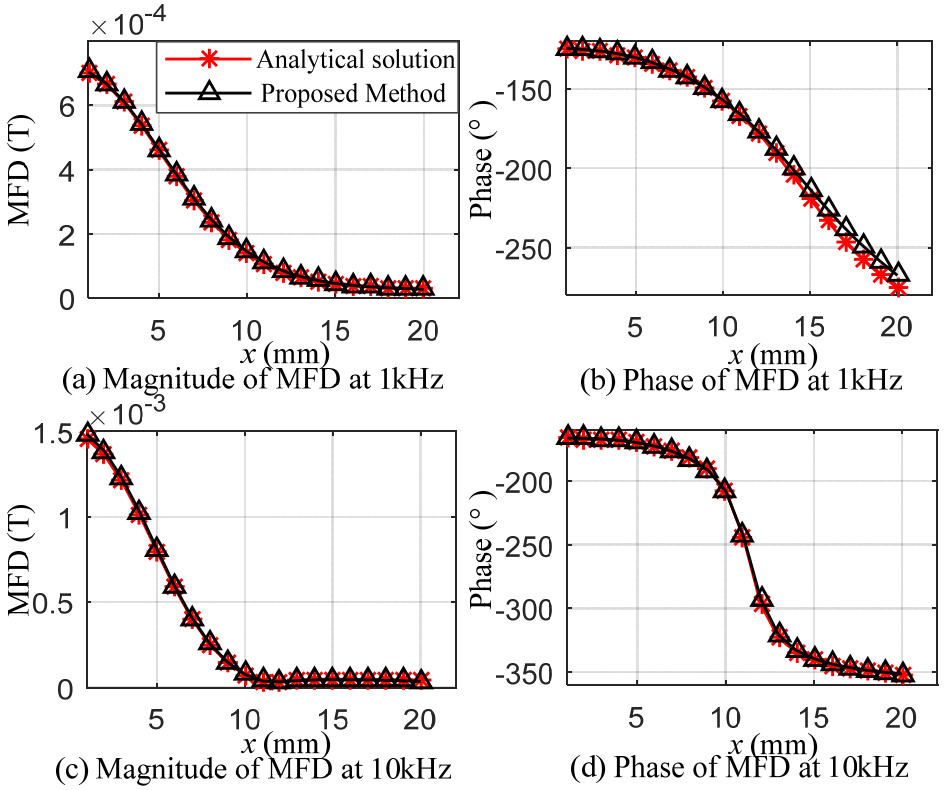

Figure 5.5 The distribution of MFD in z direction

B. Case 2 (corner)

The proposed method has the ability to estimate the ECD distribution generated in the conductors with boundary effects as illustrated in Figure 5.2(c). The parameters of the estimation are listed in Table 5.3. The excitation current frequency is set to 1kHz. The phenomenon of the skin effect is not obvious due to the relatively low current frequency (1 kHz). The conductor boundary has the dominant effects on the ECD distribution and the adaptive element refinement is only applied in x-y plane for simplicity as shown in Figure 5.6. The real and imaginary part of the ECD collected on plane z = −6mm are compared

with FEM (COMSOL) results as shown in Figure 5.7, where the subplots (a) and (c) represent ECD field distribution using arrows whereas (b) and (d) provide ECD distribution of the real and imaginary part for J_y along the diagonal starting from origin.

Table 5.3 The parameters of the field estimation for Case 2

Initial element size	2.5×2.5×1(mm)	Q_M	4
Conductor size	20×20×1(mm)	g	30%
Initial Element number	64	k	0.1

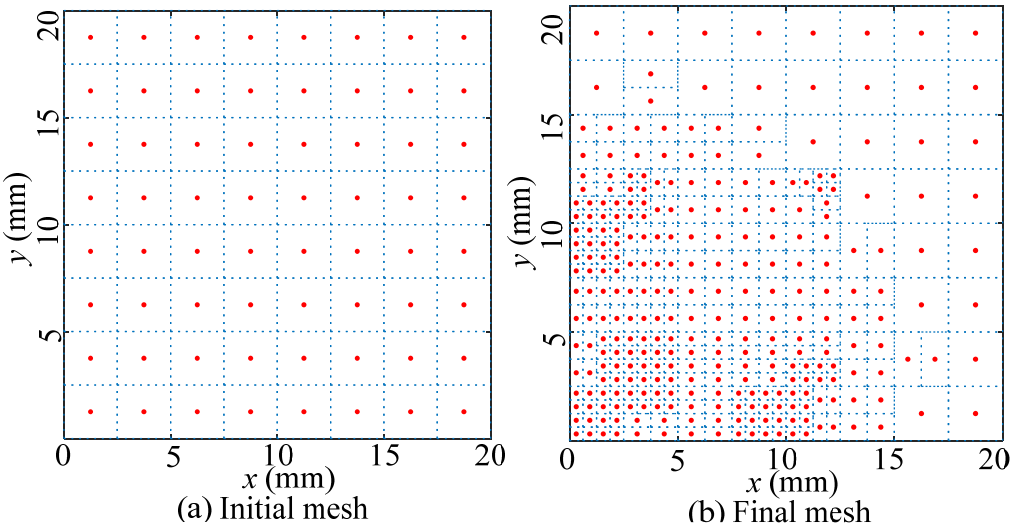

Figure 5.6 The initial and final mesh for Case 2

Some observations can be drawn from the simulation results of both cases:

- As illustrated in Figure 5.4 and Figure 5.5, the proposed forward models accurately estimate the eddy-current and generated magnetic fields.
- The differences of the eddy current in the two layers increase with frequency, which is phenomenon the skin effect and justifies the adaptive element refinement.

– As illustrated in Figure 5.7, the ECD field can be estimated using additional boundary constraints. Meanwhile, the estimation results of the imaginary part are more accurate than that of the real part.

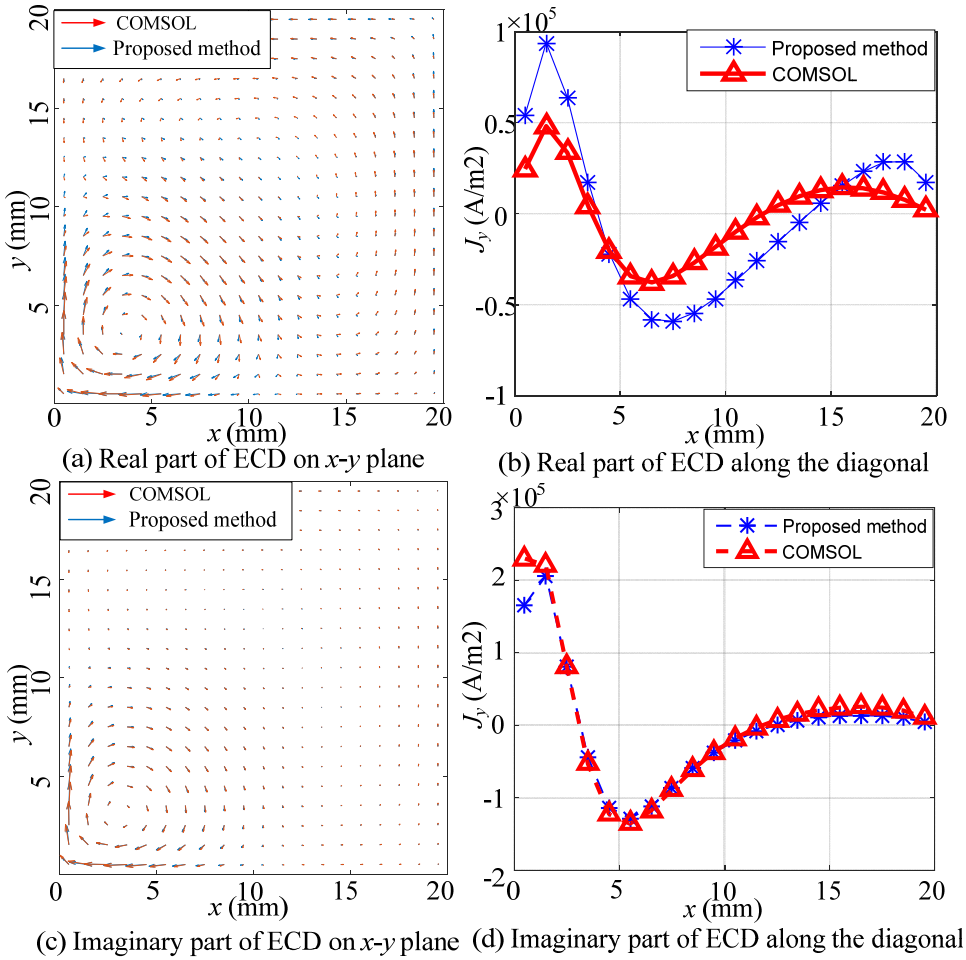

(a) Real part of ECD on *x*-*y* plane (b) Real part of ECD along the diagonal

(c) Imaginary part of ECD on *x*-*y* plane (d) Imaginary part of ECD along the diagonal

Figure 5.7 The distribution of eddy current

5.3.1.2 ECD Reconstruction Using MFD Measurements (Inverse Model)

As theoretically expressed in the last section, the ECD field inside the conductor can be estimated using MFD measurement indirectly. In this subsection, several simulation

results are presented to numerically demonstrate the accuracy and efficiency of the ECD field reconstruction method.

Two types scenarios for ECD field reconstruction was considered as shown in Figure 5.2 (b) and (c) with the current frequency equal to 1 kHz. The phenomenon of the skin effect is not obvious due to the relatively low current frequency (1 kHz), for simplicity, the adaptive element refinement was only applied in *x*-*y* plane. More reconstruction parameters are expressed in Table 5.4. The initial and final mesh are shown in Figure 5.8 for both cases.

The MFD used for ECD reconstruction is calculated with the analytical solution in [65][66] and COMSOL for Case 1 and Case2 respectively. The initial estimations for both cases are represented in Figure 5.8(a) and (b) whereas the final estimations with and without constraints are compared with the simulated eddy current as shown in Figure 5.9 (a) and (b), which represent the ECD distribution of the real and imaginary part for J_y along the *x* axis (Case 1) and the diagonal starting from origin (Case 2) represented using blue dash line shown in Figure 5.8(c) and (d). Three iterations were conducted and the estimation errors during the iteration are expressed in Figure 5.9(c) and (d) for both cases.

Table 5.4 Reconstruction parameters for two cases

	Center	**Corner**
Measurement Location	$z = -7$mm, $x, y = (-28{:}4{:}28)$ mm	$z=-7$mm, $x, y = (0{:}2.5{:}30)$ mm
Measurement Number	225	100
Conductor Size	60×60×1(mm)	30×30×1(mm)
Initial Element Size	6×6×1(mm)	3.75×3.75×1(mm)
k	0.1	0.1
Q_M	4	4
g	30%	30%

As an ill-posed inverse problem, the measurement number and distribution have critical effects on the ECD field reconstruction. Using the average diameter $\overline{a}=\left(a_i+a_o\right)/2$ as the characteristic dimension of the coil, simulations for Case 1 (no constraint) with different ratio of the spacing interval of the magnetic sensor $\overline{d}$ array and $\overline{a}$ represented in Table 5.5 were performed. The real and imaginary part of J_y along the x axis were collected and the average error, standard deviation (SD) and regularization parameter α are plotted in Figure 5.10.

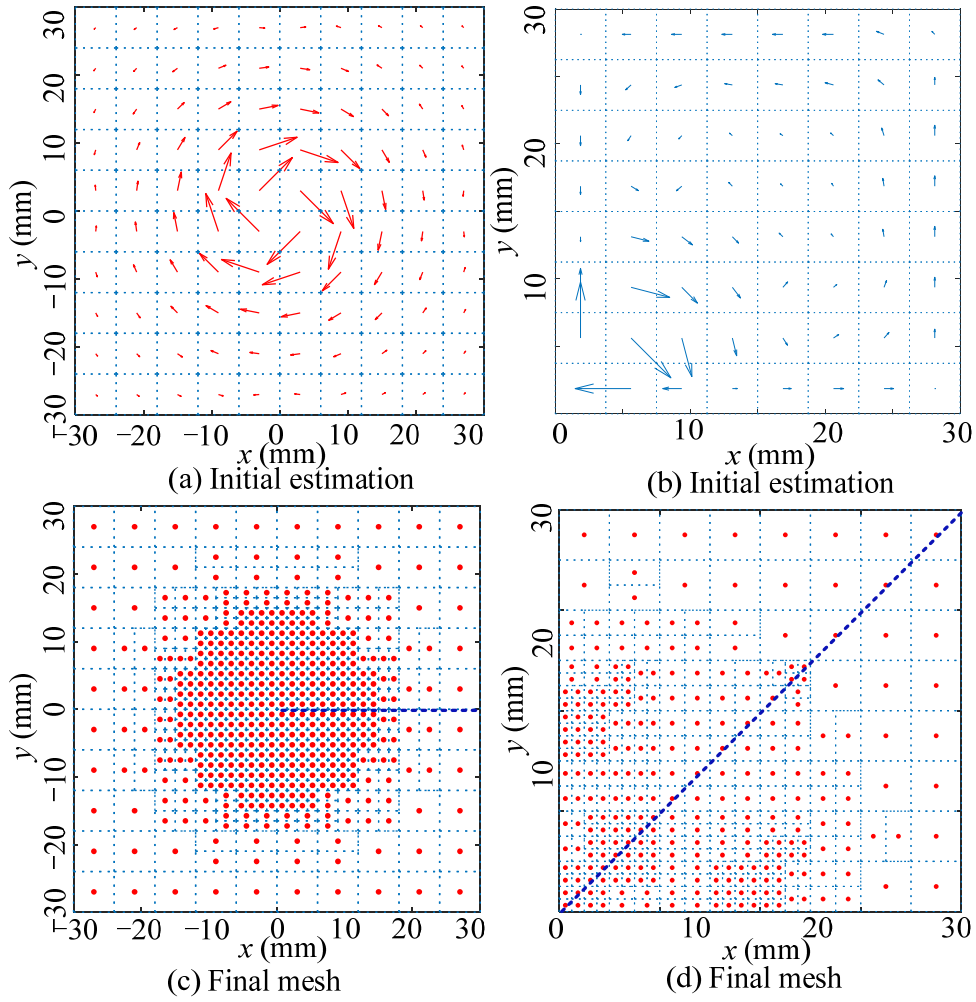

Figure 5.8 Element refinement for two cases

Meanwhile, to examine the robustness of the reconstruction method, reconstruction simulations with additional Gaussian white noise (with SNR 20dB, 10dB, 5dB, 2dB) were conducted using Case 1. Similar to Figure 5.9, the real and imaginary part of J_y along the x axis were collected and the average error and standard deviation (SD) are plotted in Figure 5.11(a) and (b). The regularization parameter α and p are represented in Figure 5.11 (c) and (d) respectively for the reconstruction of the real and imaginary components.

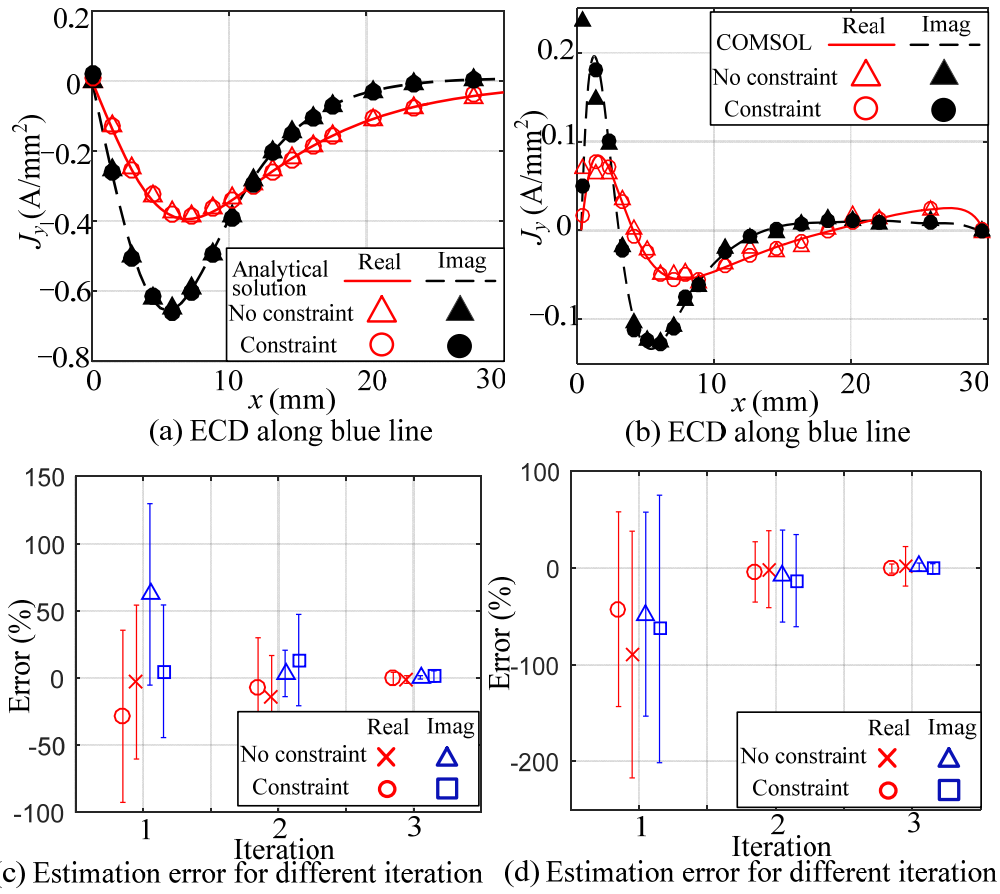

Figure 5.9 ECD field reconstruction results without noise

One important objective of ECD reconstruction is to track the path of eddy current. By reconstructing the ECD field generated by the coil which moves to five locations on x-y plane above the conductor [(0, 0), (4, 4), (−4, −4), (−4, 0), (0, −4)], the center of ECD

field (x_0, y_0) is estimated. The first three configurations of sensor arrays shown in Table III were selected and the simulated measurements used for field reconstruction with physical constraints were added with additional Gaussian white noise (SNR: 20dB). The error of ECD track is manifested in Table 5.6.

Table 5.5 Five configurations of sensor arrays

	1	**2**	**3**	**4**	**5**
$\bar{d}$ (mm)	4	6	10	12	15
Ratio $\bar{d}/\bar{a}$	0.78	1.17	1.95	2.34	2.93
Location x, y (mm)	−28:4:28	−27:6:27	−25:10:25	−30:12:30	−30:12:30
Number	225	100	36	25	16

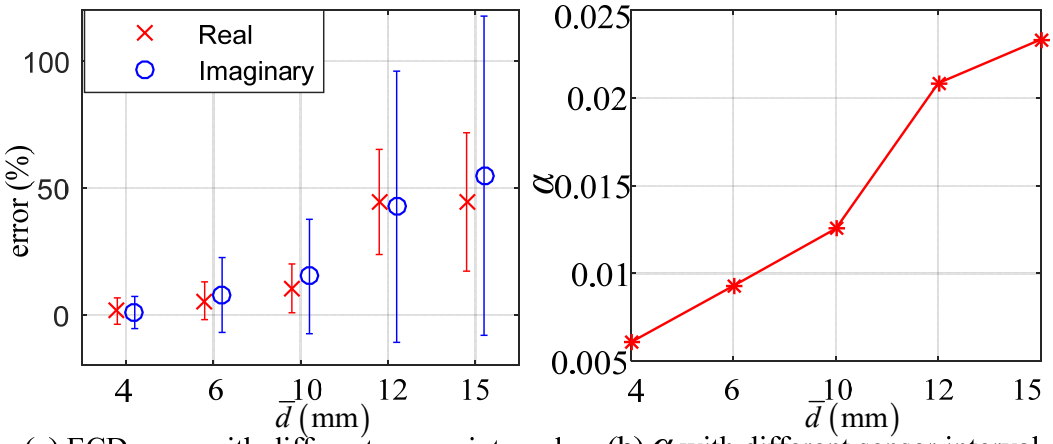

(a) ECD error with different sensor interval (b) α with different sensor interval

Figure 5.10 Reconstruction error and α with different $\bar{d}$

Table 5.6 Eddy-current track error (x, y, nm)

$\bar{d}/\bar{a}$	**(0, 0)**	**(4, 4)**	**(−4, −4)**	**(−4, 4)**	**(4, −4)**
0.78	(27, 5)	(−4, 9)	(−16, 11)	(4, 1)	(−13, −7)
1.17	(20, 1)	(35, 43)	(65, 51)	(50, 42)	(49, 53)
1.95	(19, 1)	(33,24)	(58,38)	(17, 44)	(18, 48)

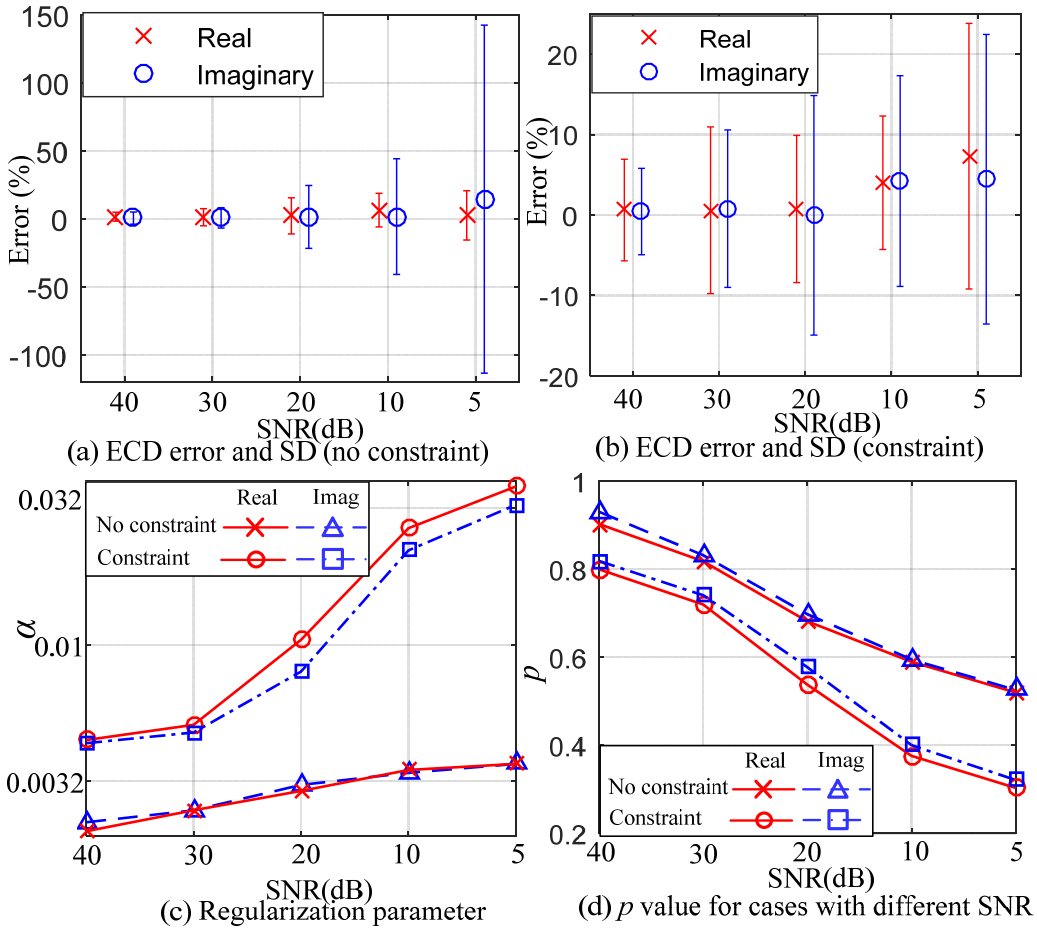

Figure 5.11 Reconstruction error, α and p with different SNR

Some observations can be drawn from the simulation results of both cases:

- As illustrated in Figure 5.9, even though this is an ill-condition problem, , the proposed ECD reconstruction method based on the regularization method can reconstruct the ECD field for both cases accurately.
- With the increase number of the iteration for the element refinement, the reconstruction error decreases dramatically as illustrated in Figure 5.9(c) and (d).
- With the increase of the ratio $\overline{d}/\overline{a}$, the reconstruction error increases as shown in Figure 5.10. The error is unacceptable when the ratio approaches 2. The required spacing

interval of the sensor array is mainly determined by the shape of the eddy current or the dimension of the excitation coil.

- As shown in Figure 5.10 and Figure 5.11, the regularization parameter α increases with the increase of the sensor interval and the decrease of SNR of the MFD data. More noise in the MFD measurements and larger sensor interval need more regularization (or larger α). Meanwhile, the reconstruction cases with additional constraints need higher regularization than those without constraints
- With the same MFD measurements (same SNR), the reconstruction results with physical constraints are much better than that without constraints. Additional physical constraints have the ability to suppress the effects of the measurement noise and the cases with larger α provide more regularization to filter the noise in the measurements.
- As shown in Table 5.6, the ECD reconstruction can track the eddy current with the average error around 10μm for ratio $\overline{d}/\overline{a} = 0.78$, which increases as the ratio $\overline{d}/\overline{a}$ increases.

5.3.2 Conductivity Estimation

As theoretically presented in the last subsection, the electrical conductivity of the conductor can be estimated using MFD measurements for the scenarios with and without the effects of the physical boundary. Several simulations have been performed to demonstrate the accuracy and efficiency of the method of electrical conductivity estimation. Two types of scenarios were considered in the simulation as shown in Figure 5.2(b) and (c). With low excitation frequency (200Hz) and thin conductor thickness (1mm), the phenomenon of the skin effect is not obvious. The estimated results for both cases are

compared with the pre-set electrical conductivity. The distribution of the electrical conductivity is assumed to be continuous.

A. Case 1 (without boundary)

To avoid the boundary effects, an EM is placed at the center of a conductive plate with the cylindrical axis perpendicular to the plate (size: 120×120×1, unit: mm) as illustrated in Figure 5.2(b). The MFD measurements were provided by COMSOL. To eliminate the boundary effects and decrease the calculation, the MFD data array generated by the eddy current covers the size of area 60×60(mm). Only the conductivity of the part of the conductor (60×60 unit: mm) directly under the MFD data array was estimated.

Table 5.7 Conductivity estimation parameters for Case 1

The location of MFD measurements		z = 7mm, x, y = (−28:4:28) mm	
Conductor size	60×60×1(mm)	**Measurement number**	225
Initial element size	6×6×1(mm)	k	0.1
Q_M	4	g	30%

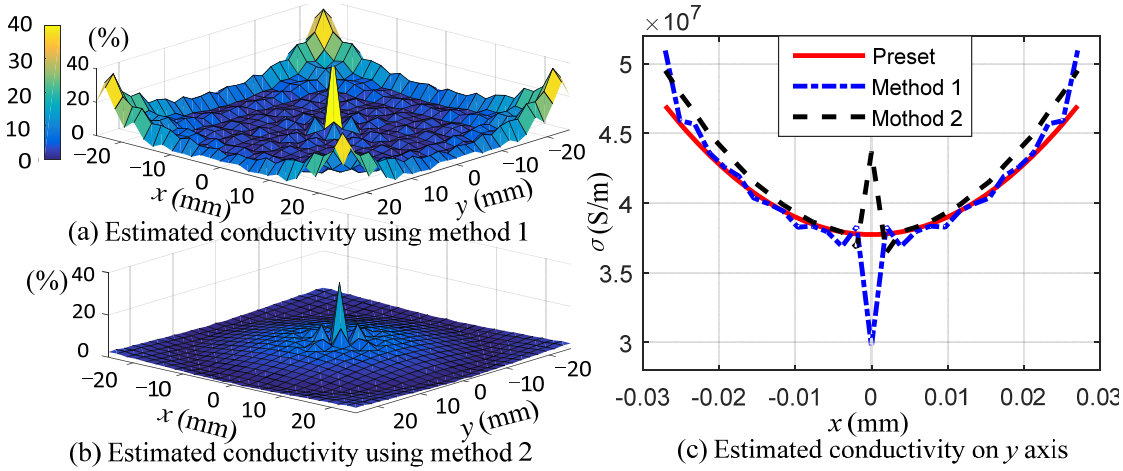

(a) Estimated conductivity using method 1

(b) Estimated conductivity using method 2

(c) Estimated conductivity on y axis

Figure 5.12 Conductivity estimation of large variation case

The details of the parameters of the conductivity estimation using Method 1 based on the ECD field reconstruction are presented in Table 5.7. The same sensor configuration

shown in Table 5.7 is utilized for the derivative method (Method 2). However, the conductor is evenly divided into small elements with the size of 2×2×1(mm).

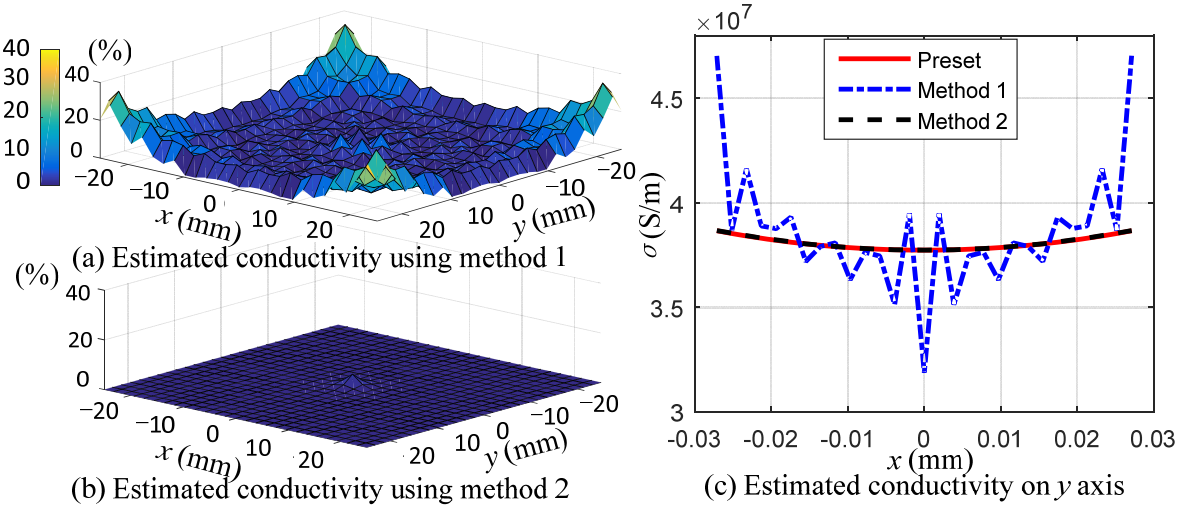

Figure 5.13 Conductivity estimation of small variation case

For validating the conductivity estimation method, the conductivity distribution of the plate is assumed to have the form:

$$\sigma(x,y)=\sigma_0\left[1+q_o\left(x^2+y^2\right)/0.03^2\right] \tag{5.11}$$

where σ_0 (= 3.774×10^7S/m) is the conductivity of aluminum, q_o is a constant which determines the variation of the preset conductivity distribution.

The proposed two methods are utilized to estimate the conductivity distribution for two scenarios: 1) Large variation (q_o=0.3), 2) Small variation (q_o=0.03). The simulated results are compared with the preset conductivity distribution in Figure 5.12 and Figure 5.13. To eliminate the boundary effects on the conductivity estimation, only the estimated results in the central area of the conductor with the size 60×60×1(mm) are represented.

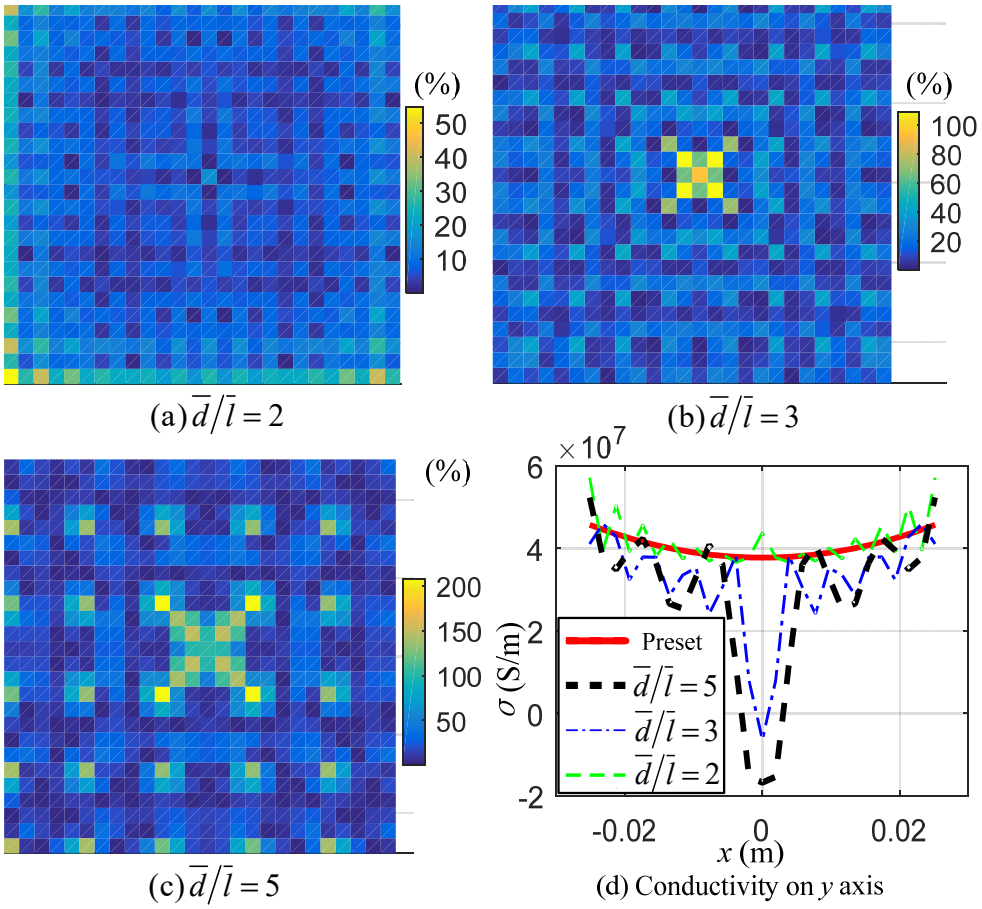

(a) $\bar{d}/\bar{l}=2$ (b) $\bar{d}/\bar{l}=3$ (c) $\bar{d}/\bar{l}=5$ (d) Conductivity on y axis

Figure 5.14 Conductivity estimation with different ratio using method 1

Table 5.8 Three configurations of sensor arrays

	1	**2**	**3**
$\bar{d}$ (mm)	4	6	10
Ratio $\bar{d}/\bar{l}$	2	3	5
Ratio $\bar{d}/\bar{a}$	0.78	1.17	1.95
Location(mm)	$x, y = -28{:}4{:}28$	$x, y = -27{:}6{:}27$	$x, y = -25{:}10{:}25$
Number	225	100	36

As an ill-posed inverse problem, sensor array configuration has critical effects on conductivity estimation for both methods. The sensor configurations for Method 1 (based on the ECD field reconstruction) and Method 2 (derivative method) are characterized by $\bar{d}/\bar{a}$ and $\bar{d}/\bar{l}$ respectively, where $\bar{l}$ is the characteristic dimension of the elements (smallest

dimension). With the sensor array configurations represented in Table 5.8, several simulations using the evenly divided elements with the size of 2×2×1(mm) have been performed for the conductivity estimation. Similar to Figure 5.12 and Figure 5.13, simulation results of estimation error and conductivity distribution on the y axis are compared with the preset value for both methods in Figure 5.14 and Figure 5.15.

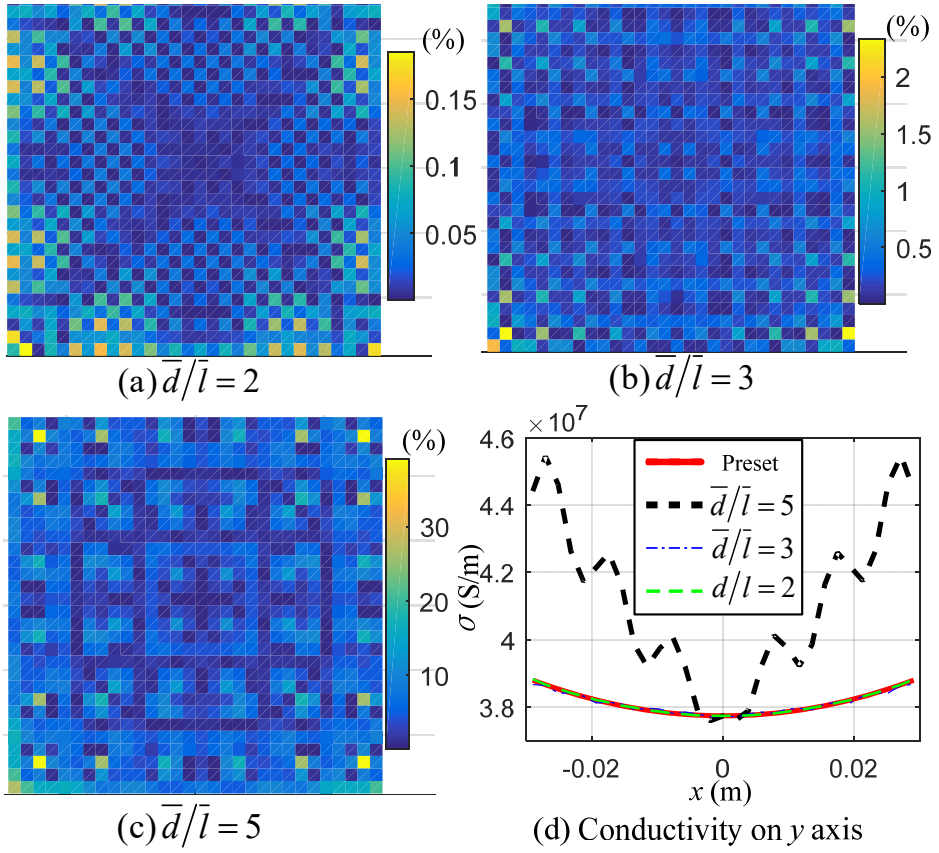

Figure 5.15 Conductivity estimation with different ratio using method 2

B. Case 2 (with boundary)

To illustrate the conductivity estimation with boundary effects, a conductive plate with the dimension of 30×30×1(mm) is placed under the EM with one corner located on z axis as illustrated in Figure 5.2(c). As Case 1, the conductivity distribution for Case 2 is

represented with (5.11) and two scenarios are considered: 1) Large variation (q_o = 0.3), 2) Small variation (q_o = 0.03). Only the derivative method (Method 2) is applied to this case with the details of conductor division and sensor configuration represented in Table 5.9. The simulated results are compared with the preset conductivity distribution in Figure 5.16. Meanwhile, the estimated results with the sensor configurations shown in Table 5.8 for the case with boundary effects are presented in Figure 5.17.

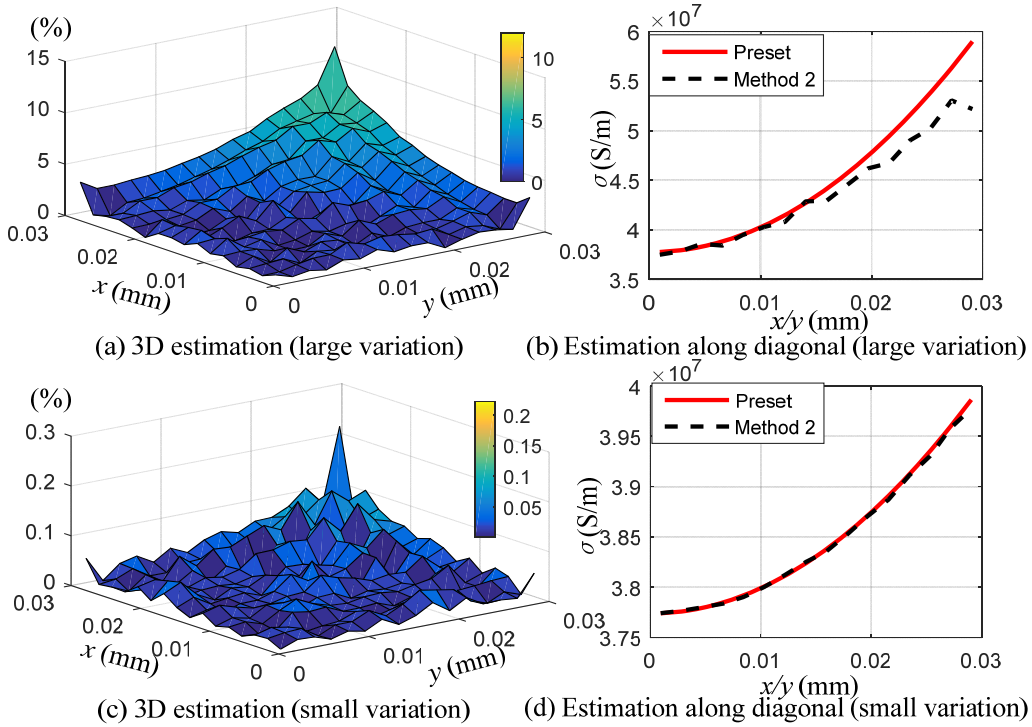

(a) 3D estimation (large variation) (b) Estimation along diagonal (large variation)

(c) 3D estimation (small variation) (d) Estimation along diagonal (small variation)

Figure 5.16 Conductivity estimation with boundary effects

Table 5.9 Conductivity estimation parameters for Case 2

The location of MFD measurements		z=−7mm, x, y = (0:3:30) mm	
Conductor size	30×30×1(mm)	**Measurement number**	100
Element size	2×2×1(mm)	**Element number**	256

Some observations can be made from the simulation results from Figure 5.12 to Figure 5.17:

- As shown in Figure 5.12, with a large variation of conductivity distribution, the errors of the estimated results closed to the boundary using Method 1 is tremendously larger than that using Method 2 whereas the errors in the area of the boundary using Method 1 is much smaller than that using Method 2.
- The estimation errors in the area under the center of the EM are larger than other areas for both scenarios and methods as shown in Figure 5.12 and Figure 5.13. The eddy current in this area is relatively small. The low SNR leads to the poor estimation results.
- For the scenario without boundary effects, as shown in Figure 5.13, the errors estimated by Method 1 are relatively large whereas the errors estimated by Method 2 are small in the whole area when the variation of conductivity is small.
- Considering the boundary effects, as shown in Figure 5.13 and Figure 5.16, Method 2 has much better estimation results with small conductivity variation than that with large variation.
- As shown in Figure 5.16, the estimated results using Method 2 close to the boundary are very accurate especially for the case with small variation.
- As shown in Figure 5.14, Figure 5.15 and Figure 5.17, with the increase of sensor interval (decrease of the measurement number), the estimation error dramatically increases especially for Method 1, which indicates that Method 1 is much more sensitive to the sensor configuration than Method 2.

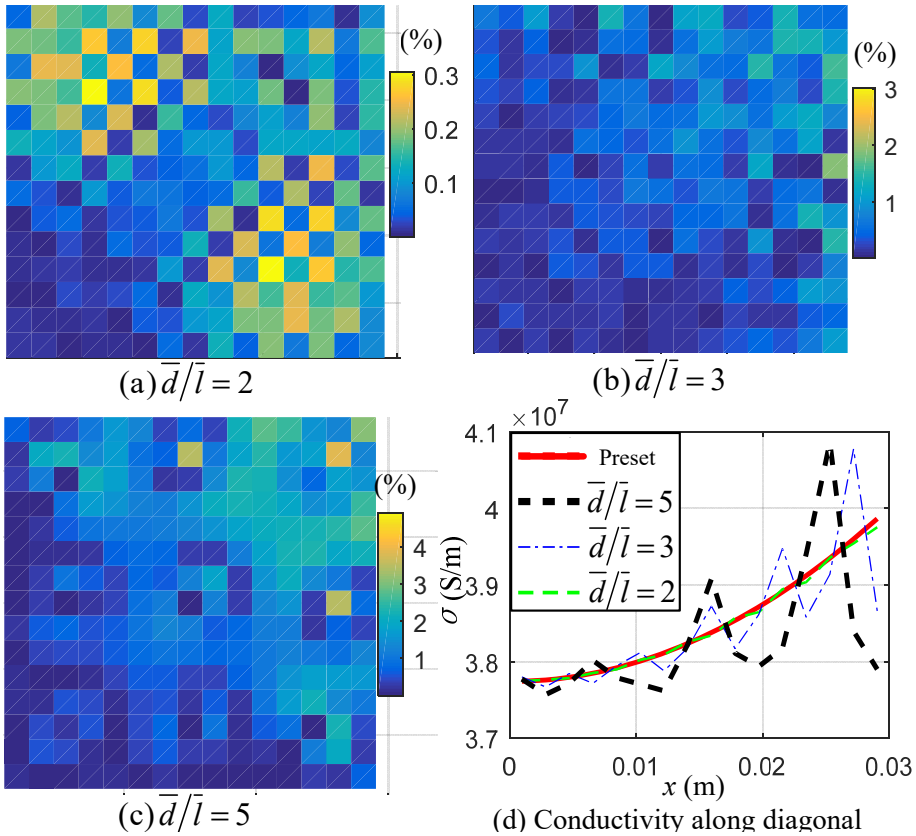

Figure 5.17 Conductivity estimation with different ratio

5.3.3 Cavity Defect Localization/Identification

As theoretically presented in the last section, the cavity defects can be identified and localized using MFD measurements. Several simulations are performed to demonstrate the accuracy and efficiency of this method. As illustrated in Figure 5.2(b), the EM is placed in the middle of a conductive plate (size: 60×60×4, unit: mm) with the cylindrical axis perpendicular to the plate. To simplify the simulation, the current frequency is set to 200Hz and the phenomenon of the skin effect is not obvious due to the relatively low current frequency. Meanwhile, the adaptive element refinement is not applied in this simulation.

The eddy-current generated MFD provided by COMSOL is collected on the plane z_S = 10mm. Two Plans (P1 and P2) of element division for the conductor are simulated,

where the simulation parameters are detailed in Table 5.10. Two commonly seen geometries (cylindrical and slot cavities) have been simulated in this section.

The resolutions of localization and identification depend on the characteristic dimension of the elements $\bar{l}$ (smallest dimension). With the sensor array configurations in Table 5.8, simulation results using evenly divided elements with the size of 2×2×4(mm) are presented in the following subsection for the cylindrical and slot cavities.

Table 5.10 Parameters of defect identification and localization

The location of MFD measurements		$z = -10$mm, $x, y = (-28.5{:}3{:}28.5)$ mm	
Measurement number	400	**Conductor size**	60×60×4(mm)
Element size / number	P1: 2×2×1(mm) / 3600	P2: 2×2×4(mm) / 900	

A. Cylindrical Defect

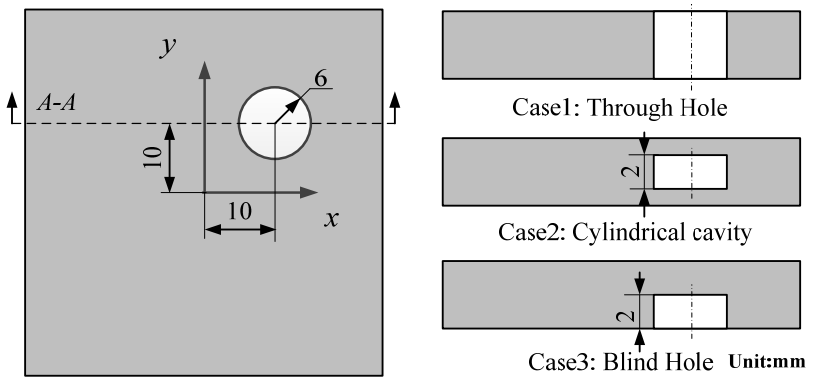

(a) Cylindrical defect Location (b) A-A intersection for 3 cases

Figure 5.18 Cylindrical defect setting

As illustrated in Figure 5.18(a), on the *x*-*y* plane, a hole with a radius of 6mm is located at (10, 10) mm. Determined by the length or depth of the cylindrical defect in *z* axis, there are three cases with the intersection *A*-*A* shown in Figure 5.18(b). The simulated results using P1 and P2 are manifested in Figure 5.19 and Figure 5.20 respectively for all three cases. The plots in each column of Figure 5.19 represent the simulation results of

different layers for one case. There is only one layer as shown in Figure 5.20 when using P2. The effects of the measurement distribution are illustrated in Figure 5.21 for the through hole using different ratio $\bar{d}/\bar{l}$.

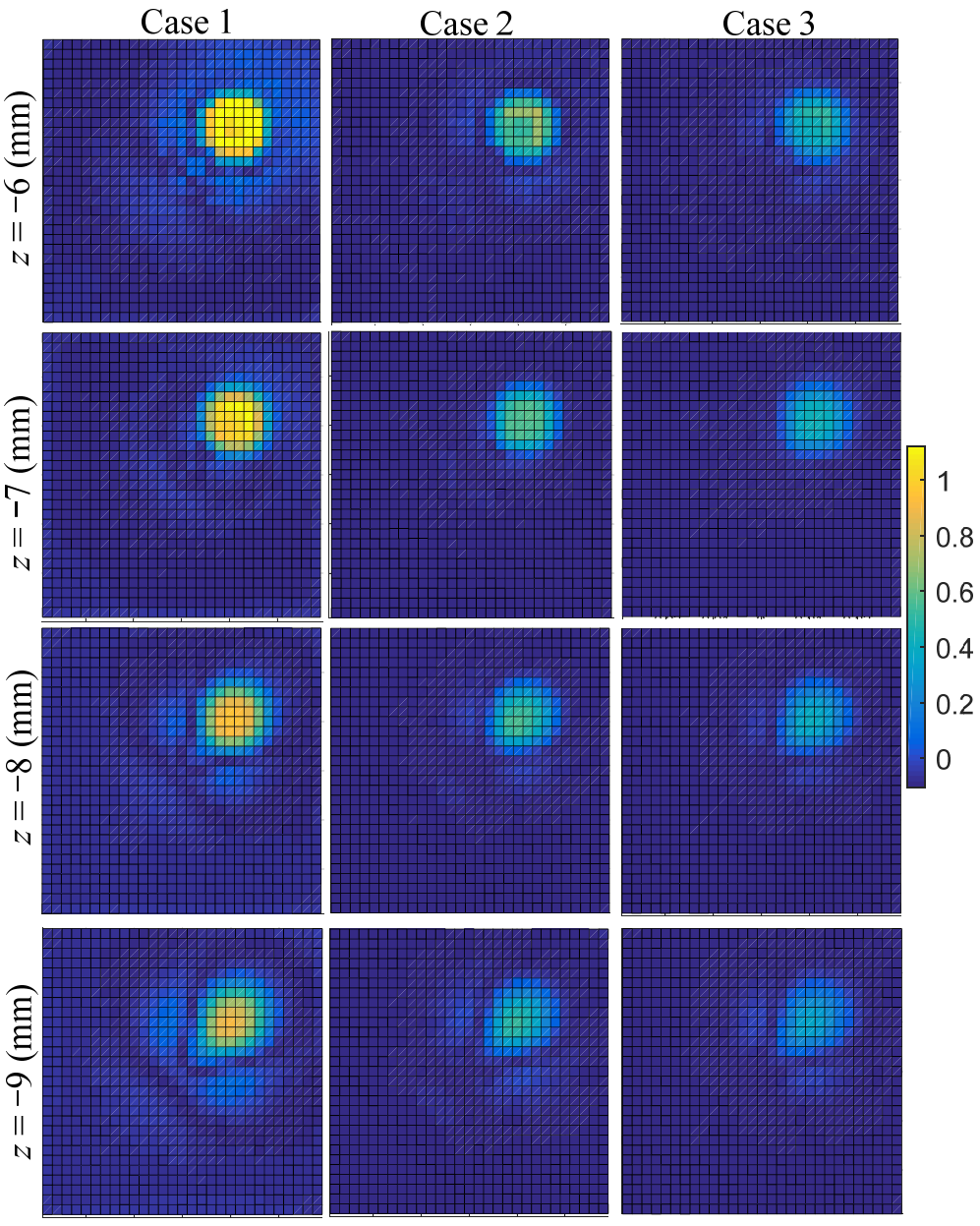

Figure 5.19 Cylindrical defect estimation using P1

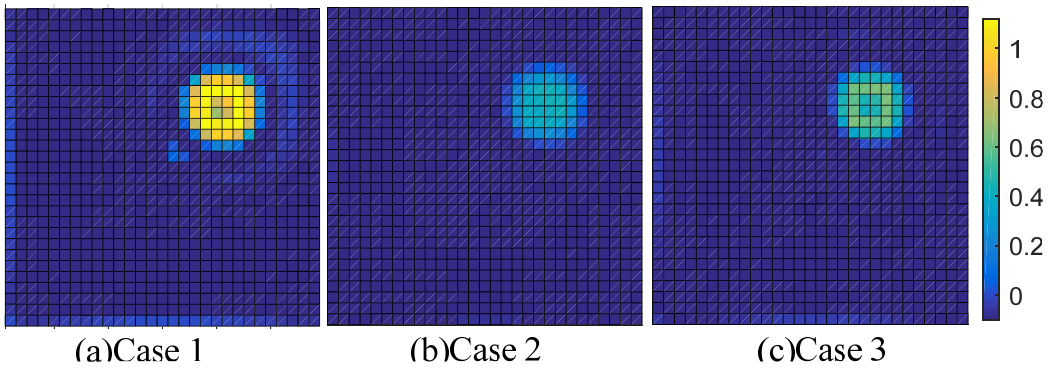

Figure 5.20 Cylindrical defect estimation using P2

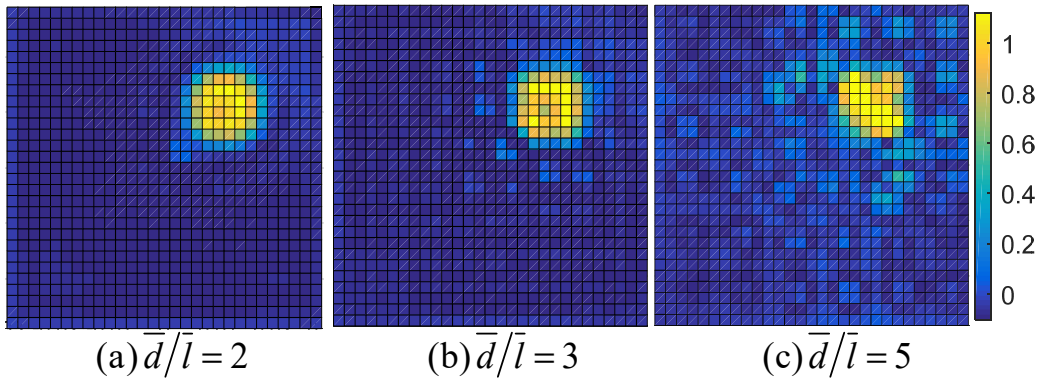

Figure 5.21 Defect estimation using different ratio

B. Slot Defect

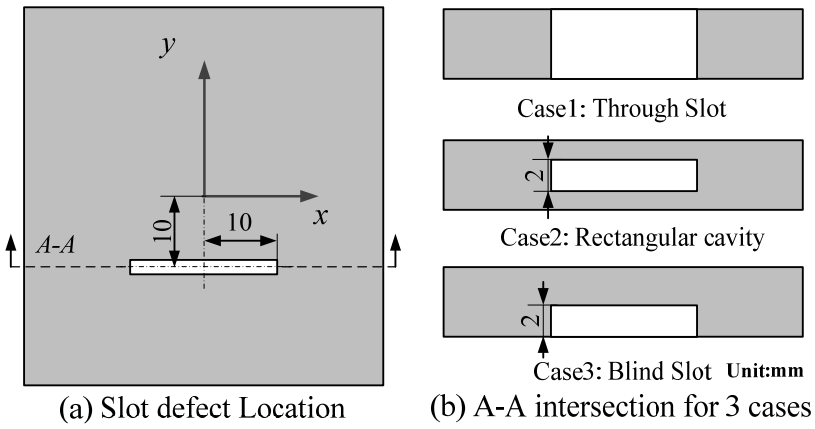

Figure 5.22 Slot defect setting

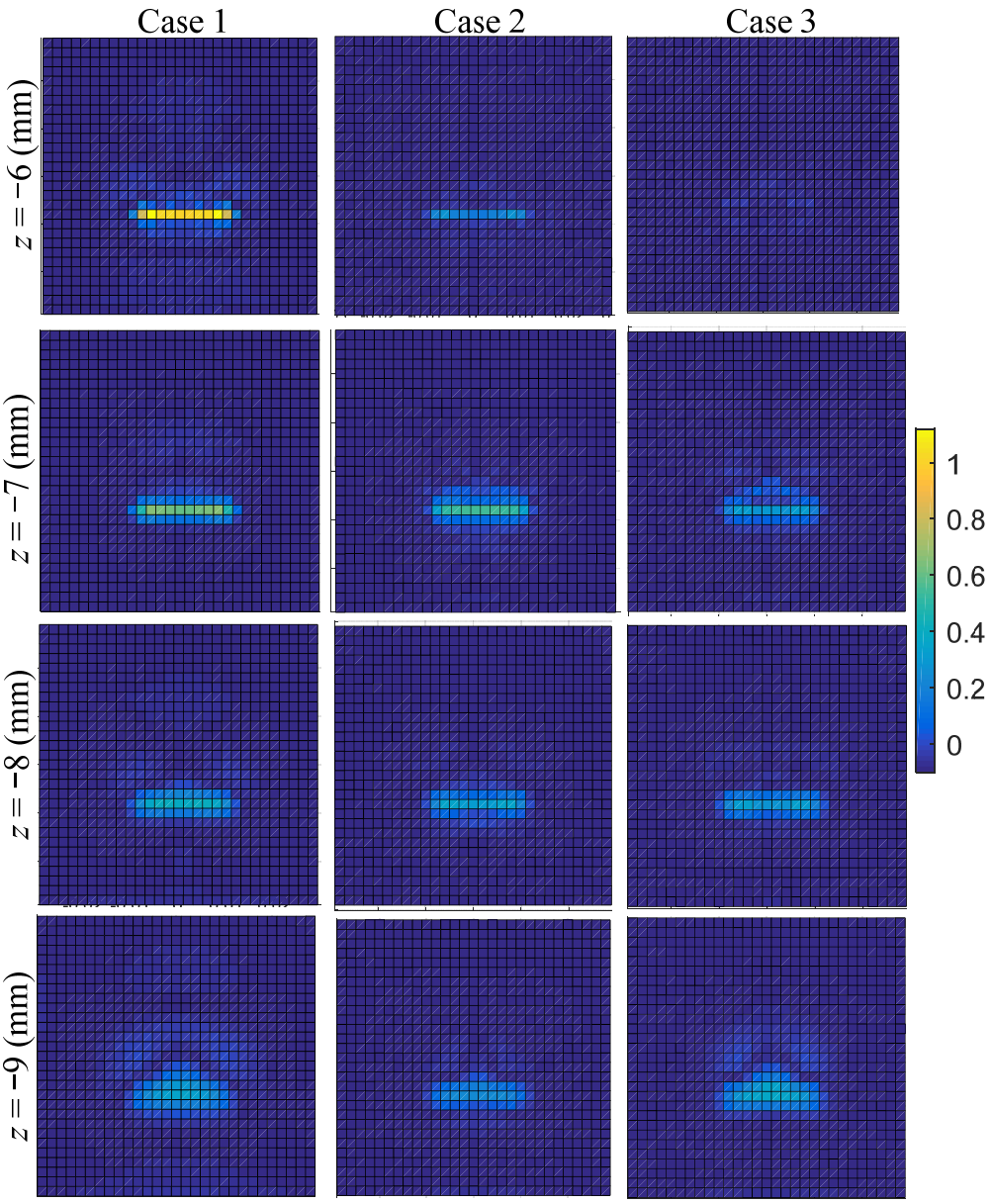

Figure 5.23 Slot defect estimation using P1

As shown in Figure 5.22(a), the center of a slot with the size of 20mm×2mm is located at (0, −10) mm on the *x*-y plane. Considering the depth of the slot defect in the *z* direction, there are three cases with the intersection *A*-*A* shown in Figure 5.22(b). Similarly, the simulated results using P1 and P2 are manifested in Figure 5.23 and Figure 5.24

respectively for all three cases. The effects of the measurement distribution are illustrated in Figure 5.25 for the through slot using different ratio $\bar{d}/\bar{l}$.

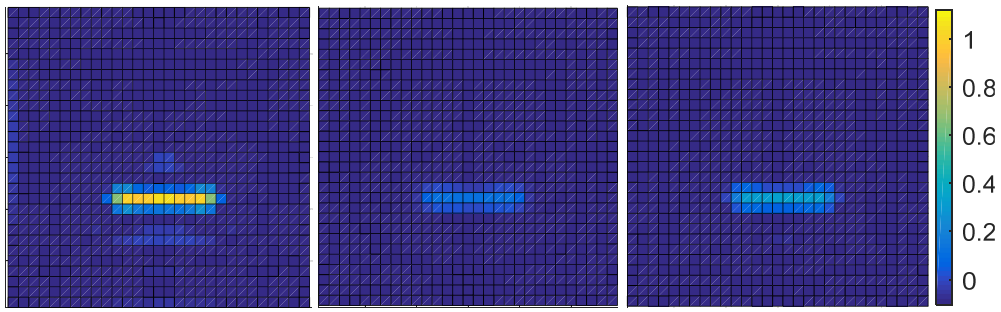

(a)Case 1 (b)Case 2 (c)Case 3

Figure 5.24 Slot defect estimation using P2

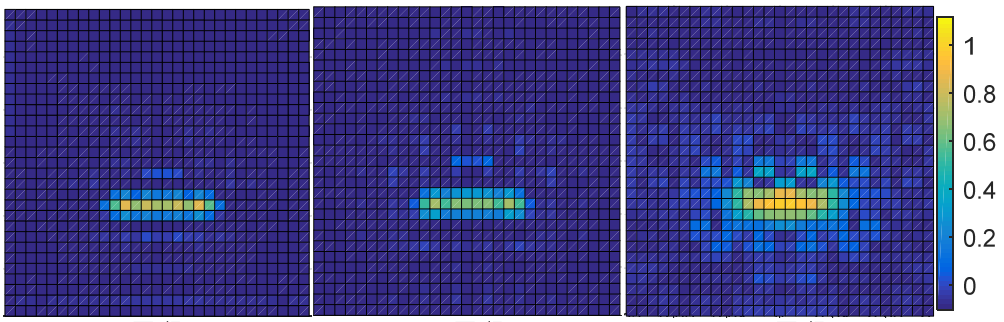

(a) $\bar{d}/\bar{l}=2$ (b) $\bar{d}/\bar{l}=3$ (c) $\bar{d}/\bar{l}=5$

Figure 5.25 Defect estimation using different ratio

C. Results Analysis and Discussion

Some observations can be made from the simulation results from Figure 5.19 to Figure 5.24.

− As shown in Figure 5.19 and Figure 5.23, the location and shape of the defects can be successfully estimated on each layer. The results get worse as the distance between the layer and EM increases.

- Simulation results with P1 shown in Figure 5.19 and Figure 5.23 cannot indicate the depth of the defects which may be caused by the configuration of the magnetic sensors.
- As shown in Figure 5.20 and Figure 5.24, the estimated location and shape of the defects with P2 is better than that with P1. The elements with yellow color indicate through defects whereas the elements with light blue indicate internal defects.
- As illustrated in Figure 5.21 and Figure 5.25, the quality of the defect estimation decreases with the increase of ratio $\bar{d}/\bar{l}$. The edge of the estimated defect becomes blurry and some shadows come out close to the estimated defects.
- Even with the same size of defects, the estimation results of Case 3 are better than that of Case 2. The closer the defects are to the magnetic sensor, the better the estimation results will be.

5.4 Experimental Result and Discussion

A prototype eddy-current sensing system has been developed to demonstrate and illustrate the effectiveness and accuracy of the ECD reconstruction method and two extended applications (conductivity estimation and cavity defect localization/identification) in manufacturing.

5.4.1 Experimental Setup

Table 5.11 Parameters of the coil

a_i	6.5mm	I_o	1A
a_o	7.7mm	N	60 #
a	3.65mm	f	1kHz

As illustrated in Figure 5.26, the experimental setup consists of an analog magnetic sensor array mounted on a printed circuit board (PCB), voltage/current amplifiers, an EM,

analog-to-digital (AD) converters, a function generator, three-dimensional (3D) precision motion stage and a computer. The EM with the parameters illustrated in Table 5.11 is attached to the motion stage using a rod, which can move the EM to desired locations very accurately. To collect analog outputs from all the magnetic sensors simultaneously, an NI (National Instruments) device cDAQ-9178 with three modules NI-9205 was utilized. The computer communicates with the NI devices using USB port. The voltage amplifiers are used to amplify the magnetic sensor output before data collection whereas the current amplifier generates a sinusoidal current flowing through the EM with the input generated by the function generator. By measuring the voltage of the sampling resistor connected with the EM in series, the excitation current can be calculated accurately.

Considering the manufacturing feasibility of the sensor board and the effects of ratio $\overline{d}/\overline{a}$ and $\overline{d}/\overline{l}$ on the errors of ECD reconstruction, conductivity estimation and defect identification/localization, the sensor array consists of 5×5 analog magnetic sensors (HMC1052 with two sensitive axes) with spacing interval 10mm. For the experiments, the sinusoidal current frequency is set to 1kHz whereas the sampling rate for each channel is set to 10kHz. As shown in Figure 5.26(d), to reduce the influence of the magnetic field generated by the EM, the conductor is placed between the sensor board and EM.

All the magnetic sensors are mounted on the PCB accurately. The magnetic sensor outputs are linear within the operating range. The gains for different sensors are unidentical. To guarantee the measuring accuracy, all the sensors need to be calibrated. Ideally, all sensors should have identical outputs when placed in the space filled with a constant magnetic field. Thereby, to calibrate the sensor array is to obtain the gain factor of each sensor respect to the reference sensor.

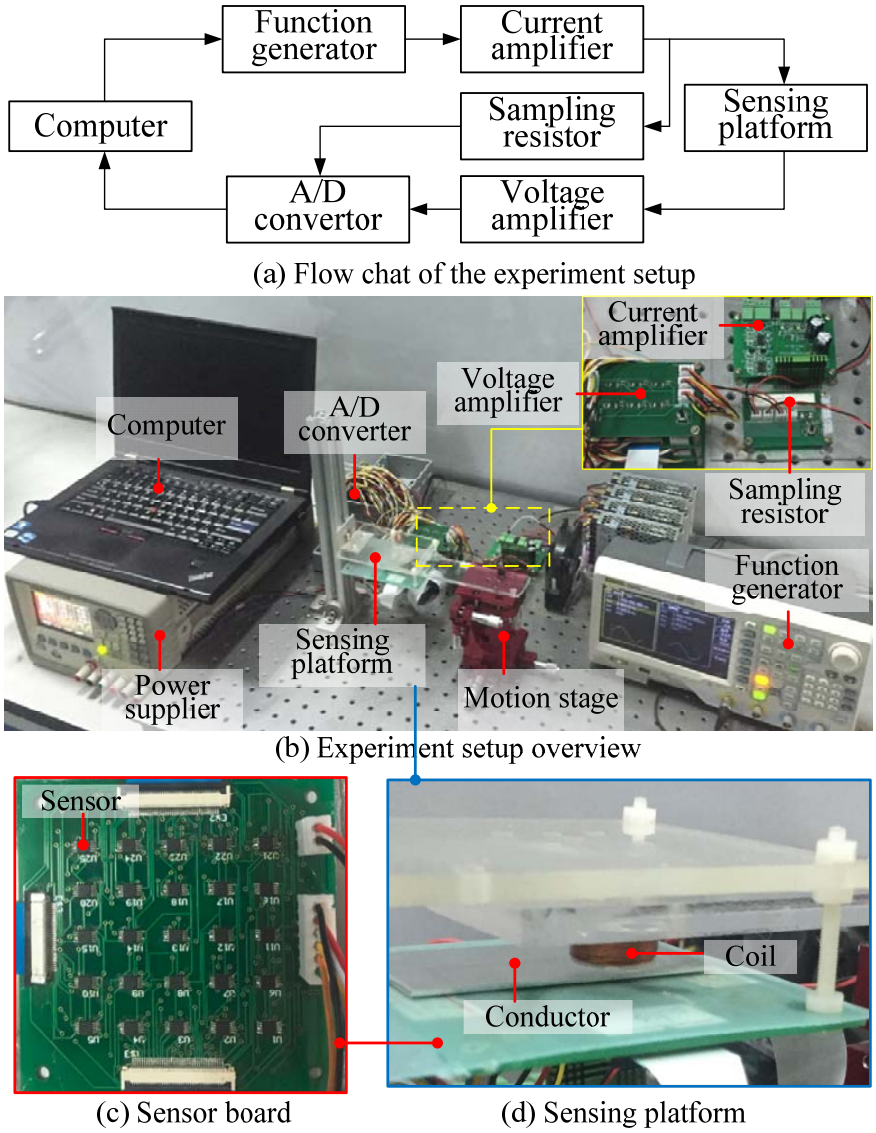

Figure 5.26 Experimental setup for eddy current reconstruction

To obtain the gain ratio of the two axes outputs of the reference sensor and relate the outputs (voltage) of the analog magnetic sensors to the actual MFD data, a precise magnetic sensor with two sensitive axes is in high demand. Laser displacement sensor LK-H025 provided by Keyence, digital 3-axis magnetic sensor BMC050, 3D precision motion stage and a cylindrical PM are introduced for the sensor calibration.

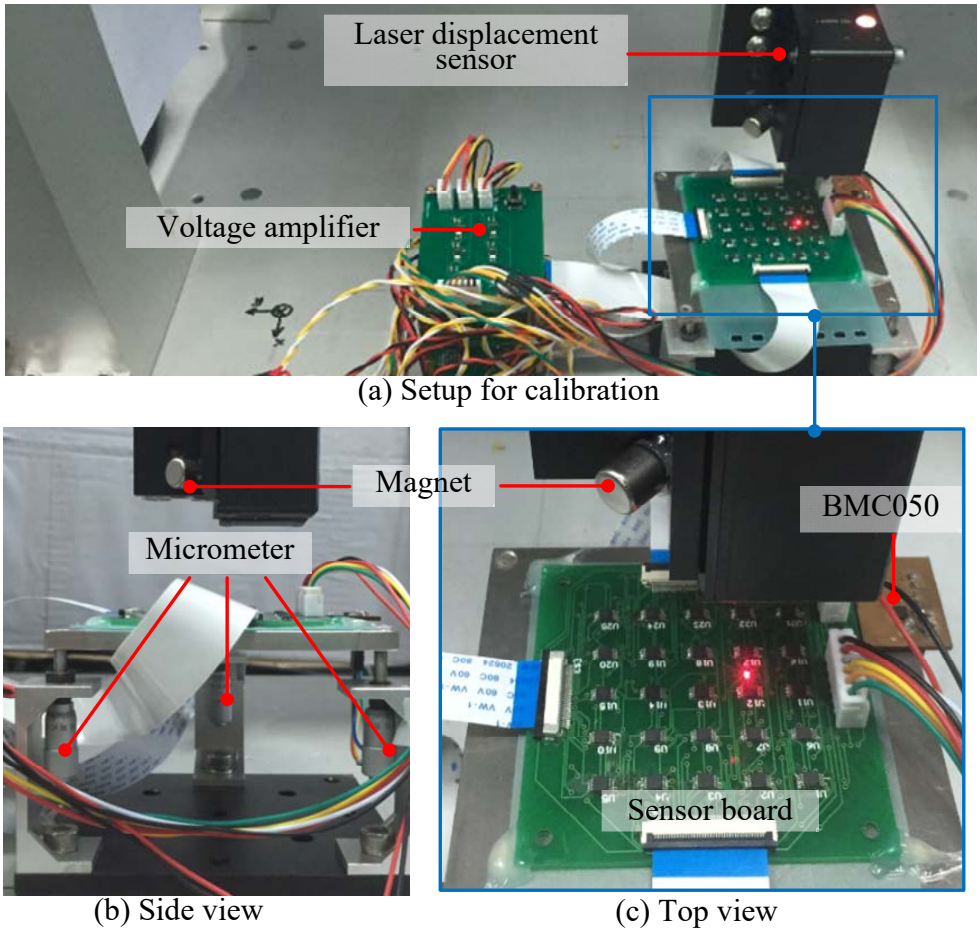

(a) Setup for calibration

(b) Side view

(c) Top view

Figure 5.27 Setup for sensor calibration

As illustrated in Figure 5.27, with all the sensor coordinates in parallel, both the sensor board and the PCB with BMC050 are mounted on the titanium plate (non-magnetic) supported by three micrometers which can adjust the levelness of the titanium plate. The laser displacement sensor is attached to the 3D motion stage. By moving the laser sensor, the output of the laser sensor guides the adjustment of levelness. Meanwhile, the red laser point projected on the sensor board helps to make the row and column of the sensor array parallel to two moving axes of the 3D motion stage. Attached by a cylindrical PM, 3D motion stage moves to each magnetic sensor (including BMC050) to keep the same relative position between the corresponding sensor and PM and the output (V_{cxi}, V_{cyi}) of the

corresponding analog sensor and (B_{cx}, B_{cy}) of BMC050 are collected at each position respectively. The digital magnetic sensor is chosen as the reference and the gain factors (a_i, b_i) can be obtained as (5.12a, b):

$$a_i = B_{cx} / V_{cxi}\,,\ b_i = B_{cy} / V_{cyi} \tag{5.12a, b}$$

where i=1, 2, 3…25.

The calibrated MFD for each analog magnetic sensor can be represented as below:

$$B_{xi} = a_i V_{xi}\,,\ B_{yi} = b_i V_{yi} \tag{5.13a, b}$$

where (V_{xi}, V_{yi}) are the voltage output of the i^{th} magnetic sensor, (B_{xi}, B_{yi}) are the corresponding MFD measurements.

5.4.2 ECD Field Reconstruction and Tracking

Electrically conductive metals, such as aluminum or aluminum alloy have been utilized to perform the ECD field reconstruction and tracking using the finite measurements of the MFD field. Eddy current flows inside the conductor which makes it almost impossible to measure directly. Thereby, the experimental results are compared with the simulation results provided by COMSOL.

Table 5.12 Reconstruction parameter for the experiment

The location of MFD measurements		z=−12.5mm, x, y=(−20:10:20) mm	
Measurement number	25	k	0.1
Initial element size	5.6×5.6×3(mm)	Q_M	4
Conductor size	56×56×3(mm)	g	30%

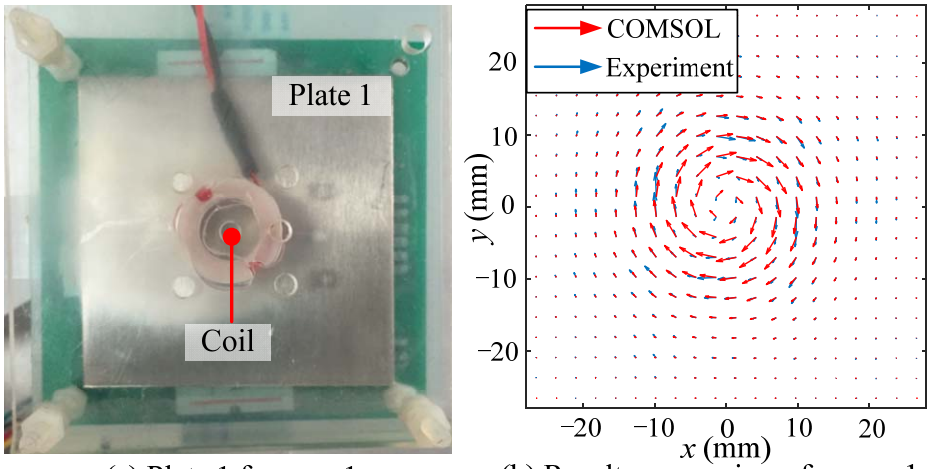

(a) Plate 1 for case 1 (b) Results comparison for case 1

Figure 5.28 Results for case 1

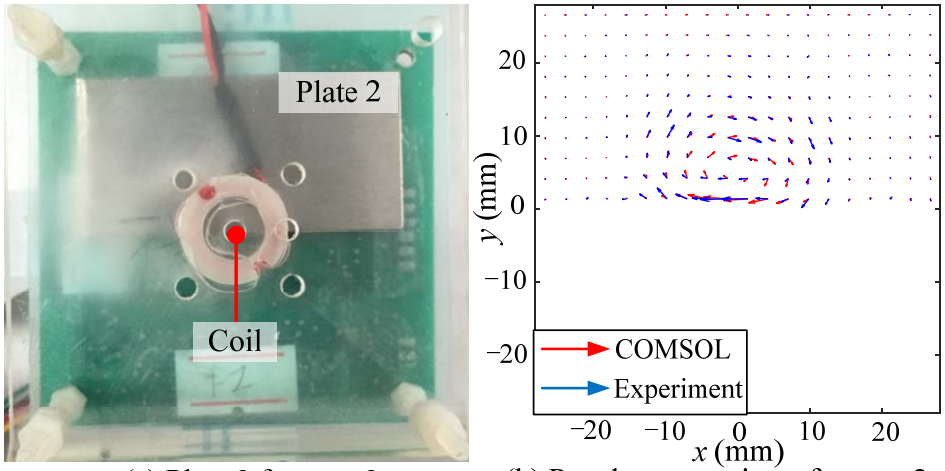

(a) Plate 2 for case 2 (b) Results comparison for case 2

Figure 5.29 Results for case 2

Three cases are introduced as illustrated in Figure 5.28(a), Figure 5.29(a) and Figure 5.30(a). Three plates (with the dimension of 56×56×3, 56×28×3, 28×28×3 respectively, unit: mm) are placed between the sensor board and EM with z_C = 7.1mm. The MFD generated by the eddy current is collected by the magnetic sensor array with z_S = 12.5mm. More details of the reconstruction parameters are presented in Table 5.12. Similar

to the simulations, the adaptive element refinement was only applied in *x*-*y* plane for simplicity. Reconstructed results are compared with simulations in Figure 5.28(b), Figure 5.29(b) and Figure 5.30(b).

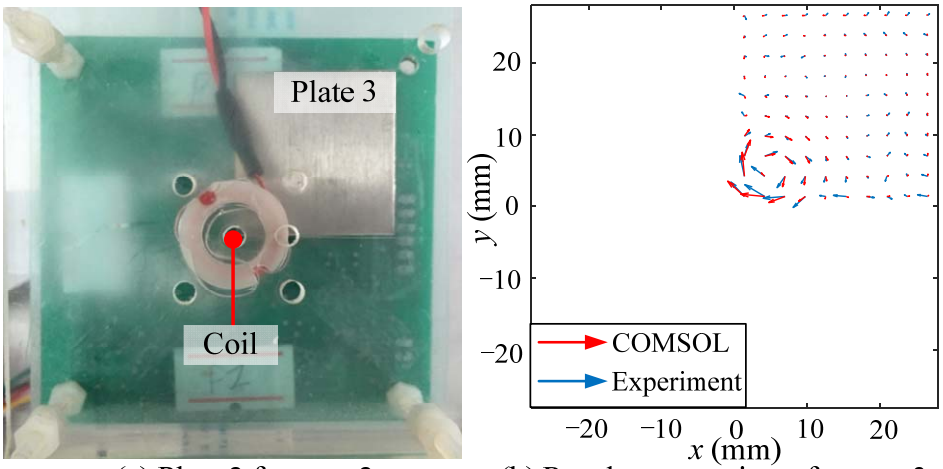

(a) Plate 3 for case 3 (b) Results comparison for case 3

Figure 5.30 Results for case 3

Similar to the simulations, the ECD is reconstructed by acquiring the MFD generated by the eddy current when moving the EM on *x*-*y* plane as shown in Figure 5.31, in which the red circles indicate the EM location for each case with the center location shown below each figure (unit: mm). The tracking error of the eddy current for different locations is also represented in Figure 5.31.

Some observations can be drawn from the experimental results:

- The reconstructed and simulation results have the similar eddy current field distribution patterns tremendously affected by the boundary of the conductors.
- The errors of the reconstructed results for Plate 1 is smaller than those for plate 2 and 3.
- With the method of ECD reconstruction, the movement of the eddy current can be successfully tracked. However, the tracking error is much larger than that of simulation

results especially in the x direction, which is caused by the measurement errors and fewer measurements.

- The reconstructed eddy-current field is consistent with simulation in most area of the conductor.

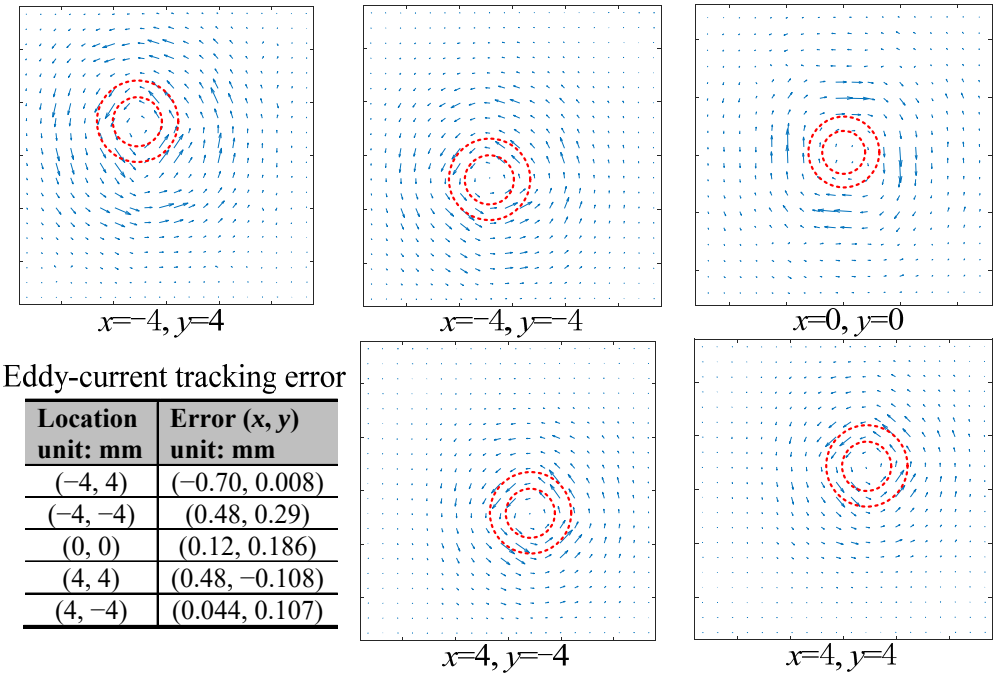

Eddy-current tracking error

Location unit: mm	Error (x, y) unit: mm
(−4, 4)	(−0.70, 0.008)
(−4, −4)	(0.48, 0.29)
(0, 0)	(0.12, 0.186)
(4, 4)	(0.48, −0.108)
(4, −4)	(0.044, 0.107)

Figure 5.31 ECD localization for different coil locations

The reconstruction errors can be accounted for three parts. The first part is the measurements. The second part is related to the mathematical regularization. Even all the gains of the magnetic sensor have been calibrated, the location error, especially the orientation error, will introduce extra errors to the calibration, which are not considered in this article. Meanwhile, the error of the digital sensor and AD converter may affect the final reconstructed results. Using 25 measurements to estimate the eddy current in more than 400 elements may ignore the details of the eddy current which are represented as the reconstructed error. Although the physical constraints can suppress the measurement noise,

they can also introduce errors into the results. That is why the results of case 1 are better than those of case 2 and 3 with same measurement noise level. The errors of the setup are the third part such as errors of the coil shape, the relative location of the conductor and coil and so on.

5.4.3 Conductivity Estimation

As illustrated in Figure 5.32, the two types of plates with the dimension of 56×56×1 and 56×28×1 (unit: mm) respectively are utilized in the experiments. For each type of plates, they are made of aluminum alloy 6061 and 7075 with the conductivity 2.16×10^7 and 1.903×10^7 (unit: S/m) respectively. To eliminate the effects of the error between the simulation and experiments, in the experiments, $\overline{\mathbf{B}}_E$ is directly collected using the conductor with known conductivity instead of using simulation value.

By placing the conductors between the sensor array and EM as illustrated in Figure 5.26(d), the experimental results of conductivity estimation using two methods are manifested in Figure 5.33 and Figure 5.34.

Table 5.13 ECD field reconstruction parameters

The location of MFD measurements		z=−12.5mm, x, y=(−20:10:20) mm	
Measurement number	25	**Initial element size**	5.6×5.6×3(mm)
Q_M	4	g	30%

Using the conductivity estimation method based on ECD field reconstruction (Method 1), the estimated ECD field and conductivity of the full plate made of aluminum alloy 6061 are represented in Figure 5.33 with the detail reconstruction parameters shown in Table 5.13. To eliminate the boundary effects on the estimation results, only the

estimated results in the central area of the conductor with the size of 30×30×1(mm) are represented (as shown in Figure 5.33b).

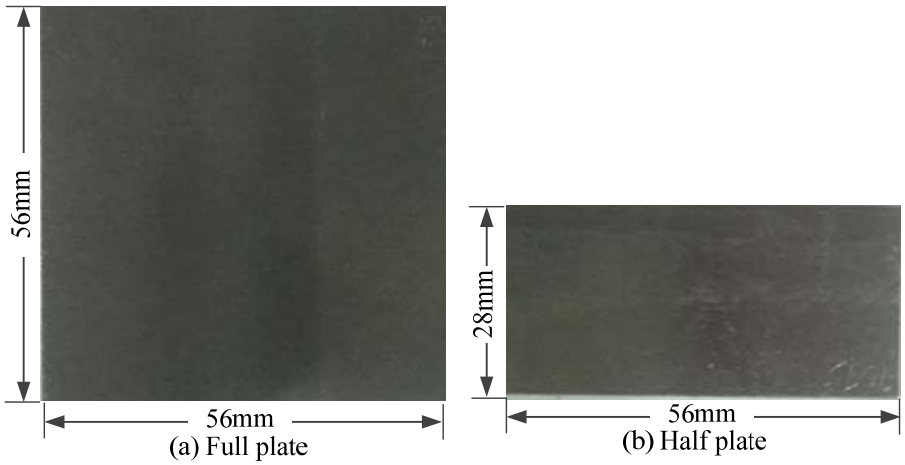

Figure 5.32 Experimental samples for conductivity estimation

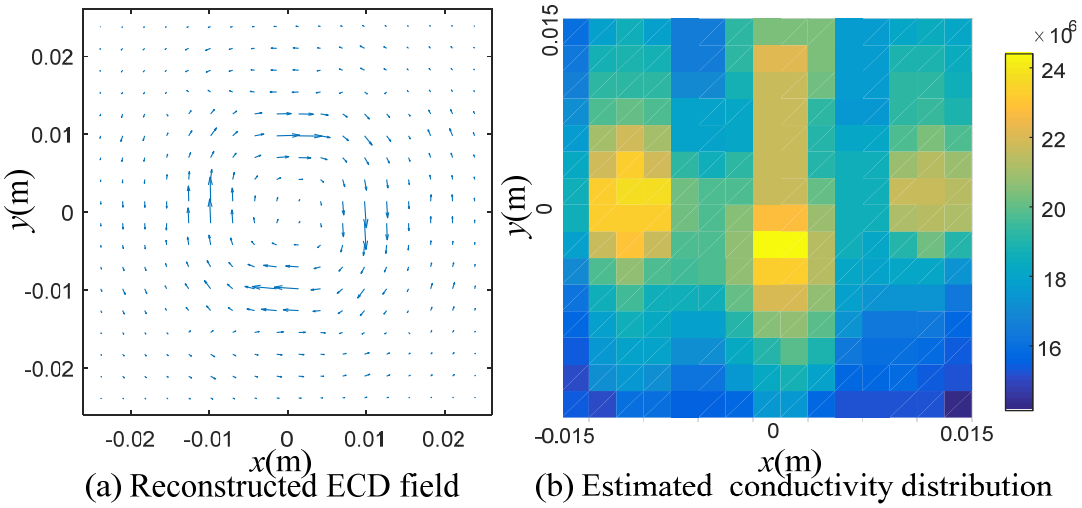

Figure 5.33 Conductivity estimation for 6061 using Method 1

As illustrated in the simulation, derivative method (Method 2) can also estimate electrical conductivity with the conductions of conductivity continuity and small deviation regardless of boundary effects. Since aluminum alloy 6061 and 7075 have relatively close conductivity, using the information of either material, the conductivity of the other can be

estimated with Method 2. We assume the conductivity of 7075 is known and estimate the conductivity of 6061. Using sensor configuration manifested in Table 5.13 and evenly divided element with the size of 1.86×1.86×1(mm), the conductivity of full and half plates made of aluminum alloy 6061 is estimated as shown in Figure 5.34.

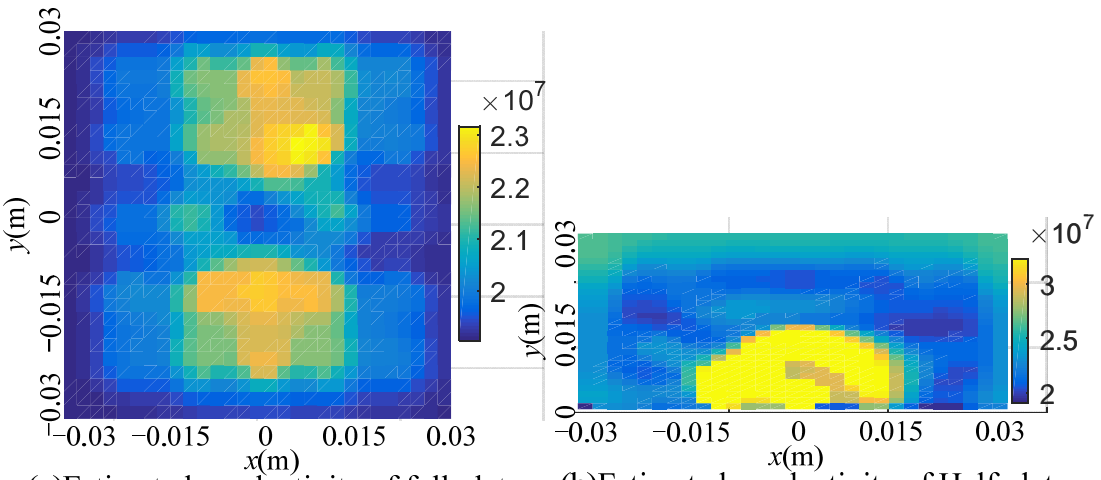

(a)Estimated conductivity of full plate (b)Estimated conductivity of Half plate

Figure 5.34 Conductivity estimation for 6061 using Method 2

Some observations can be drawn from the experimental results represented in Figure 5.33 and Figure 5.34:

- As shown in Figure 5.33 and Figure 5.34, the conductivity of the full and half plates made of 6061 can be estimated by measuring MFD generated by the eddy current.
- Since the generated eddy current is relatively small in the area closed to the boundary and the center of EM which leads to low SNR, the estimation errors in the areas shown in Figure 5.33 and Figure 5.34 are relatively large.
- As shown in Figure 5.34(b), Method 2 can accurately estimate the conductivity of the area closed to the boundary on the *x* axis regardless of boundary effects.

− There are regular patterns for the estimated conductivity shown in Figure 5.33 and Figure 5.34(a). Inspired by the numerical analysis of the sensor configuration in Figure 5.14 and Figure 5.17, the errors of conductivity estimation mainly come from the improper sensor configuration (large sensor interval) especially for the case using Method 1.

− The measurement errors of MFD and the dimension error of the experimental setup, sensor configuration and EM may also lead to the error of conductivity estimation.

5.4.4 Defect Localization and Identification

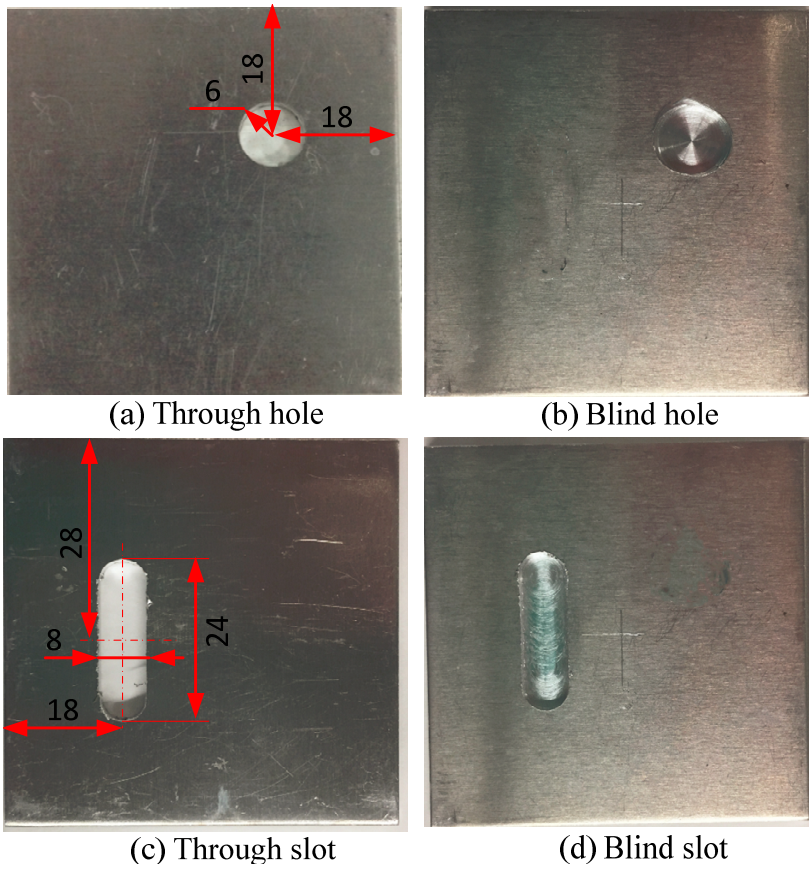

(a) Through hole (b) Blind hole

(c) Through slot (d) Blind slot

Figure 5.35 Cavity defects samples

Four types of cavity defects shown in Figure 5.35 are utilized in the experiment. The plate is made of aluminum with the dimension of 56×56×3 (mm). The depth of the

blind hole and slot is 1.5mm. The parameters of defect identification and localization are shown in Table 5.14.The size and location of the hole and slot are manifested in Figure 5.35. Blind hole and slot have exactly the same size and location as the through hole and slot respectively. The corresponding experimental results are manifested in Figure 5.36.

Table 5.14 Parameters of defect identification and localization

The location of MFD measurements		z=−12.5mm, x, y=(−20:10:20) mm	
Measurement number	25	**Conductor size**	56×56×3(mm)
Element size	2.8×2.8×3(mm)	**Element number**	400

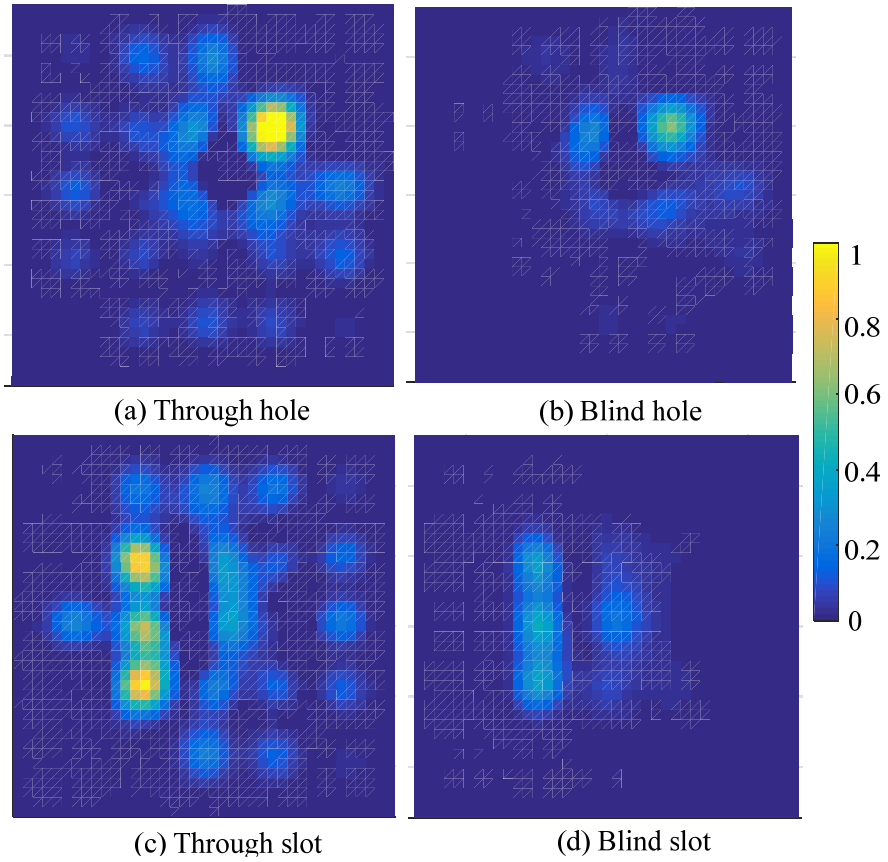

Figure 5.36 Cavity defects estimation

Some observations can be drawn from the experimental results:

- The cavity defects (hole and slot) can be located and estimated by using MFD measurements.
- The corresponding elements in the areas of through defects are approximately equal to 1 whereas those elements in internal defects (interpreted using blind hole and slot) are approximately equal to the values less than 1.
- Besides the actual defects, there are several shadows which have similar shapes of the defects in the results. They seem to follow a certain pattern as shown in Figure 5.36. The intensity of the shadows is much smaller than that of actual cavity defects.
- Inspired by the simulation results of the sensor configuration effects in the simulation subsection, the phenomenon of shadows may be the results of MFD measurement error and the error of Regularization method due to the large ratio $\bar{d}/\bar{l}$.

5.5 Summary

With the assumption of the MQS condition valid for manufacturing application, the modeling of the eddy-current reconstruction has been explored for two specific manufacturing applications, conductivity estimation and cavity defect identification/localization. By discretizing the conductor, an analytical representation of conductivity has been linearly expressed using the reconstructed ECD field without considering the nonlinear boundary effects. With additional assumption that the conductivity is continuous and varies in a small range, the conductivity has been estimated using linearization method with the sensitivity matrix derived from the forward. Similar to the conductivity estimation, the relationship between the possibility of the existence of the cavity defects and the MFD measurements has been estimated using the forward model and the cavity defects have been consequently identified and localized.

The effectiveness and accuracy of the eddy-current reconstruction, conductivity estimation and cavity defect localization/identification have been demonstrated numerically and experimentally. The eddy-current reconstruction results are compared with the results provided by the theoretical model and commercial FEM software COMSOL. With the simulated magnetic field (generated by the eddy current) added with different level Gaussian noise, the ECD field has been well estimated for two cases. The simulation results also indicate that the reconstruction accuracy decreases with the decrease of the measurement SNR and the additional physical constraints have the ability to suppress the effects of the measurement noise. The errors of ECD reconstruction and localization increase with the increase of the ratio $\overline{d}/\overline{a}$.

With two preset conductivity distributions (large and small variation) for both cases (with and without boundary effects), the conductivity has been estimated using two methods and compared with the preset value. Both methods can estimate the conductivity accurately. Derivative method (Method 2) can deal with the case with boundary effects and has a better estimation when the conductivity varies in a small range whereas Method 1 has better performance as the conductivity variation is large. With the increase of sensor interval (decrease of measurement number), the estimation error dramatically increases for both methods. Two types of cavity defects (slot and hole) are utilized for the numerical investigation of the defect localization/identification method. With the proposed method, both types of defects have been successfully localized and identified. Similarly, with the increase of sensor interval (decrease of measurement number), the quality of the defect estimation decreases and the edge of the estimated defect becomes blurry and some shadows come out close to the estimated defects.

A self-built experimental setup consisting of a sensor array (5×5 two-axis magnetic sensors), an air-cored EM and other hardware is utilized to perform several experiments similar to the numerical investigation. Even though there are some errors comparing to the simulation results which may come from the error of the measurements and setup parameters, the experimental eddy-current field reconstructed using the finite MFD measurements is consistent with the simulations in the most area of the conduction and the location of the eddy-current field has been successfully tracked. Meanwhile, the conductivity of the full and half plates made of aluminum alloy has been successfully estimated, although the estimation error close to the boundary and EM center is relatively large due to low SNR. There are regular patterns for the estimated conductivity and the errors mainly come from the improper sensor configuration (large sensor interval) besides the measurement errors of MFD and the dimension error of the experimental setup. Similar to the simulations, four types of cavity defects have been successfully located and identified using MFD measurements. Although there are several shadows which have similar shapes as the defects in the results, the intensity of the shadows is much smaller than that of actual cavity defects. The phenomenon of shadows may be the results of MFD measurement error and the error of Regularization method due to the large ratio $\bar{d}/\bar{l}$ or sensor interval.

CHAPTER 6. CONCLUSION AND FUTURE WORKS

6.1 Accomplishments and Contribution

This dissertation has developed an electromagnetic sensing system for field reconstruction using limited MFD measurements. The potential applications of this novel designed sensing system in visually impaired assistance and manufacturing have been successfully illustrated and validated. The specific contributions include the following:

A. Electromagnetic field reconstruction based on limited MFD measurements

An analytical model of electromagnetic field reconstruction using the limited measurements of the magnetic field has been presented inspired by the simplicity of pole-based models. Illustrated with magnetostatic fields, the far field generated by a magnetic source element can be approximately modeled using a dipole. A gradient-based method for dipole location and moment estimation has been provided. For the near field (illustrated with eddy-current field), an analytical model of eddy-current field reconstruction (including forward and inverse models) using the finite measurements of the MFD field generated by the ECD field has been presented. By discretizing the target/conductor, the forward model is linearly expressed using state-space representation (matrix form). The mathematical method of Tikhonov regularization is utilized to estimate the ECD field with the derived matrix expression.

B. Geomagnetic field-based sensing system for visually impaired assistance

As an extension of the creatively designed electromagnetic sensing system for the visually impaired assistance, a prototype of the gradient-based MTS system consisting of

two orthogonal pairs of three-axis magnetic sensors has been developed. This sensing system can not only locate and identify the man-made magnetic object placed in geomagnetic field (such as magnets, wrench), but also guide VIPs indoor, outdoor and avoid obstacles as a supplement of existing technologies (vision and GPS). The effectiveness and accuracy of this system have been numerically and experimentally illustrated and demonstrated.

C. Eddy-current sensing system for geometrical feature detection in manufacturing

With the assumption of the MQS condition valid for manufacturing applications, the modeling of the electromagnetic field reconstruction has been successfully applied to manufacturing applications, conductivity estimation and cavity defect identification/localization. A newly designed prototype of the eddy-current sensing system with multiple functions can estimate the physical information of the workpiece in certain area/volume with one-time measurement instead of mechanical motion and multiple measurements. Numerical and experimental cases have demonstrated and validate the effectiveness and accuracy of this system.

6.2 Future Works

This research has developed an electromagnetic sensing system for field reconstruction based on finite magnetic field measurements and applied this system to the applications of visually impaired assistance and manufacturing. Further research and possible direction are summarized as follows:

A. Sensing system for autonomous mobile robots

A geomagnetic-field based sensing system designed for visually impaired assistance has the potential to be applied for autonomous mobile robots or vehicles. Beside the magnetostatic field, a new sensing system will integrate multiple passive physical fields or parameters, such as visible light, radiation, inertial (acceleration) to establish an intelligent space that is easy for users to enrich or extract/acquire surrounding information (not only the location and geometry, but also the physical/material information) for specific applications such as autonomous mobile robots or VIPs guide.

B. Eddy-current stimulation and manipulation

The transient eddy-current distribution in a conductor can be represented in closed form with the theoretically presented eddy-current model (forward model), which has considered not only the effects of the conductor deformation, but also the influence of the possible anisotropic physical properties, especially for biological tissues. With the state-space representation of the eddy-current model, by controlling the external sources, it is possible to generate a desired eddy-current pattern at a desired location inside the conductor and optimize the shape and distribution of the external sources (such as EMs) for specific applications, such as neural system (retinal or brain) stimulation.

C. Conductivity reconstruction using eddy-current technologies

The electrical properties have the potential to indicate and uncover other related material properties. For instance, the changes of the electrical conductivity can indicate the internal stress of a metal workpiece which is difficult to measure noninvasively. The biological tissues with cancer contain much more water than healthy tissues, which lead to higher electrical conductivity. Meanwhile, the electrical properties (such as conductivity,

permittivity) of the biological tissue highly depend on the external simulation frequency which introduces additional barriers for examination based on electrical properties of the tissues. Fortunately, the reconstruction model presented in this dissertation has covered the anisotropic effects of conductivity, as well as permittivity which will provide a good basis to extend the method of conductivity estimation used in manufacturing to medical applications, such as medical imaging.

APPENDIX A. ELECTROMAGNETIC MODEL WITH DISPLACEMENT CURRENT

Assume a non-magnetic conductor is placed in the space filled with changing magnetic field and there is no external current inside the conductor. Referring to classical electromagnetic theories, the eddy-current field can be generated inside the conductor. Applying Maxwell' equation inside the conductor domain:

$$\nabla \times \frac{1}{\mu}\mathbf{B} = \mathbf{J} + \frac{\partial \mathbf{D}}{\partial t} \tag{A.1}$$

where **B** is the MFD, **J** is the ECD inside the conductor, **D** is the displacement field with the expression $\mathbf{D} = \varepsilon \mathbf{E}$, μ and ε are the permeability and permittivity of the conductor respectively.

MFD can be represented by the magnetic vector potential **A** using (A.2):

$$\mathbf{B} = \nabla \times \mathbf{A} \tag{A.2}$$

Substituting A.2 into A.1 with $\mathbf{D} = \varepsilon \mathbf{E}$ and Ohm's law ($\mathbf{J} = \sigma \mathbf{E}$),

$$\nabla \times \left(\frac{1}{\mu} \nabla \times \mathbf{A} \right) = \mathbf{J}_P, \text{ where } \mathbf{J}_P = \mathbf{J} + \frac{\varepsilon}{\sigma} \dot{\mathbf{J}} \tag{A.3}$$

Here, $\mathbf{J}_P$ is named equivalent current density. With the condition of $\nabla \bullet \mathbf{A} = 0$, (A.3) can be simplified as below,

$$\nabla^2 \mathbf{A} = -\mu \mathbf{J}_P \tag{A.4}$$

The magnetic vector potential **A**(**r**) at location **r** generated by the current $\mathbf{J}_P$ in the small volume V' can be calculated by solving (A.5).

$$\mathbf{A}(\mathbf{r}) = \frac{\mu}{4\pi}\int_{V'} \frac{\mathbf{J}_P(\mathbf{r}')}{|\mathbf{r}-\mathbf{r}'|}dv' \tag{A.5}$$

Substituting (A.5) into (A.2), the MFD **B**(**r**) at location **r** generated by the current $\mathbf{J}_P$ in the small volume V' is derived as (A.6).

$$\mathbf{B}(\mathbf{r}) = \frac{\mu}{4\pi}\int_{V'} \frac{\mathbf{J}_P(\mathbf{r}')\times(\mathbf{r}-\mathbf{r}')}{|\mathbf{r}-\mathbf{r}'|^3}dv' \tag{A.6}$$

With the assumption that the dimension the volume is relatively much smaller than the distance between **r** and the volume, **A**(**r**) and **B**(**r**) can be approximately expressed with (A.7) and (A.8).

$$\mathbf{A}(\mathbf{r}) \approx \frac{\mu}{4\pi R}\mathbf{J}_P V' = V'\left[\eta_{\mathrm{A1}}(R)\mathbf{J} + \eta_{\mathrm{A2}}(R)\dot{\mathbf{J}}\right] \tag{A.7a, b}$$

$$\mathbf{B}(\mathbf{r}) \approx \frac{1}{4\pi R^2}V'\mathbf{J}_P \times \mathbf{e} = V'\left[\eta_{B1}(R)\mathbf{J} + \eta_{B2}(R)\dot{\mathbf{J}}\right]\times\mathbf{e}\,, \tag{A.8a, b}$$

where $\eta_{\mathrm{A1}}(R) = \frac{\mu}{4\pi R}, \eta_{\mathrm{A2}}(R) = \frac{\mu\varepsilon}{4\pi R\sigma}, \eta_{\mathrm{B1}}(R) = \frac{\mu}{4\pi R^2}, \eta_{\mathrm{B2}}(R) = \frac{\mu\varepsilon}{4\pi R^2\sigma}$, $R = |\mathbf{r}-\bar{\mathbf{r}}|$,

$\mathbf{e} = \frac{1}{R}(\mathbf{r}-\bar{\mathbf{r}})$, $\bar{\mathbf{r}}$ is the location of the center of the volume.

APPENDIX B. ERROR ANALYSIS FOR REGULARIZATION

In (2.24), $[\varsigma]$ is assumed known, real-valued matrix and has a singular value decomposition (SVD) with strictly positive decreasing singular values s_i:

$$[\varsigma] = [\mathbf{F}]\left[\operatorname{diag}(s_i)\right][\mathbf{O}]^{\mathrm{T}} \tag{B.1}$$

Consequently, $[\varsigma]^{\mathrm{T}} = [\mathbf{O}]\left[\operatorname{diag}(s_i)\right][\mathbf{F}]^{\mathrm{T}}$ and $\mathbf{F}^{\mathrm{T}} = \mathbf{F}^{-1}$,

$$[\varsigma]^{\mathrm{T}}[\varsigma] = [\mathbf{O}]\left[\operatorname{diag}\left(s_i^2\right)\right][\mathbf{O}]^{\mathrm{T}} \tag{B.2}$$

Substituting (B.1), (B.2) and $[\mathbf{R}_\alpha]$ from (2.26b) into (2.27a, b) lead to

$$\hat{\mathbf{e}}_\alpha = \sum_{i=1}^{n}\left(w_\alpha\left(s_i^2\right)-1\right)\left(\mathbf{f}_i^{\mathrm{T}}\hat{\mathbf{J}}\right)\mathbf{o}_i \tag{B.3a}$$

$$\tilde{\mathbf{e}}_\alpha = \sum_{i=1}^{n} w_\alpha\left(s_i^2\right)s_i^{-1}\left(\mathbf{f}_i^{T}\boldsymbol{\eta}_1\right)\mathbf{o}_i \tag{B.3b}$$

where $w_\alpha(s^2) = \dfrac{s^2}{s^2+\alpha}$ is the Tikhonov filter function; and $\mathbf{f}_i$ and $\mathbf{o}_i$ are the column vectors of [**F**] and [**O**] respectively. As seen in (B.3a), $w_\alpha(s^2) \to 1$ and hence the solution truncation error $\hat{\mathbf{e}}_\alpha \to 0$ as $\alpha \to 0$.

To deal with the noise amplification error $\tilde{\mathbf{e}}_\alpha$, $\left(s-\alpha^{1/2}\right)^2 \geq 0$ or $w_\alpha(s^2)s^{-1} \leq \alpha^{-1/2}$ (since s^2 and α are positive). The regularization parameter α is chosen to have the form (B.4a) in terms of the error level δ defined in (B.4b):

$$\alpha = \delta^p \text{ where } \delta = \left\|\boldsymbol{\eta}_1\right\| > 0 \text{ and } 0 < p < 2 \tag{B.4a, b, c}$$

where $\|\bullet\|$ denotes the standard Euclidean norm. From (B.3b) along with (B.4b),

$\tilde{\mathbf{e}}_\alpha \le \alpha^{-1/2}\delta = \delta^{1-p/2}$ implying that the requirement $\tilde{\mathbf{e}}_\alpha \to 0$ as $\delta \to 0$ can be guaranteed with (α, p) given by (B4.a, c).

APPENDIX C. EQUIVALENT MAGNETIZATION CHARGE MODEL

The MFD around a permanent or soft magnetic object (with magnetization **M**) can be expressed as

$$\mathbf{B}_{\boldsymbol{m}} = \frac{\mu_0}{4\pi}\left(\iiint_V \frac{\rho_m \mathbf{R}}{R^3} dV + \oiint_S \frac{\rho_{ms} \mathbf{R}}{R^3} dS \right) \tag{C.1}$$

where **R** is the position vector from the source point to the point of interest; and ρ_m and ρ_{ms} (A/m^2) are its equivalent magnetization charge densities in volume V and at the surface (outward normal $\mathbf{e_n}$) of the magnet respectively:

$$\rho_m = -\nabla \bullet \mathbf{M} \text{ and } \rho_{ms} = \mathbf{M} \bullet \mathbf{e_n} \tag{C.2a,b}$$

Example: Rectangular magnetic object

For a uniformly magnetized rectangular object (sides a, b and c; and magnetization **M**) shown Figure B, ρ_m =0. Equation (C.1) reduces to a summation of six surface integrals:

$$\mathbf{B_m} = \frac{\mu_0}{4\pi} \sum_{i=1}^{6} \iint \frac{\rho_{ms_i} \mathbf{R}_i}{R_i^3} dS_i \tag{C.3}$$

In Figure C, **L** and **r** are the position vectors from the sensor to the object center O, and from O to an arbitrary point $P(c/2, y, z)$ on the shaded plane surface (with a unit normal $\mathbf{e_n}=[1\ 0\ 0]^T$) being considered respectively:

$$\mathbf{L} = \begin{bmatrix} L_x & L_y & L_z \end{bmatrix}; \ \mathbf{x} = \begin{bmatrix} \frac{c}{2} & y & z \end{bmatrix}; \ \mathbf{R} = \mathbf{L} + \mathbf{x} \tag{C.4a,b,c}$$

Thus, the surface integration on the shaded plane surface 1 is given by

$$\iint \frac{\rho_{ms_1}\mathbf{R}}{R_1^3} dS_1 = \int_{-b/2}^{b/2}\int_{-a/2}^{a/2} \frac{m_1\left[L_x+\frac{c}{2} \quad L_y+y \quad L_z+z\right]^{\mathrm{T}}}{\left[\left(L_x+c/2\right)^2+\left(L_y+y\right)^2+\left(L_z+z\right)^2\right]^{\frac{3}{2}}} dydz \tag{C.5}$$

The other five surface integrals can be calculated similarly for solving the magnetic flux density $\mathbf{B_m}$ in (C.1).

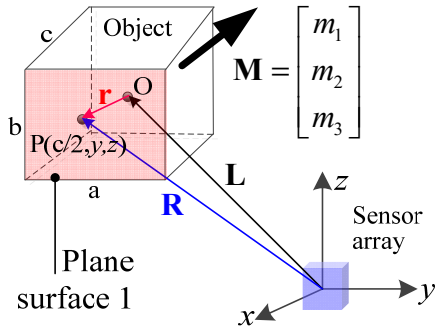

Figure C. Characteristic parameters for calculating MFD

APPENDIX D. MTS CALIBRATION

This appendix describes the procedure for calibrating the MTS (Figure 4.6b) which consists of four magnetometers. The MTS is calibrated on the experimental setup shown in Figure 4.6 (a) and (b). With the MTS rigidly attached to the 3-axis translational stage, the MTS is moved such that each of the four magnetometers measures the MFD (denoted as $\mathbf{B}i$ where i=1, 2, 3 and 4) generated by the PM at a common location. The measurements $\mathbf{B}j$ (where j=2, 3 and 4) are related to $\mathbf{B}_1$ by (D.1):

$$\mathbf{H}_{j1}\mathbf{B}_j = \mathbf{B}_1 \text{ where } \mathbf{H}_{j1} = \mathbf{A}_{j1}\mathbf{T}_{j1} \tag{D.1}$$

In (D.1), $\mathbf{A}_{j1}$ is a 3×3 diagonal matrix accounting for the relative scale factor between the j^{th} and 1st sensors; and $\mathbf{T}_{j1}$ is a 3×3 rotational matrix to describe $\mathbf{B}_j$ in $\mathbf{B}_1$ sensor coordinates. To calibrate $\mathbf{H}_{1i}$, the measuring steps are repeated at N locations resulting in four data sets (one for each sensor):

$$\mathbf{K}_i = \left[\mathbf{B}_{i1} \quad \cdots \quad \mathbf{B}_{ik} \quad \cdots \quad \mathbf{B}_{iN}\right]_{3\times N} \tag{D.2}$$

Expressed in $\mathbf{B}_1$ sensor coordinates,

$$\mathbf{H}_{j1}\mathbf{K}_j = \mathbf{K}_1 \tag{D.3}$$

$\mathbf{H}_{1i}$ is given by
$$\mathbf{H}_{1i} = \mathbf{K}_1\mathbf{K}_j^{\mathrm{T}}\left[\mathbf{K}_j\mathbf{K}_j^{\mathrm{T}}\right]^{-1} \tag{D.4}$$

The calibration results of the MTS shown in Figure 4.6(b) are given by

$$\mathbf{H}_{21} = \begin{bmatrix} 0.989 & 0.011 & 0.012 \\ -0.012 & 1.049 & -0.027 \\ -0.014 & 0.019 & 0.968 \end{bmatrix}; \mathbf{H}_{31} = \begin{bmatrix} 0.969 & 0.016 & 0.031 \\ -0.017 & 1.062 & 0.019 \\ -0.023 & 0.023 & 0.959 \end{bmatrix}; \text{ and}$$

$$\mathbf{H}_{41} = \begin{bmatrix} 1.051 & -0.017 & -0.024 \\ 0.015 & 0.949 & -0.027 \\ 0.024 & 0.098 & 1.081 \end{bmatrix} \qquad \text{(D.5a, b, c)}$$

REFERENCES

[1] I. Ulrich, and J. Borenstein, "The Guide Cane-Applying Mobile Robot Technologies to Assist the Visually Impaired," *IEEE Trans. on Systems, Man, and Cybernetics-Part A: Systems and Humans*, vol. 31, no. 2, pp. 131-135, Mar. 2001.

[2] C. Hu, Max Q.- H. Meng, and M. Mandal, "Efficient magnetic localization and orientation technique for capsule endoscopy," *Int. J. Inf. Acquisition,* vol. 01, pp. 628-633, Mar. 2011.

[3] S. D. Billings, "Discrimination and classification of buried unexploded ordnance using magnetometry," *IEEE Trans. on Geosci. & Remote Sens.,* vol. 42, no. 6, pp. 1241-1251, Jun. 2004.

[4] S. Foong, K.-M. Lee and K. Bai, "Harnessing embedded magnetic fields for angular sensing with nanodegree accuracy," *IEEE/ASME Trans. On Mechatronics*, vol. 17, no. 4, pp. 687-696, Aug. 2012.

[5] Y. Barrell, and H. W. L. Naus, "Detection and localization of magnetic objects," *IET Sci. Meas. Technol.* vol. 1, no. 5, pp. 245-254, Sep. 2007.

[6] N. Wahlstrom and F. Gustafsson, "Magnetometer modeling and validation for tracking metallic targets," *IEEE Trans. on Signal Process.*, vol. 62, pp. 545-556, Feb. 2014.

[7] S. Taghvaeeyan and R. Rajamani, "Use of vehicle magnetic signatures for position estimation," *Appl. Phys. Lett.*, vol. 99, pp. 134101-134101-3, Sep. 2011.

[8] J. Lenz and A. S. Edelstein, "Magnetic sensors and their applications," *IEEE Sensors J.*, vol. 6, no. 3, pp. 631-649, Jun. 2006.

[9] J. E. McFee, Y. DSA, and R. O Ellingson, "Locating and identifying compact ferrous objects," *IEEE Trans. on Geosc. & Remote Sens.*, vol. 28, no. 2, pp. 182-193, Mar. 1990.

[10] R. Wiegert, and J. Oeschger, "Portable magnetic gradiometer for real-time localization and classification of unexploded ordnances," *Oceans*, Panama City, FL, USA, Sep. 2006, pp. 1-6.

[11] K. M. Popek, A. W. Mahoney, and J. J. Abbott, *IEEE Inf. Conf. Robot. Autom. (ICRA)*, Karlsruhe, Germany, May 2013, pp. 5348-5353.

[12] A. Sheinker, L. Frumkis, B. Ginzburg, N. Salomonski and B. Z. Kaplan, "Magnetic anomaly detection using a three-axis magnetometer," *IEEE Trans. on Magn.*, vol.45, no.1, pp. 160-167, Jan. 2009.

[13] K.-M. Lee and M. Li, "Magnetic field localization method for guiding visually impaired applications," *IEEE/ASME Adv. Intell. Mechatronics (AIM)*, Wollongong, NSW, Jul. 2013, pp. 542-547.

[14] V. Schlageter, P.-A. Besse, R.S. Popovic and P. Kucera, "Tracking system with five degrees of freedom using a 2D-array of hall sensors and a permanent magnet," *Sens. Actuators A: Phys.,* vol. 92, pp. 37-42, Aug. 2001.

[15] H. M. Shen, L. Hu, X. Fu, and K.-M. Lee, "A novel method for locating PM marker based on magnetic field reconstruction," in *Proc.* 7th *IEEE Conf. Ind. Electron. Appl. (ICIEA)*, Singapore, Jul. 2012, pp.1683-1687.

[16] R. Liu and Y.-X. Wang, "Auditory Feedback and Sensory Substitution during Tele-operated Navigation," *IEEE/ASME Trans. on Mechatronics,* vol. 17, no. 4, pp. 680-686, Aug. 2012.

[17] B. Li, Y. Wang, H. K. Lee, A. Dempster, and C. Rizos, "Method for Yielding a Database of Location Fingerprints in WLAN," *IEE Proc.- Commun.*, vol. 152, pp. 580-586, 2005.

[18] V. Moghtadaiee, A.G. Dempster, and Samsung Lim, "Indoor Localization Using FM Radio Signals: A Fingerprinting Approach," in *Proc. Int. Conf. on Indoor Position. Indoor Navig.*, Sep. 21-23, 2011, pp. 1-7.

[19] C. Ye, S. Hong, and A. Tamjidi, "6-DOF Pose Estimation of a Robotic Navigation Aid by Tracking Visual and Geometric Features," *IEEE Trans. on Autom. Sci. Eng.*, vol. 12, no. 4, pp. 1169-1180, Oct. 2015.

[20] S. Gezici, Z. Tian, G. Giannakis, H. Kobayashi, A. Molisch, H. Poor, and Z. Sahinoglu, "Localization via Ultra-wideband Radios: a Look at Positioning Aspects for Future Sensor Networks," *Signal Process. Mag.,* vol. 22, pp. 70-84, Jul. 2005.

[21] N. B. Priyantha, A. Chakraborty, and H. Balakrishnan," The Cricket Location-support System," in Proc. *6th Annu. Int. Conf. Mobile Comput. Netw.*, Boston, Massachusetts, USA, Aug. 2000, pp. 32-43.

[22] R. Want, A. Hopper, V. Falcao, and J. Gibbons," The Active Badge Location System," *ACM Trans. on Inf. Syst.* vol.10, pp. 91-102, 1992.

[23] D. Hauschildt, and N. Kirchhof, “Improving Indoor Position Estimation by Combining Active TDOA Ultrasound and Passive Thermal Infrared Localization,” in *Proc. 8th Workshop on Position. Navig. Commun.*, Apr. 7-8, 2011, pp. 94-99.

[24] B. Zhou, Q. Li, Q. Mao, W. Tu, and X. Zhang, "Activity Sequence-Based Indoor Pedestrian Localization using Smartphones," *IEEE Trans. on Human-Mach. Syst.*, vol. 45, no. 5, pp. 562-574, Oct. 2015.

[25] S. Kaluwahandi, and Y. Tadokoro, “Portable Traveling Support System Using Image Processing for the Visually Impaired,” in *Proc. Int. Conf. Imag. Process.,* 2001, vol.1, pp. 337-340.

[26] D. Dakopoulos, and N. N.G. Bourbakis, "Wearable Obstacle Avoidance Electronic Travel Aids for Blind: A Survey," *IEEE Trans. on Syst., Man, Cybern. C: Appl. Rev.*, vol. 40, no. 1, pp. 25-35, Jan. 2010.

[27] B. Ando, S. Baglio, V. Marletta, and A. Valastro, "A Haptic Solution to Assist Visually Impaired in Mobility Tasks," *IEEE Trans. on Human-Mach. Syst.*, vol. 45, no. 5, pp. 635-640, Oct. 2015.

[28] B. Ando, "A Smart Multisensor Approach to Assist Blind People in Specific Urban Navigation Tasks," *IEEE Trans. on Neural Syst. Rehab. Eng.*, vol. 16, no. 6, pp. 592-594, Dec. 2008.

[29] N. Bourbakis, S. K. Makrogiannis, and D. Dakopoulos, "A System-Prototype Representing 3D Space via Alternative-Sensing for Visually Impaired Navigation," *IEEE Sensors J.*, vol. 13, no. 7, pp. 2535-2547, Jul. 2013.

[30] V. Garaj, Z. Hunaiti, and W. Balachandran, "Using Remote Vision: The Effects of Video Image Frame Rate on Visual Object Recognition Performance," *IEEE Trans. on Syst., Man, and Cybern. A: Syst. Humans*, vol. 40, no. 4, pp. 698-707, Jul. 2010.

[31] Z. Hunaiti, V. Garaj, and W. Balachandran, "An Assessment of a Mobile Communication Link for a System to Navigate Visually Impaired People," *IEEE Trans. on Instrum. Meas.*, vol. 58, no. 9, pp. 3263-3268, Sep. 2009.

[32] J. Xiao, S. L. Joseph, X. Zhang, B. Li, X. Li, and J. Zhang, "An Assistive Framework for the Visually Impaired," *IEEE Trans. on Human-Mach. Syst.*, vol. 45, no. 5, pp. 635-640, Oct. 2015.

[33] K.-M. Lee, and C.-Y Lin, “Design Concept of a Novel EM-Array Magnetic Scanning System for Continuous Motion Control of Maximum MFD,” in *Proc. IEEE/ASME*

Adv. Intell. Mechatronics (AIM) 2014. Besacon, France, Jul. 8-11, 2014, pp. 1581-1586.

[34] M. Nakajima, and S. Harurama "Indoor Navigation System for Visually Impaired People Using Visible Light Communication and Compensated Geomagnetic Sensing," in *Proc. 1st IEEE Int. Conf. on Commun. China*, Aug. 15-17 2012, pp. 524-529.

[35] T. Gallagher, E. Wise, B. Li, A. G. Dempster, C. Rizos, and E. Ramsey-Stewart, "Indoor Positioning System Based on Sensor Fusion for The Blind and Visually Impaired," in *Proc. Int. Conf. on Indoor Position. Indoor Navig.*, Nov.13-15 2012, pp.1-9.

[36] B. Gozick, K. P. Subbu, R. Dantu, and T. Maeshiro, "Magnetic Maps for Indoor Navigation," *IEEE Trans. on Instrum. & Meas.*, vol. 60, no. 12, pp. 3883-3891, Dec. 2011.

[37] M. Wrzuszczak, J. Wrzuszczak, "Eddy current flaw detection with neural network applications," *Measurement*, vol. 28, no. 2, pp. 132-136, 2005.

[38] B. Lebrun, Y. Jayet, J. C. Baboux, "Pulsed eddy current signal analysis: application to the experimental detection and characterization of deep flaws in highly conductive materials," *NDT & E International*, vol. 30, no. 3, pp. 163-170, 1997.

[39] J. C. Moulder, E. Uzal, and J. H. Rose1, "Thickness and conductivity of metallic layers from eddy current measurements," *Review of Sci. Instrum.*, vol. 63, no. 6, pp. 3455-3465, 1992.

[40] F. Sakran, M. Golosovsky, H. Goldberger, and D. Davidov, "High-frequency eddy-current technique for thickness measurement of micron-thick conducting layers," *Applied Physics Letters*, vol. 78, no. 11, pp. 1634-1626, 2001.

[41] R. Grimberg, Lalita Udpa, Adriana Savin, Rozina Steigmann, Valerian Palihovici, and Satish S. Udpa, "2D Eddy current sensor array," *NDT & E International*, vol. 39, no. 4, pp. 264-271, 2006.

[42] R. Grimberg, A. Savin, E. Radu, O., Mihalache, "Nondestructive Evaluation of the Severity of Discontinuities in Flat Conductive Materials by an Eddy-Current Transducer with Orthogonal Coils," *IEEE Trans. on Magn.*, vol. 36, no. 1, pp. 299-307, 2000.

[43] D. G. Park, C. S. Angani, G. D. Kim, C. G. Kim, and Y. M. Cheong, "Evaluation of Pulsed Eddy Current Response and Detection of the Thickness Variation in the Stainless Steel," *IEEE Trans. on Magn.*, vol. 45, no. 10, pp. 3893-3896, 2009.

[44] J. Kral, R. Smid, H. M. G. Ramos, and A. L. Ribeiro, "The Lift-Off Effect in Eddy Current on Thickness Modeling and Measurement," *IEEE Trans. on Instrum. & Meas.*, vol. 62, no. 7, pp. 2043-2049, 2013.

[45] T. Dogaru, and S. T. Smith, "Giant Magnetoresistance-Based Eddy-Current Sensor," *IEEE Trans. on Magn.*, vol. 37, no. 5, pp. 3831-3838, 2001.

[46] J. R. Claycomb, N. Tralshawala, and J. H. Miller, "Theoretical Investigation of Eddy-Current Induction for Nondestructive Evaluation by Super conducting Quantum Interference Devices," *IEEE Trans. on Magn.*, vol. 36, no. 1, pp. 292-298, 2000.

[47] T. Kiwa, Hideaki Tahara, Etsuro Miyake, Hironobu Yamada, and Keiji Tsukada, "Non-contact Thickness Gauge for Conductive Materials Using HTS SQUID System," *IEEE Trans. on Applied Superconductivity*, vol. 19, no. 3, pp. 801-803, 2009.

[48] G. Yang, A. Tamburrino, L. Udpa, S. S. Udpa, Z. Zeng, Y. Deng, and P. Que, "Pulsed Eddy-Current Based Giant Magnetoresistive System for the Inspection of Aircraft Structures," *IEEE Trans. on Magn.*, vol. 46, no. 3, pp 910-917, Mar. , 2010.

[49] W. Yin, S. J. Dickinson, and A. J. Peyton, "A multi-frequency impedance analyzing instrument for eddy current testing," *Meas. Sci. & Tech.*, vol. 17, no. 2, pp. 393-402, 2006.

[50] Y. L. Diraison, P.-U. Joubert, D. Placko, "Characterization of subsurface defects in aeronautical riveted lap-joints using multi-frequency eddy current imaging," *NDT & E International*, vol. 42, no. 2, pp. 133-140, 2009.

[51] S. Hosseini, and A. A. Lakis, "Application of time-frequency analysis for automatic hidden corrosion detection in a multilayer aluminum structure using pulsed eddy current," *NDT & E International*, 47, pp. 70-79, 2012.

[52] K. M. Lee, M. Li and K. Bai, " An Investigation of Eddy-Current Effects On Parameter Monitoring for Duplex Lathe Machining Of thin-Wall Components," *ASME Dynamic Systems and Control Conf.,* Oct. 22-24, 2014, San Antonio, Texas, USA

[53] K. M. Lee, and H. Son, "Distributed Multipole Model for Design of Permanent-Magnet based Actuators," *IEEE Trans. on Magn.* , vol. 43, no. 10, pp. 3904-3913, 2007.

[54] J. Lim and K. M. Lee, "Distributed Multilevel Current Models for Design Analysis of Electromagnetic Actuators," *IEEE/ASME Trans. on Mech.* , vol. 20, no. 5, pp. 2413-2424, Oct. 2015.

[55] Curtis R. Vogel, *Computational Method for Inverse Problems*, SIAM, 2002.

[56] P.C. Hansen, "*Numerical Tools for Analysis and Solution of Fredholm Integral Equations of the First Kind*," *Inverse Problems*, vol. 8, no. 6, pp. 956-972, 1992.

[57] M. Hanke, P.C. Hansen, "*Regularization Methods for Large-scale Problems*," *Surveys on Mathematics for Industry*, vol. 3, pp. 253-315, 1993.

[58] D. A. Clark, "New methods for interpretation of magnetic vector and gradient tensor data I: Eigenvector analysis and the normalized source strength," *Exploration Geophys.*, vol. 43, no. 4, pp. 267–282, 2012.

[59] K.-M. Lee, and M. Li. "Magnetic tensor sensor for gradient-based localization of ferrous object in geomagnetic field." *IEEE Trans. on Magn. ,* vol.52. pp. 1-10, 2016.

[60] Bosch Sensortec, "BMC050 Electronic Compass", BMC050 datasheet, Oct. 2011.

[61] S. Bellavia, M. Macconi and B. Morini, "A two-dimensional trust-region method for large scale bound-constrained nonlinear systems," in *Applied & Industrial Mathematics in Italy II*, Singapore: Word Scientific, pp. 137-148, 2007.

[62] Image Processing Toolbox, MATLAB 7.0.4 (R14SP2) 1994-2015 The MathWorks, Inc.

[63] K.-M. Lee, Q. Li, and W. Daley, "Effects of Classification Methods on Color-Based Feature Detection with Food Processing Applications," *IEEE Trans. on Auto. Sci. Eng.* vol. 4, no. 1, pp: 40-51, Jan. 2007.

[64] J. Y. Bouguet, "Pyramidal Implementation of the Lucas-Kanade Feature Tracker Description of the Algorithm", OpenCV Documents, Microprocessor Res. Labs, Intel Corp., 1999.

[65] C. V. Dodd and W. E. Deeds, "Analytical Solutions to Eddy-Current Probe-Coil Problems," *J. Appl. Phys*., vol. 39, pp. 2829-2838, 1968.

[66] J. W. Luquire, W. E. Deeds, and C. V. Dodd, "Alternating Current Distribution Between Planar Conductor," *J. A. Phys*., vol. 41, pp. 3983-3991, 1970.

[67] B. A. Abu-Nabah, F. Yu, W. T. Hassan, M. P. Blodgett and P. B. Nagy, "Eddy current residual stress profiling in surface-treated engine alloys," *NDT & E International*, vol. 24, nos. 1-2, pp. 209-232, 2009.

[68] M. Morozov, G. Y. Tian, P. J. Withers, "Noncontact Evaluation of the Dependency of Electrical Conductivity on Stress for Various AI Alloys as a Function of Plastic Deformation and Annealing,", *J. Appl. Phys.*, vol. 108, 2010.